CrossMark

The Feasibility of Detecting Biosignatures in the TRAPPIST-1 Planetary System with JWST

Victoria S. Meadows[1,2] , Andrew P. Lincowski[1,2] , and Jacob Lustig-Yaeger[2,3]

[1] Department of Astronomy and Astrobiology Program, University of Washington, Box 351580, Seattle, WA 98195, USA; meadows@uw.edu
[2] NASA Nexus for Exoplanet System Science, Virtual Planetary Laboratory Team, Box 351580, University of Washington, Seattle, WA 98195, USA
[3] Johns Hopkins University Applied Physics Laboratory, Laurel, MD 20723, USA

Abstract

The James Webb Space Telescope (JWST) provides the first opportunity to detect gases in the atmospheres of M-dwarf terrestrial planets and search for signs of life. Here we determine the detectability of a comprehensive suite of biosignature gases that may have been episodically prevalent across Earth's history. We used coupled 1D climate–photochemical models to generate synthetic inhabited terrestrial planetary environments for TRAPPIST-1 d and e. These encompass cloudy and/or hazy Archean-Earth-like environments with either a dominant sulfur- or methane-producing biosphere, as well as clear and cloudy modern-Earth-like environments with photosynthetic oxygen-producing biospheres. We generate transmission spectra and assess the likely detectability of different biosignatures with JWST. Our simulations suggest that biogenically generated O_2 and its photosynthetic by-product O_3 will likely be extremely difficult to detect. We explored the detectability of methyl chloride (CH_3Cl) as an alternative indicator for a photosynthetic biosphere but find that it will likely require significantly higher global surface fluxes than Earth's. We find that the CH_4 and CO_2 disequilibrium pair is potentially detectable in ∼10 transits for both the methanogen-dominated Archean-like environment and the modern photosynthetic-dominated biosphere—even in cloudy atmospheres. Organic haze and methyl mercaptan are other potential biosignatures for the Archean. Given the likely difficulties in observing an oxygenic-photosynthetic biosphere with JWST, we conclude that the methanogenic biosphere revealed by the combination of outgassed CO_2 in the presence of methanogenically generated CH_4 may be the most persistent detectable biosignature for an Earth-like planet.

Unified Astronomy Thesaurus concepts: Astrobiology (74); Biosignatures (2018); Transmission spectroscopy (2133); Exoplanet atmospheres (487)

1. Introduction

With its small (M8V) host star and seven transiting Earth-sized planets, the TRAPPIST-1 system currently provides the best opportunity to attempt a near-term search for biosignatures in a terrestrial exoplanetary atmosphere. The small size of the stellar host enhances the planet–star contrast ratio of atmospheric absorption features and could enable potentially detectable molecular transit features of 100–200 ppm, even in a high molecular weight (e.g., N_2- or CO_2-dominated) atmosphere (e.g., Morley et al. 2017; Lincowski et al. 2018; Lustig-Yaeger et al. 2019). Up to four of the seven known TRAPPIST-1 planets (d, e, f, and g) are at a distance from their star where—depending on the presence and composition of their atmospheres—they may be able to support liquid water, and therefore biospheres, on their surfaces (Gillon et al. 2017; Ducrot et al. 2020; Agol et al. 2021). Of these potentially habitable targets, TRAPPIST-1 d and e are the most promising observationally, given their proximity to the star, which results in shorter orbital periods and more opportunities to observe the planets in transit during the mission lifetime. Additionally, TRAPPIST-1 d's smaller mass favors a higher atmospheric scale height and an enhanced ability to detect molecular features in transmission (Lincowski et al. 2018; Lustig-Yaeger et al. 2019; Agol et al. 2021).

Early attempts to determine the properties of the TRAPPIST-1 planets have provided multiple observational constraints on the possible nature of the atmospheres, which, if present, are likely to be high molecular weight terrestrial-type atmospheres. Hubble Space Telescope (HST) and Spitzer observations did not detect molecular features but ruled out clear-sky low molecular weight, H_2-dominated atmospheres on all but TRAPPIST-1 g (de Wit et al. 2018; Delrez et al. 2018). Early modeling and laboratory results also suggested that the current observational data are inconsistent with an H_2-dominated atmosphere with high hazes (Moran et al. 2018). Theoretical calculations also make the case that only small amounts of H_2 would have been accreted during formation by the migrating chain of TRAPPIST-1 planets and that there is a high probability that these tenuous primordial atmospheres were subsequently lost (Hori & Ogihara 2020). A comprehensive review of existing constraints from transit observations and bulk density measurements, combined with orbital, evolutionary, and climate modeling, makes a solid case against the presence of clear or cloudy H_2-dominated atmospheres (Turbet et al. 2020). Exquisitely precise new measurements of planetary mass via transit timing variations (Agol et al. 2021) also show that water mass fractions comparable to or higher than Earth's are not ruled out for TRAPPIST-1 e, with the possibility of an attendant surface ocean and a terrestrial-type atmosphere. Consequently, observations and laboratory measurements, along with a broad suite of modeling results, suggest that the TRAPPIST-1 habitable-zone (HZ) planets are unlikely to have H_2-dominated atmospheres. They may either have no atmospheres at all—which may be the result of stellar-activity-driven atmospheric loss (Bolmont et al. 2017)—or have higher

molecular weight secondary atmospheres. The latter type of atmosphere may be generated from early ocean-loss processes, or via sufficient levels of interior outgassing that balance rates of atmospheric loss (Meadows et al. 2018; Barth et al. 2021; Krissansen-Totton & Fortney 2022).

While HST and Spitzer were unable to detect the TRAPPIST-1 planetary atmospheres, the James Webb Space Telescope (JWST) has the sensitivity to detect molecular features in even high molecular weight atmospheres (e.g., Greene et al. 2016; Morley et al. 2017; Batalha et al. 2018; Lincowski et al. 2018; Lustig-Yaeger et al. 2019), enabling the first search for atmospheric biosignature gases on Earth-sized, and likely terrestrial (Rogers 2015; Weiss et al. 2016; Fulton et al. 2017), exoplanets. Given this new capability, it is therefore important to comprehensively assess whether a range of known potential biosignatures (Des Marais et al. 2002; Segura et al. 2005; Domagal-Goldman et al. 2011; Schwieterman et al. 2018) for terrestrial-type atmospheres may be detected with JWST, including key factors affecting detectability, such as photochemical lifetimes and the presence of clouds and hazes. Initial research on this important problem suggests that biological levels of CH_4 (Lin et al. 2021), or the CH_4/CO_2 disequilibrium pair for an early Earth environment (Krissansen-Totton et al. 2018b), may be detectable in as few as 5–10 transits for TRAPPIST-1 e (Krissansen-Totton et al. 2018a; Lin et al. 2021; Mikal-Evans 2022). Existing estimates of the detectability of modern Earth's O_2 and O_3 biosignatures on a TRAPPIST-1 HZ planet are largely in agreement that detection will be extremely challenging, although predicted minimum observations for 3σ detection vary widely, with a typical range of 85–200 transits (Lustig-Yaeger et al. 2019; Wunderlich et al. 2019, 2020; Pidhorodetska et al. 2020; Gialluca et al. 2021; Lin et al. 2021).

Using transmission spectroscopy for biosignature detection is not without challenges, as this technique may not be able to probe the near-surface atmosphere where biosignature signals may be strongest. Although refraction is less effective at truncating transmission paths in M-dwarf planetary atmospheres (Muñoz et al. 2012; Bétrémieux & Kaltenegger 2014; Misra et al. 2014), intrinsic atmospheric opacity, or the presence of clouds or hazes, must also be considered. All of these phenomena can create a baseline overlapping spectral continuum that blocks sight lines close to the planetary surface (Lustig-Yaeger et al. 2019). A biosignature gas is therefore more likely to be detected via JWST transmission spectroscopy if it is both abundant and resistant to photochemical destruction. These attributes will make it more likely to be present throughout the planet's atmospheric column, thereby making it more detectable even in the presence of clouds, hazes, or molecular continuum absorption (Meadows 2017). While any volatile, biologically produced gas could serve as a biosignature (Seager et al. 2016), photochemical processes will decrease the survivability of complex biogenic molecules at higher altitudes (Domagal-Goldman et al. 2011), while hazes and other UV absorbers may protect them (Sagan & Chyba 1997; Domagal-Goldman et al. 2011; Arney et al. 2017). These processes may combine to affect the overall detectability of complex biosignature gases, although this has not been explicitly modeled.

When considering relevant biosignatures for a JWST search, Earth's 4.6 Gyr history provides a suite of example biosignatures that are paired with habitable environments known to support the relevant biosignature-producing metabolism—and that span atmospheric compositions from reducing to oxidizing. Potential biosignature targets that produce features in the near- and mid-infrared in Earth's modern-day atmosphere include anomalously abundant, photosynthetically generated O_2 (Meadows 2017); the classic O_2/CH_4 disequilibrium (Hitchcock 1967; Lovelock 1975; Krissansen-Totton et al. 2016), which is driven by both oxygenic photosynthesis and a methanogenic biosphere; and methyl chloride (CH_3Cl), which is produced in the nonindustrial world primarily by photosynthetic, and especially tropical, vegetation (Yokouchi et al. 2002; Saito & Yokouchi 2008). For the early Earth, the CH_4/CO_2 disequilibrium pair may indicate a sufficiently high flux of CH_4, indicating that methanogenesis, rather than geology, is the most likely source (Krissansen-Totton et al. 2018b; Thompson et al. 2022). A more sulfur-dominated biosphere could emit a variety of gases, including dimethyl sulfide (DMS), dimethyl disulfide (DMDS), and their photochemical by-product, ethane (Pilcher 2003; Domagal-Goldman et al. 2011). In these cases, the excess methyl groups from the biogenic gases may also help to generate an organic haze, which, since it is biologically mediated, could also serve as a potential biosignature if chemical context and the UV spectrum of the parent star are known (Arney et al. 2018).

Earth's modern oxygenic-photosynthetic biosphere is estimated to be at least three orders of magnitude more productive than Earth's early pre-photosynthetic biosphere (Des Marais 2000; Canfield et al. 2006; Hoehler et al. 2020), giving photosynthetic by-products a potential advantage in dominating a planet's observable environment. However, it may take a significant amount of time to achieve that dominance, with evidence suggesting that Earth's O_2 was below 0.1% of the modern value as recently at 0.8 Gyr ago (Planavsky et al. 2014b). While abundant O_2 generally has many observational advantages as a biosignature (Meadows 2017), JWST's spectral resolution and sensitivity are not well matched to the planetary spectral regions where O_2 is most prominent, and so other indicators of oxygenic photosynthesis may need to be considered. For the smaller M-dwarf hosts needed to increase the detectability of planetary atmospheric molecular features in transmission, their backlighting stellar spectra drop off sharply in both the visible to near-infrared and longer mid-infrared regions, where O_2 and its photochemical by-product, O_3, absorb most strongly. This leads to a loss of sensitivity to the 0.76 μm O_2 and the 9.6 μm O_3 features in transmission spectra (Lustig-Yaeger et al. 2019). The 1.27 μm O_2 feature might therefore be the most promising, but its relatively narrow width and moderate absorption strength in Earth-like atmospheres make detection challenging at JWST's spectral resolution and precision (Fauchez et al. 2019; Lustig-Yaeger et al. 2019; Pidhorodetska et al. 2020). Fauchez et al. (2019) proposed that the broad O_2–O_2 collisionally induced absorption at 6 μm might provide an alternative, potentially stronger feature that could reveal the presence of abundant biologically generated O_2 in a planetary atmosphere. However, this feature overlaps with a strong water band at 6.3 μm, and so its detectability becomes potentially challenging in habitable, water-rich atmospheres.

Given JWST's relatively poor sensitivity to biogenic O_2, an alternative tracer of oxygenic photosynthesis might be found in methyl chloride (CH_3Cl). CH_3Cl has strong features in the near- to mid-infrared (Nikitin et al. 2016), and it was first

identified as a potential biosignature for emission spectroscopy observations of M-dwarf planets by Segura et al. (2005). Their photochemical calculations suggested that, in a manner similar to the buildup of CH_4 for planets orbiting M dwarfs, the abundance of CH_3Cl could be enhanced by up to three orders of magnitude over Earth values for the same surface flux, thereby enhancing its detectability. While Earth's sources of CH_3Cl have not been fully identified, on Earth the largest known nonanthropogenic source of CH_3Cl is tropical coastal land (Yokouchi et al. 2002; Seinfeld & Pandis 2006; Saito & Yokouchi 2008), in addition to planktonic sources in the oceans and bacterial sources in salt marshes (Seinfeld & Pandis 2006). Tropical plants and ferns have subsequently been identified as a major source for atmospheric CH_3Cl, with laboratory experiments showing that these plants produced CH_3Cl at a rate ∼6 times the average global flux (Yokouchi et al. 2002). Atmospheric CH_3Cl levels therefore should have been higher at times in the Carboniferous period (440 Mya), when global vegetation coverage of tropical plants and ferns was likely increased (Yokouchi et al. 2002). However, if CH_3Cl is produced primarily by vegetation, it may also have a late rise to detectable abundances and, like biogenic O_2, a relatively short opportunity to be seen in a planetary atmosphere. Recent comprehensive work has also explored the production of CH_3Cl and CH_3Br by microorganisms in saline wetlands as a potential biosignature for JWST that may have persisted over a larger span of Earth's history (Leung et al. 2022).

Although not as productive as an oxygenic-photosynthetic biosphere, the methanogenic biosphere may gain a detectability advantage by persisting over a larger fraction of a planet's lifetime. On Earth, methanogenesis is an ancient metabolism, possibly evolving as early as 3.5 Gyr ago (Wolfe & Fournier 2018). CH_4 in the Archean was also likely much higher than today, with lower limits on CH_4 abundance ranging from >20 to >5000 ppm (Catling & Zahnle 2020) based on required sulfur chemistry to explain observed mass-independent sulfur signals (Zahnle et al. 2006) and xenon isotope fractionation (Zahnle et al. 2019) in the rock record. Coupled models suggest that to maintain thousands of parts per million of CH_4 in the anoxic Archean atmosphere, the productivity of the Archean methanogenic biosphere was similar to or even higher than that of modern Earth's (Kharecha et al. 2005; Ozaki et al. 2018; Catling & Zahnle 2020). Earlier in Earth's history, before the rise of O_2, the atmosphere was likely more reducing, and many metabolisms would have driven the environment toward chemical equilibrium, making them more challenging to identify (Des Marais 2000; Canfield et al. 2006). Nonetheless, in a more reducing atmosphere, by-products from methanogenesis (CH_4) can accumulate (Catling & Zahnle 2020). These by-products also accumulate for planets orbiting earlier-type M-dwarf stars, even in an oxygen-rich atmosphere, where the stellar UV favors a longer planetary atmospheric lifetime for CH_4 (Segura et al. 2005; Rugheimer et al. 2015). As a possible threshold for interpreting abundant CH_4 alone as a biosignature, Guzmán-Marmolejo et al. (2013) suggest that an abundance above a threshold of 10 ppm in a terrestrial planetary atmosphere may be indicative of life, as it is difficult to generate and maintain this much atmospheric CH_4 with abiotic water/rock reactions. However, the lower densities of the TRAPPIST-1 planets compared to Earth (Grimm et al. 2018) may suggest a higher primordial volatile abundance

(Agol et al. 2021), which could include significant reservoirs of CH_4 ice, potentially providing a false positive for the abundant CH_4 biosignature.

Instead of using abundant CH_4 as a sole indicator of a large, likely biological flux of CH_4, Krissansen-Totton et al. (2018b) suggest that a more easily interpretable biosignature may be the simultaneous presence of CH_4 and CO_2 in an early Earth-like environment. In this case, a high flux of CH_4 is required to maintain a detectable abundance in the atmosphere against atmospheric oxidants such as CO_2. While abiotic outgassing of large fluxes of CH_4 from a more reduced interior is a potential false positive, such a scenario would also tend to produce high levels of outgassed CO, which could serve as a false-positive discriminant (Krissansen-Totton et al. 2018b). In a follow-up paper, Krissansen-Totton et al. (2018a) used simulated observations of atmospheres with prescribed, nonphotochemically consistent CO_2/CH_4 abundances and performed spectroscopic retrievals to show that both CO_2 and CH_4 can produce strong, potentially detectable and quantifiable features in JWST transmission spectra of the TRAPPIST-1 planets, although the detectability of the CO discriminant was not explored. However, the interpretation of this combined biosignature is not entirely straightforward, as there may be planetary conditions that allow the generation of relatively large amounts of CO in an inhabited and more modern-Earth-like atmosphere, especially for planets orbiting M dwarfs (Schwieterman et al. 2019; Zhan et al. 2022). Consequently, caution and additional information will be needed to interpret the simultaneous observation of CO_2, CH_4, and CO, especially for JWST data, where photosynthetic O_2 and O_3 may be much harder to detect (Schwieterman et al. 2019).

Photochemistry has been shown to be critically important for both the destruction and production of biosignatures (Segura et al. 2005; Domagal-Goldman et al. 2011; Meadows et al. 2018) and so should be considered when assessing which potential biosignature molecules to target and their potential detectability. For example, for more reducing terrestrial environments in which sulfur-producing metabolisms dominate, it has been suggested that complex but less ambiguous biogenic molecules such as DMS (or DMDS) will be rapidly photolytically destroyed in the upper atmosphere (Domagal-Goldman et al. 2011) and so are less likely to be detected in transmission. However, their photolytic by-products, including the CH_3 radical, can combine to form ethane (C_2H_6)—which is more robust to photolysis and has strong features in the mid-infrared (Domagal-Goldman et al. 2011). Additionally, in the right environmental conditions a high flux of these photolytic by-products can produce a biologically mediated organic haze, a potential biosignature that has strong spectral features in the UV and the blue (Arney et al. 2018). However, a high CH_4/CO_2 ratio, whether biogenic or not, can also enhance photochemical organic haze production (especially around M dwarfs; Arney et al. 2016, 2017), potentially obscuring sensitivity to other biosignatures, making the haze biosignature challenging to interpret.

Here we provide a comprehensive exploration of the potential detectability of a suite of biosignatures in JWST observations for both oxidizing and reducing terrestrial atmospheres and for several different metabolisms. We use coupled photochemical–climate models for inhabited Earth-like TRAPPIST-1 d and TRAPPIST-1 e environments to generate atmospheric compositions that are self-consistent with the

spectrum of the host star and to simulate transmission spectra of these environments. We model several archetypal environments/biospheres of Earth throughout its history, including reducing Archean-Earth-like environments with either methanogenesis or enhanced biogenic sulfur-containing fluxes, and modern-Earth-like oxygenic biospheres with and without enhanced CH_3Cl fluxes from vegetation. We explore the detectability and interpretation of biosignatures in clear, cloudy, and—where appropriate—hazy conditions, using JWST noise and instrument models. Section 2 discusses our modeling efforts; Section 2.4.1 specifically discusses the assumptions for our different model environments. Section 3 describes the results. In Section 4 we discuss the ramifications of these simulations for the possibility of life detection on exoplanets with JWST, and in Section 5 we provide our conclusions.

2. Methods

Here we use coupled 1D planetary climate (VPL Climate) and photochemistry (*Atmos*; Virtual Planetary Laboratory 2021) models to simulate our plausible inhabited environments for TRAPPIST-1 d and e. The photochemistry and climate simulations are driven self-consistently by the spectrum of the TRAPPIST-1 star and incorporate up-to-date planetary and orbital parameters. These 1D models also explicitly calculate haze formation for reducing atmospheres and identify atmospheric layers of water vapor condensation, which is used to determine reasonable altitudes for prescription of Earth-like ice and liquid-water clouds. We use a radiative transfer model to simulate the resulting transmission spectra for these inhabited environments, with clouds and hazes where appropriate. Finally, we use the PandExo model to estimate noise levels and required exposure times to detect biosignature features with JWST instruments. These models and the stellar and surface albedo inputs are described in more detail in the sections below.

2.1. The VPL Climate Model

To generate the temperature–pressure profiles for the habitable modeled atmospheres considered here, we use VPL Climate, a general-purpose, 1D radiative-convective-equilibrium, terrestrial planet climate model (Lincowski et al. 2018; Meadows et al. 2018; Robinson & Crisp 2018). This model uses the Spectral Mapping Atmospheric Radiative Transfer model (SMART; see Section 2.5 below) for rigorous, spectrum-resolving (line-by-line) radiative transfer, coupled to a mixing-length convection parameterization, which includes condensation and a radiatively active layer-by-layer cloud parameterization. The VPL Climate model components and inputs are described in more detail in Lincowski et al. (2018).

To better model atmospheric water vapor for habitable ocean-bearing planets, the atmospheric convective processes were updated from Lincowski et al. (2018) and are described in detail in Appendix A. We validated this updated model against Earth's measured vertical profiles for temperature, water vapor, and eddy diffusion coefficient and obtained agreement within the measured ranges of these parameters for Earth. The detailed description of this validation can be found in Appendix B. The convection parameters used for the modern Earth validation test, and subsequently used for all environments in this work, are given in Table 1. The mixing-length proportionality

Table 1
Adjustable Convection Model Parameters

Parameter	Earth	Description
f_z	0.085	Mixing-length proportionality constant
U (m s^{-1})	7	Surface wind speed
z_0 (m)	0.004	Surface roughness length
du/dz (s^{-1})	0.02	Constant wind shear
ρ_0 (kg m^{-3})	1	Baseline density for eddy diffusion
P_0 (Pa)	1	Pressure for breaking of gravity waves in eddy diffusion
$K_{h,1}$ (m^2 s^{-1})	0.5	Constant minimal eddy diffusion for heat
$K_{m,0}$ (m^2 s^{-1})	0.2	Eddy scaling coefficient for mass, gravity waves
$K_{m,1}$ (m^2 s^{-1})	0.5	Constant minimal eddy diffusion for mass

constant and the constant wind shear value are the most sensitive convective parameters. These parameters can affect the tropospheric lapse rate and thereby the surface and cold trap temperatures. The minimum eddy diffusivity affects transport through the cold trap.

2.2. Atmospheric Chemistry Model

To self-consistently model the effects of TRAPPIST-1's UV radiation on our modeled atmospheres, VPL Climate is coupled to an updated photochemical module of the *Atmos*[4] atmospheric climate–chemistry model for terrestrial planets. The *Atmos* code is based on Kasting et al. (1979), and the version we use here has been significantly updated as described in Zahnle (2006), Arney et al. (2016), and Lincowski et al. (2018). *Atmos* can simulate a wide range of planetary redox states ranging from extremely anoxic ($pO_2 = 10^{-16}$) to 100 bars of O_2 (Lincowski et al. 2018; Meadows et al. 2018). An organic haze formation scheme is used for reducing, methane-rich atmospheres as described in Pavlov et al. (2001b), Zerkle et al. (2012), and Arney et al. (2016). To more accurately model photochemistry for M-dwarf stellar hosts, Lincowski et al. (2018) updated *Atmos* with new UV cross sections and a higher-resolution spectral grid (100 cm^{-1}) for incoming stellar UV that better resolves stellar emission lines, such as Lyα.

Atmos is described in more detail in Meadows et al. (2018), and a comprehensive explanation of more recent updates can be found in Lincowski et al. (2018). Briefly, *Atmos* divides the nominal model atmosphere into plane-parallel layers and assumes hydrostatic equilibrium. A vertical transport scheme includes molecular and eddy diffusion. Boundary conditions can be set for all species at the bottom of the atmosphere, including fixed surface gas mixing ratios or surface humidity, outgassing fluxes, and surface deposition velocities. The top-of-atmosphere boundary for all species is assumed to be constant velocity determined by the diffusivity, while diffusion-limited flux is calculated for hydrogen.

Two primary templates were adopted for the experiments here: modern preindustrial Earth (no fluxes from industry) and Archean Earth. The modern (preindustrial) template uses 330 reactions and 81 species, 9 of which are considered in chemical equilibrium (i.e., short-lived, with no transport terms), and the Archean template uses 454 reactions and 83 species, 8 of which are short-lived. The modern Earth template includes chlorine chemistry, while the Archean template does not but has

---

[4] https://github.com/VirtualPlanetaryLaboratory/atmos

expanded hydrocarbon and sulfur networks (Domagal-Goldman et al. 2011), including haze formation (similar to Arney et al. 2016). In this work, these templates are used with different boundary conditions (i.e., surface fluxes) to simulate different planetary assumptions. The species and reaction templates are available in text format,[5] and the individual boundary conditions for each experiment are described in Section 3. A validation of these templates against modern Earth data is shown in Appendix B. The other templates are adapted and expanded from the core modern Earth template.

2.3. Coupled Climate–Chemistry Model Convergence

The climate and chemistry models are run independently and are loosely coupled via their inputs and outputs. The convergence criterion for VPL Climate is met when all atmospheric layers are flux balanced within $1\,W\,m^{-2}$ and the heating rate for each layer is less than $10^{-4}\,K\,day^{-1}$. The atmospheric chemistry model tracks changes in gas concentrations in each time step and computes the relative error. It adjusts the next time step based on the largest error (i.e., when the changes in mixing ratios are small, the next time step is increased). The model checks the time-step length, and when the elapsed time reaches 10^{17} s, the model is converged.

To run coupled climate–photochemistry experiments, we pass the converged profile from VPL Climate (temperature, gas mixing ratios, and eddy diffusion profiles) to the chemistry code, which is run to convergence. The modified gas mixing ratios from the chemistry code are then passed back to VPL Climate to compute a new equilibrium temperature structure and condensable gas mixing profiles. These profiles are then passed back to the chemistry model, and this process is repeated until global convergence (both photochemistry and climate) is achieved.

2.4. Model Inputs

Our climate and photochemical models require a number of inputs that tailor the model to the planetary atmosphere studied. Inputs include planetary properties (e.g., orbit, radius), atmospheric gas mixing ratios for each constituent in each layer, gas absorption properties (i.e., cross-section data and line lists), thermodynamic data for condensable gases, particle optical properties for aerosols, wavelength-dependent surface albedo data, and stellar spectral energy distribution (SED).

2.4.1. Planetary Properties and Model Atmospheres

Here we adopt the current best-fit orbital periods, radii, and masses of the TRAPPIST-1 planets (see Table 2 and Agol et al. 2021). We assume that the planets are in fixed, circular orbits.

The nominal planetary atmospheres in the climate and spectral models are 1D and plane-parallel, consisting of 64 pressure levels, 32 of which are from the surface to 10% of surface pressure, and the remaining layers extend to 0.01 Pa at the top of the atmosphere. The preindustrial modern atmosphere uses nonanthropogenic modern-day fluxes, which are relatively well-known. However, the different "Archean" atmospheres and biospheres considered here, although labeled as Archean, are not intended to be the most accurate known representation of periods in Earth's Archean. Instead, they

---
[5]　https://github.com/VirtualPlanetaryLaboratory/atmos

Table 2
Stellar and Planetary System Parameters as Model Inputs for TRAPPIST-1

Parameter	Modeled	Measured[a]
Star		TRAPPIST-1—2MASS J23062928–0502285
Mass ($M_\odot$)		0.0898 ± 0.0023
Radius ($R_\odot$)[b]	0.119	0.1192 ± 0.0013
Luminosity ($L_\odot$)[c]	0.000553	0.000553 ± 0.000019
Effective temperature (K)		2566 ± 26
Metallicity [Fe/H][d]		$+\,0.04 \pm 0.08$
Planets[a]	d	e
Period (days)[d]	4.0496	6.0996
Semimajor axis (AU)	0.02227 ± 0.00019	0.02925 ± 0.00025
Irradiation ($S_\odot$)	1.115 ± 0.043	$0.646^{+0.028}_{-0.025}$
Radius ($R_\oplus$)	$0.788^{+0.011}_{-0.010}$	$0.920^{+0.013}_{-0.012}$
Mass ($M_\oplus$)	0.388 ± 0.012	0.692 ± 0.022
Density ($\rho_\oplus$)	$0.792^{+0.028}_{-0.030}$	$0.889^{+0.030}_{-0.033}$
Gravity ($g_\oplus$)	0.624 ± 0.019	0.817 ± 0.024
Impact parameter b (R_*)	$0.0630^{+0.0627}_{-0.0435}$	$0.1907^{+0.0410}_{-0.0405}$

Notes. We use nominal values for our modeling. Error bars (1σ) are shown for reference. Standard errors on the period are smaller than the precision reported here. Irradiation is computed from the reported semimajor axis, assuming the luminosity quoted here.
[a] Data from Agol et al. (2021) unless otherwise noted.
[b] Data from Mann et al. (2019).
[c] Data from Ducrot et al. (2020).
[d] Data from Gillon et al. (2017).

---

provide starting templates of weakly reducing atmospheres and surface fluxes loosely compatible with the different metabolisms considered here. These atmospheres and biological fluxes are modified to self-consistency via the coupled climate–photochemical model, driven by the incoming stellar radiation from the TRAPPIST-1 host star. Consequently, despite having similar geological and biological surface fluxes to Earth's Archean, the converged atmospheric states of these models may no longer resemble Earth's Archean.

For the Archean biosphere, we assumed surface fluxes for CH_4 that are identical to those of present-day Earth (which includes fluxes from industry). This assumption is a reasonable one, albeit perhaps counterintuitive, as it is consistent with modeling efforts that have estimated that the Archean biological CH_4 flux (from a methanogen-acetogen ecosystem) was likely approximately 0.3–2.3 times the present Earth's CH_4 flux (Kharecha et al. 2005). However, specific measured constraints on CH_4 production in Earth's Archean are not available, and the link between CH_4 surface flux and the atmospheric abundance of CH_4 is intricately tied to environmental conditions and the possible presence of other metabolisms. For example, Ozaki et al. (2018) used biogeochemical models to show that the presence of anoxic photosynthesis, as well as the H_2 fluxes and Fe_2^+ to feed them, can greatly enhance the productivity of a methanogenic biosphere. For the sulfur-dominated Archean biosphere, we used up to 30 times Earth's current organic sulfur fluxes, for direct comparison with the previously explored environment in Domagal-Goldman et al. (2011).

In comparison, for the atmosphere based on the modern preindustrial Earth, methane fluxes are approximately 1/3 of the modern biological-industrial flux (Seinfeld & Pandis 2006,

Section 2.4.2), and N_2O is also slightly reduced. Nonanthropogenic CO production for preindustrial Earth is approximately 1/3 that of modern Earth (Seinfeld & Pandis 2006, Section 2.4.5). These fluxes result in surface atmosphere concentrations consistent with ice core data (Haan & Raynaud 1998; Flückiger et al. 2002). In the Archean templates we exclude the (predominantly anthropogenic) CO and NO_x surface fluxes entirely. Ethane fluxes are included in all modeled environments as a geological flux of 3.0×10^8 molecules cm^{-2} (Nicewonger et al. 2016).

Methyl chloride on current Earth is measured at approximately 0.5 ppb, with a range of 0.4–1.2 ppb (Hu et al. 2010). Because surface fluxes of CH_3Cl are very uncertain, we calibrated a flux for CH_3Cl based on the measurements for HCl, the primary oxidation product, which results in a surface abundance of 0.7 ppb (see Appendix B).

For Archean cases with nonfixed CO_2, we use CO_2 flux measurements for volcanic ocean ridge outgassing (Marty & Tolstikhin 1998; 2.25×10^{10} molecules $cm^{-2} s^{-1}$), which resulted in atmospheric CO_2 values between 165 and 524 ppm, depending on the planet and its environment.

For comparison with the CO_2/CH_4 biosignature pair, we include a potential false positive from a cloudy prebiotic version of the Archean Earth with higher outgassing from a more reducing mantle, as proposed in Krissansen-Totton et al. (2018b). This case is not intended to represent a known period in Earth's history but is an extreme case used solely to explore the potential detectability and discrimination of this false positive. In this potential false-positive case, both outgassed CO_2 and abiotic CH_4 will be present, but the atmosphere will also contain abundant CO, which serves as the false-positive discriminant. In our models, this environment includes approximate ratios of fluxes for $CO_2:CO:CH_4:H_2$ based on calculations of the outgassing from Earth's early mantle with a plausibly reduced chemistry (Catling & Kasting 2017). To keep global temperatures at a habitable level, the environment modeled here used 200 times the CO_2 flux for volcanic ocean ridge outgassing as given above, and the other species' fluxes are scaled as follows: $H_2/CO_2 = 0.5$, $CO/CO_2 = 0.1$, and $CH_4/CO_2 = 0.01$.

As a final note, our simulations of TRAPPIST-1 d with an Archean-Earth-like atmosphere entered a nonhabitable runaway greenhouse state, and so we do not discuss environmental properties or biosignatures for the TRAPPIST-1 d Archean Earth case.

2.4.2. Gas Absorption Data

Gas absorption cross sections are calculated from three sources: vibrational-rotational transitions at visible and infrared wavelengths, continuum absorption from electronic transitions and predissociation bands at UV wavelengths, and dimer- and pressure-induced absorption bands at visible to infrared wavelengths. Absorption lines associated with vibrational-rotational transitions are calculated using the line-by-line model LBLABC (see Meadows & Crisp 1996; Crisp 1997; Meadows et al. 2018, for details) with the HITRAN2016 line database (Gordon et al. 2017), which assumes terrestrial isotopic abundances.

Collision-induced absorption data are used for CO_2–CO_2 (Moore 1972; Kasting et al. 1984; Gruszka & Borysow 1997; Baranov et al. 2004; Wordsworth et al. 2010; Lee et al. 2016), N_2–N_2 (Lafferty et al. 1996; Hartmann et al. 2017), and O_2–O_2

updated from HITRAN (Maté et al. 1999; Baranov et al. 2004; Tran et al. 2006; Spiering et al. 2011; Spiering & van der Zande 2012; Thalman & Volkamer 2013; Karman et al. 2018, 2019).

UV–visible cross section data are incorporated from a variety of primary sources available from the MPI-Mainz UV/VIS Spectral Atlas of Gaseous Molecules of Atmospheric Interest[6] (Keller-Rudek et al. 2013). A list of updated sources is given in Lincowski et al. (2018). Additionally, we have updated our H_2O UV cross section with new data from Ranjan et al. (2020).

For gases without comprehensive line lists (DMS, DMDS, CH_3SH), we employ cross-section files from the Pacific Northwest National Laboratories (PNNL) Northwest Infrared spectral database (Johnson et al. 2004). These cross-section data are from standard temperature and pressure (1 bar, 298 K). Therefore, the spectral bands produced for some of our modeled environments with these gases are not as accurate, particularly because transit spectroscopy generally probes cooler, lower-pressure regions of the atmosphere than the standard temperatures and pressures at which the cross sections were measured. Consequently, our absorption cross sections are likely to overestimate the strength of the absorption of these three species.

2.4.3. Aerosol Optical Properties

All our model cases include clouds and/or hazes, except for a clear-sky TRAPPIST-1 preindustrial Earth case that is used for comparison. The single-scattering optical properties of clouds and aerosols are defined in precomputed tables for a range of specific particle types. Each particle type (i.e., water cloud, ice cloud, or hydrocarbon hazes) is defined by its composition, associated wavelength-dependent refractive indices, and its particle size and shape distributions. Given these properties, a single-scattering model was used to compute the wavelength-dependent extinction and scattering efficiencies (Q_{ext} and Q_{abs}) and the phase function moments (for Mie scattering) or the particle asymmetry parameter (g, for fractal hazes) used in our radiative transfer calculations.

For Earth-like clouds, we specify cirrus (water-ice) and stratocumulus (liquid-water) clouds, each nominally of cumulative optical depth $\tau = 0.15$ and 2.1, respectively. Here we have updated our cloud aerosol properties since Meadows et al. (2018). For cirrus clouds, the optical properties from B. Baum's Cirrus Optical Property Library (Baum et al. 2014) are used, as in Meadows et al. (2018); however, we have processed and include up to 200 Legendre polynomial phase moments per wavelength interval. The particles consist of a distribution of 45% solid columns, 35% plates, and 15% 3D bullet rosettes, spanning 2–9500 μm with a cross-section-weighted mean radius of 50 μm. Phase moments add a more accurate representation for these nonspherical particles compared to the Henyey–Greenstein phase function used previously. Stratocumulus cloud optical properties are based on refractive indices of water from Segelstein (1981) and calculated using Mie scattering theory, using a two-parameter gamma distribution ($a = 2.0$, $b = 0.118$) resulting in a mean particle radius of 1.53 μm and effective radius of 2.0 μm. This distribution is narrower and with a smaller density of large-radius particles compared to previous work (see Robinson et al. 2011;

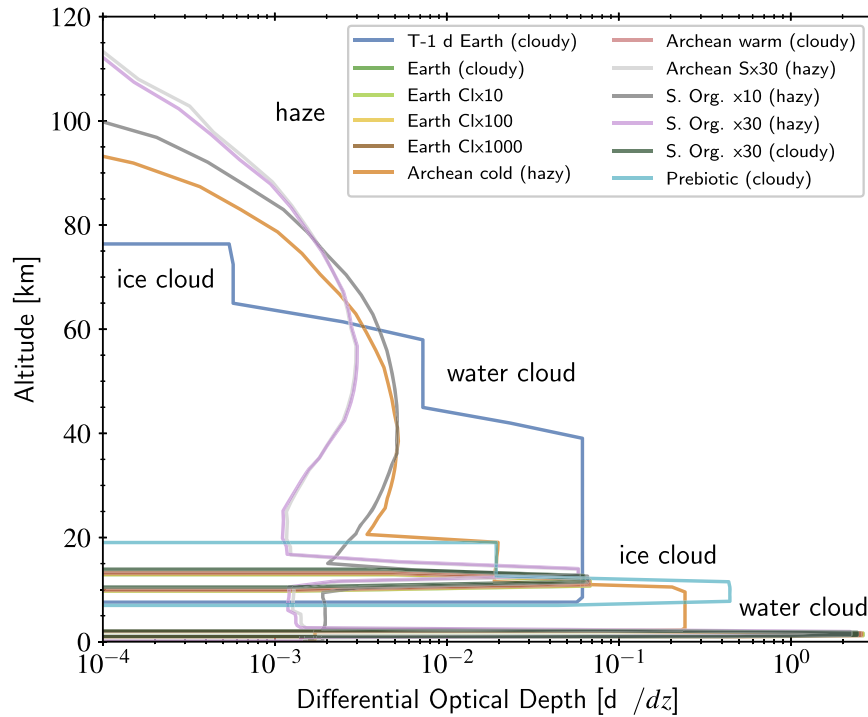
6 https://www.uv-vis-spectral-atlas-mainz.org/uvvis/

Figure 1. Calculated aerosol differential optical depth (optical depth per kilometer of altitude) profiles for our modeled TRAPPIST-1 d and e environments. The aerosol optical properties used and the calculation of cloud-layer optical depths and altitudes are described in Section 2.4.3. The TRAPPIST-1 d Earth-like environment is warmer than the true Earth (modern Earth orbiting the Sun), and its condensation water clouds form at higher altitudes. The cold Archean climate is modeled with higher, more distributed ice clouds, due to the much colder temperatures, and has a smaller total optical depth, due to reduced overall condensation. Except for the cold Archean and the additional haze optical depths, cumulative cloud optical depths are $\tau = 2.25$.

Meadows et al. 2018), and it improves the globally averaged greenhouse forcing in our climate model for Earth-like cases. Our calculated aerosol properties for the cases considered here are plotted in Figure 1.

We specify vertical profiles for cloud optical depth based on the modeled environment. Our standard profile is that employed for the VPL Spectral Earth model of Earth observing data (Robinson et al. 2011), namely an ice cloud at 0.3 bar and a water cloud at 0.85 bar. These cloud altitudes are used for our Archean and Earth-like environments. Our cloud altitudes and optical depths for the TRAPPIST-1 d Earth-like case and for the cold TRAPPIST-1 e Archean environment are modified from this standard because the tropospheric temperature profiles for these cases diverge materially from Earth. In these cases, we specify cloud altitude ranges corresponding to condensation altitudes in our mixing-length convection model. For layer temperatures with condensation below 235 K, we specify ice clouds, and for warmer layers, we specify water clouds. This is consistent with supercooled water clouds in the atmosphere of Earth (Wallace & Hobbs 2006). Due to the warming and self-evaporation of ice clouds for TRAPPIST-1 d and the small condensation fluxes at temperatures below 235 K, for this planet we specify a small optical depth of $\tau = 0.01$ for ice clouds and $\tau = 2.24$ for water clouds, to maintain a total optical depth of $\tau = 2.25$, as used for our Earth validation. For the cold Archean environment, the condensation rates are smaller than in our Earth validation, and a larger fraction of condensation is in cold layers, so the ice clouds are specified with $\tau = 0.25$ and the water clouds with $\tau = 0.5$, for a smaller total optical depth of $\tau = 0.75$. Higher ice optical depths result in layer warming and suppressed condensation. The self-

evaporation is consistent with models of radiatively warming CO_2 ice clouds in early Mars models (Forget et al. 2013).

Overall, cloud-top altitudes (here defined as the altitude at which vertically integrated optical depth from above reaches optical depth 0.1) were approximately 11–12 km for Earth-like TRAPPIST-1 e and 76 km for Earth-like TRAPPIST-1 d. These cloud distributions resulted in lowest effective transits heights of 14 km in our haze-free simulations, and these altitudes were similar to, and in fact a few kilometers higher than, the lowest effective transit heights for terminator averages of clouds from similar 3D global climate model (GCM) environments (Fauchez et al. 2019).

Our hydrocarbon hazes are assumed to be fractal aggregates of 0.05 μm monomers, using the codes and methods described in Arney et al. (2016). The optical depths obtained by this method are added to those of the standard ice and water clouds. Our photochemical model calculates the effective monodisperse aerosol radii at every atmospheric layer given the coagulation, sedimentation, and diffusion timescales (see, e.g., Pavlov et al. 2001a) in phase equilibrium. In climate and spectral modeling, for each layer we bin the haze to the precomputed optical properties. The optical depth is the required layer-by-layer input into the climate and spectral models, which is computed as given in Arney et al. (2016). There were a number of caveats discussed by Arney et al. (2016) regarding the haze formation scheme we use. In particular, this scheme does not include oxygen or nitrogen in haze formation and so may underestimate the thickness of the haze in early Earth environments that include oxidizing species such as CO_2 (Trainer et al. 2006; DeWitt et al. 2009; Trainer 2013; Hörst et al. 2018; Ugelow et al. 2018).

2.4.4. Surface Spectral Albedo

Although transmission observations are not sensitive to the planetary surface, surface albedos can affect climate calculations, and so we set up our simulations to use different surface compositions matched to the simulated environment. However, our simulations showed that the surface albedos we assumed had very little effect on the climate outcomes. For modern Earth, we use the spatially integrated wavelength-dependent surface albedo from the VPL 3D Spectral Earth model (Robinson 2011), as described in Meadows et al. (2018). For the Archean-like simulations, to enhance ease of modeling, we assume that the Archean environments have a similar distribution of ocean, land, and ice to modern Earth, but without plants (see Meadows et al. 2018). The integrated, energy-flux-weighted surface albedos for these surfaces for our TRAPPIST-1 stellar spectrum are 0.112 (Earth) and 0.124 (Archean). We note that using the modern Earth's land fraction is unlikely to be a good representation of the actual Archean, which by 3 Ga may have had only 60%–70% of Earth's present volume of continental crust (Cawood et al. 2013; Hawkesworth et al. 2017). However, there are many results, using different techniques, that predict that the Archean may have had between 20% and 80% of the current Earth's continental crust (Korenaga 2018). Additionally, the Archean sea-ice fraction may have been lower owing to saltier oceans that drove a warmer climate and a reduced polar cap (Olson et al. 2022).

Nonetheless, our assumption of similar ice and continental coverage and distribution, although not historically accurate for the true Archean Earth, is unlikely to significantly change our climate results, given that even 50% cloud cover can also mitigate the impact of the surface albedo. To test this, we ran climate simulations for TRAPPIST-1 e for our assumed Archean land and ice distribution, versus the extreme case of an aqua planet with no continents or ice, and found only 3 K difference in surface temperature. Given the likely smaller albedo difference between the modern Earth and a true Archean land and surface-ice distribution, we expect the impact of our assumed surface continent distribution on overall climate and surface temperature to be significantly less than 3 K.

2.4.5. Stellar Spectra

Characterizing the climate and photochemistry and computing spectra and detectability all require a panchromatic stellar spectrum of TRAPPIST-1 (2MASS J23062928–0502285), and the available data on this star in the UV to IR are currently limited. Here we use a spectrum derived from an average of the three high-resolution panchromatic model spectra presented by Peacock et al. (2019), which were calibrated to different available photometric UV measurements. In sensitivity testing, we found that the differences in stellar UV for the three spectra did not have a material impact on photochemistry or corresponding transit spectra. Potentially spurious emission lines have been removed (S. Peacock, private communication). See Figure 2 for the UV spectra of these model TRAPPIST-1 spectra, along with the solar UV for comparison.

2.5. SMART

To generate synthetic transmission spectra of our simulated inhabited environments, we use the SMART code. SMART is a 1D line-by-line, multistream, fully multiple-scattering radiative transfer model (Meadows & Crisp 1996; Crisp 1997;

Robinson 2017) that computes accurate synthetic planetary spectra. SMART has been validated against observations of solar system planets, including Mars, Earth, and Venus (Tinetti et al. 2005; Robinson et al. 2011; Arney et al. 2014). SMART requires a number of user inputs, including a pressure/altitude–temperature grid, gas mixing ratios, molecular absorption coefficients generated using the Line-By-Line ABsorption Coefficients (LBLABC) code (see Meadows et al. 2018) from line lists (e.g., HITRAN), collision-induced absorption data, UV–visible absorption cross sections, a stellar spectrum, and wavelength-dependent surface albedo data. We also incorporate hazes and clouds in our spectral simulations, which require inputs containing the altitude-dependent optical depths, as well as the particle asymmetry parameter and the extinction, scattering, and absorption efficiencies (Q_{ext}, Q_{scat}, and Q_{abs}). SMART can generate spectra at any arbitrary wavelength or spectral resolution and has been extensively validated against solar system observations including haze-covered worlds such as Titan in the visible–near-infrared (Robinson & Marley 2014) and Venus in the submillimeter (Lincowski et al. 2021).

2.6. Pandexo-noise Model

To determine the detectability of spectroscopic biosignatures with JWST, we adopt the techniques described in Lustig-Yaeger et al. (2019) and use the JWST time-series spectroscopy simulator `PandExo`[7] (Batalha et al. 2017, 2022) to model different observing modes and their associated noise sources. `PandExo` uses the Space Telescope Science Institute's Exposure Time Calculator, `Pandeia`[8] (Pontoppidan et al. 2016), to compute 3D data cubes for realistic point-spread function modeling, but we do not include systematic sources of error, and we assume no strict noise floor for JWST spectroscopy (see Greene et al. 2016).

Although Lustig-Yaeger et al. (2019) showed that the Near-InfraRed Spectrograph (NIRSpec) Prism sub512 ngroup6 mode was likely the most broadly sensitive for transmission spectroscopy of terrestrial exoplanet atmospheres, we also consider instrument capabilities that overlap and extend the NIRSpec wavelength range. We include the Near-Infrared Camera (NIRCam) using the F444W (3.880–4.986 μm) and F322W2 (2.430–4.013 μm) filters; NIRSpec using the G140M/H (0.7–1.27 μm), G235M/H (1.66–3.17 μm), G395M/H (2.87–5.27 μm), and Prism (0.6–5.3 μm) disperser combinations; the Near Infrared Imager and Slitless Spectrograph (NIRISS) using the single object slitless spectroscopy (SOSS; 0.6–2.8 μm) mode; and the Mid-Infrared Instrument (MIRI) low-resolution spectrometer (LRS; 5–12 μm). We also include a partial saturation strategy for the NIRSpec Prism, as described in Batalha et al. (2018) and Lustig-Yaeger et al. (2019), which increases the observing efficiency from 33.3% to 71.4% but assumes that data reduction techniques are able to recover the flux from partially saturated pixels by using only unsaturated groups up the ramp. See Table 1 of Lustig-Yaeger et al. (2019) for more information about each instrument and mode.

Our noiseless model spectra are generated at 1 cm^{-1} resolution, which is $R = 10,000$ at 1 μm, but for our detectability plots (Figures 9–18) they were binned using PandExo to $R = 20$, except for the NIRSpec G140H

---

[7] https://natashabatalha.github.io/PandExo/
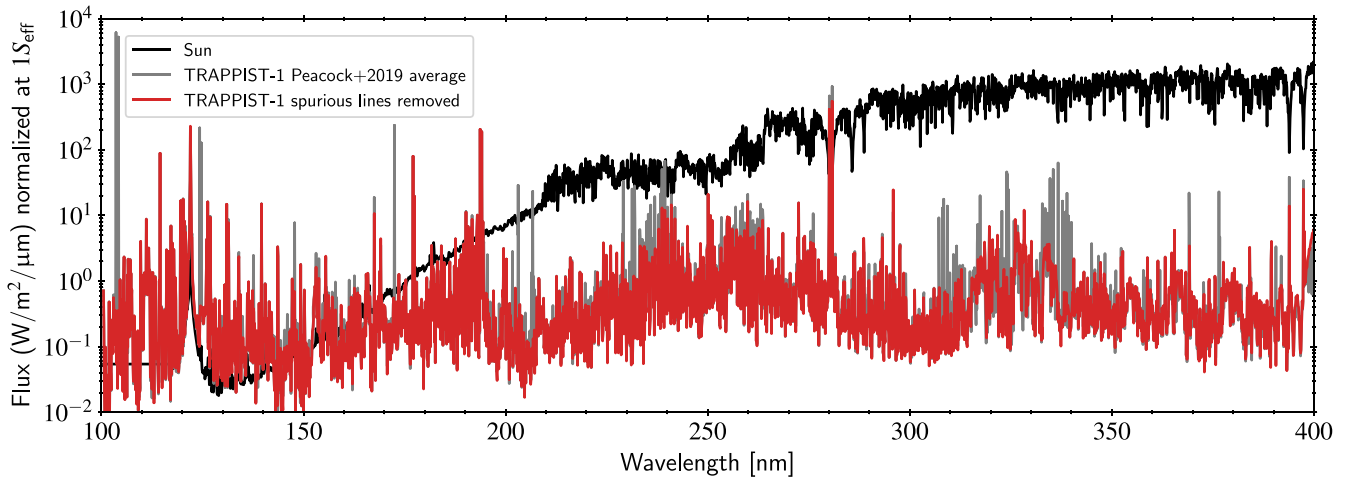[8] https://jwst.etc.stsci.edu/

Figure 2. UV spectra comparison, for the Sun (black), average of calibrated models from Peacock et al. (2019; gray), and the same model with spurious UV lines removed (red; S. Peacock, personal communication).

simulations, where $R = 40$ was used to better show the narrow O_2 band. These resolutions are at the lower end of the spectral resolution for the NIRSpec PRISM, which has $R \sim 30$–300 $\lambda/\Delta\lambda$. NIRSpec G140H has $R \sim 1300$–2300.

3. Results

We have modeled a series of atmospheric biosignatures in clear, cloudy, and hazy environments (Table 3 and Figure 1) that are informed by our understanding of different global Earth environments and dominant metabolisms through time. These include Archean-Earth-like TRAPPIST-1 e planets with a surface ocean and either a methanogenic biosphere (cloudy/hazy) or a methanogenic/sulfagenic biosphere (cloudy/hazy) and a modern-Earth-like (preindustrial), ocean-bearing TRAP-PIST-1 e (and d), with biospheres containing both methanogenesis and oxygenic photosynthesis (clear and cloudy). For TRAPPIST-1 e, we also model modern-Earth-like environments with progressively enhanced CH_3Cl fluxes, which nominally simulate denser vegetation coverage over larger fractions of the globe than on present-day Earth. To serve as a potential false-positive environment for the CO_2/CH_4 biosignature, we also included a prebiotic atmosphere with enhanced volcanism from a more reducing mantle. Finally, for comparison with the more self-consistent preindustrial modern Earth interacting with the TRAPPIST-1 host star, we also modeled a non-self-consistent version of TRAPPIST-1 e (same planetary size and orbit) that uses the temperature/pressure profile and vertical gas abundances of the current Earth, which are produced via photochemical and climate interaction with the Sun (a G2V dwarf).

In the following subsections we present results for the habitable/inhabited environments listed in Table 3 for our climate and photochemical atmospheric models (Section 3.1), simulated transmission spectra (Section 3.2), and JWST atmospheric (Section 3.3) and biosignature (Section 3.4) detectability estimates.

3.1. Coupled Climate and Photochemistry Model Results

Our modeled surface temperatures are provided in Table 3, the temperature profile and gas profiles for the TRAPPIST-1 d preindustrial Earth are shown in Figure 3, and the atmospheric vertical temperature structures for inhabited versions of

TRAPPIST-1 e are shown in Figure 4. Our Archean TRAPPIST-1 d simulation entered a runaway greenhouse state and became uninhabitable and so is not included here.

3.1.1. Climate and Atmospheric Composition for TRAPPIST-1 d

Our TRAPPIST-1 d preindustrial modern Earth maintained a hot, but potentially habitable, 302 K surface with only 280 ppm of CO_2. This climate stability may be due to the low CO_2 abundance and a relative lack of greenhouse gases overall, as well as cooling from an anti-greenhouse induced by the 4.5 ppm CH_4 abundance. CH_4 can absorb incoming stellar radiation at high altitudes, and it has been proposed that this could induce an anti-greenhouse effect on planets orbiting M-dwarf stars, resulting in cooler surface temperatures (Ramirez & Kaltenegger 2018). It is also worth noting that this CH_4 abundance—although roughly threefold higher than Earth's—is much less than that found in the modeled TRAPPIST-1 e atmospheres, which typically contain 100 ppm or more. This is likely due to an enhanced destruction rate for CH_4 via the hydroxyl radical, which is more abundant in simulated TRAPPIST-1 d's moist, hot atmosphere.

However, this 302 K surface temperature is at the limit for a stable atmosphere as modeled by Kopparapu et al. (2017), who used 3D models, and with 1% stratospheric water vapor this atmosphere is in a moist greenhouse state (Kopparapu et al. 2016, 2017). In this state, the more evenly mixed water vapor column implies that the planet is able to lose water readily. Though it is emitting 317 W m^{-2} of thermal radiation, the model planet remains stable and does not enter a runaway greenhouse state. This outgoing thermal flux value is higher than the maximum greenhouse radiation limit of 282 W m^{-2} calculated by Goldblatt et al. (2013) using prescribed temperature profiles. Unlike Goldblatt et al. (2013), our climate calculations are self-consistent and take into account a realistic atmospheric composition, which includes N_2 and CO_2. These gases are known to modify the runaway greenhouse onset from that anticipated from a pure water vapor atmosphere (Chaverot et al. 2022). We also use the M-dwarf host star's stellar spectrum, which produces a different planetary temperature structure than that used in Goldblatt et al. (2013). Other differences in our approach include assuming a humidity profile similar to Manabe & Wetherald (1967), with declining

Table 3
Planetary Environmental Cases

Planet	Template	Surface	Type(s) of Haze/Clouds	Atmospheric Gases	Surface Temperature (K)
True Earth	Modern Earth	Earth composite	water, ice	78% N_2, 21% O_2, 400 ppm CO_2, trace H_2O, O_3, CH_4, N_2O	288
TRAPPIST-1 d	Preindustrial Earth	Earth composite	water, ice	78% N_2, 21% O_2, 280 ppm CO_2, H_2O, O_3, CH_4, N_2O, CH_3Cl, HCl	302
TRAPPIST-1 d	Archean Earth	Earth no vegetation	water, ice, organic haze	64%–97% N_2, 280 ppm CO_2, 1.75% CH_4, trace H_2O, H_2, CO, C_2H_6, C_2H_6S	runaway
TRAPPIST-1 e	Preindustrial Earth	Earth composite	none	73% N_2, 21% O_2, 5% CO_2, trace H_2O, O_3, CH_4, N_2O, CH_3Cl, HCl	282
TRAPPIST-1 e	Preindustrial Earth	Earth composite	water, ice	73% N_2, 21% O_2, 5% CO_2, trace H_2O, O_3, CH_4, N_2O, CH_3Cl, HCl	276
TRAPPIST-1 e	Preindustrial Earth $\Phi(CH_3Cl) \times 10$	Earth composite	water, ice	73% N_2, 21% O_2, 5% CO_2, trace H_2O, O_3, CH_4, N_2O, CH_3Cl, HCl	276
TRAPPIST-1 e	Preindustrial Earth $\Phi(CH_3Cl) \times 100$	Earth composite	water, ice	73% N_2, 21% O_2, 5% CO_2, trace H_2O, O_3, CH_4, N_2O, CH_3Cl, HCl	279
TRAPPIST-1 e	Preindustrial Earth $\Phi(CH_3Cl) \times 1000$	Earth composite	water, ice	73% N_2, 21% O_2, 5% CO_2, trace H_2O, O_3, CH_4, N_2O, CH_3Cl, HCl	286
TRAPPIST-1 e	Archean Earth (cold)	Earth no vegetation	organic haze, water, ice	99% N_2, 150 ppm CO_2, O_2, H_2O, H_2, CO, CH_4, C_2H_6, C_2H_6S, CH_3SH	267
TRAPPIST-1 e	Archean Earth (warm)	Earth no vegetation	water, ice	95% N_2, 5% CO_2, trace O_2, H_2O, H_2, CO, CH_4, C_2H_6, C_2H_6S, CH_3SH	275
TRAPPIST-1 e	Archean Earth $\Phi(DMS,CH_3SH) \times 30$	Earth no vegetation	organic haze, water, ice	99% N_2, trace O_2, 358 ppm CO_2, CH_4, H_2O, H_2, CO, C_2H_2, C_2H_4, C_2H_6, C_3H_8, CS_2, C_2H_6S, $C_2H_6S_2$, CH_3SH	299
TRAPPIST-1 e	Archean Earth $\Phi(DMS,CH_3SH,H_2S,CS_2) \times 10$	Earth no vegetation	organic haze, water, ice	99% N_2, trace O_2, 165 ppm CO_2, CH_4, H_2O, H_2, CO, C_2H_2, C_2H_4, C_2H_6, C_3H_8, CS_2, C_2H_6S, $C_2H_6S_2$, CH_3SH	282
TRAPPIST-1 e	Archean Earth $\Phi(DMS,CH_3SH,H_2S,CS_2) \times 30$	Earth no vegetation	organic haze, water, ice	99% N_2, trace O_2, 524 ppm CO_2, CH_4, H_2O, H_2, CO, C_2H_2, C_2H_4, C_2H_6, C_3H_8, CS_2, C_2H_6S, $C_2H_6S_2$, CH_3SH	300
TRAPPIST-1 e	Archean Earth $\Phi(DMS,CH_3SH,H_2S,CS_2) \times 30$	Earth no vegetation	water, ice	94% N_2, 5% CO_2, trace O_2, CH_4, H_2O, H_2, CO, C_2H_2, C_2H_4, C_2H_6, C_3H_8, CS_2, C_2H_6S, $C_2H_6S_2$, CH_3SH	281
TRAPPIST-1 e	Prebiotic Earth (low redox volcanism, 200× enhanced)	Earth no vegetation	water, ice	89% N_2, 1.9% CO_2, 4.4% CO, 4.8% H_2, 14 ppm CH_4, trace O_2, H_2O	262

Note. True Earth denotes the modern Earth orbiting the Sun, and this case is provided for comparison with the TRAPPIST-1 planetary results. Here Φ is the surface flux in molecules $cm^{-2} s^{-1}$, so the descriptions indicate enhancement factors to surface fluxes for particular gases. Additional information about the template validations is given in Appendix B, and the templates are available online at https://github.com/VirtualPlanetaryLaboratory/atmos, in the photochemical input files.
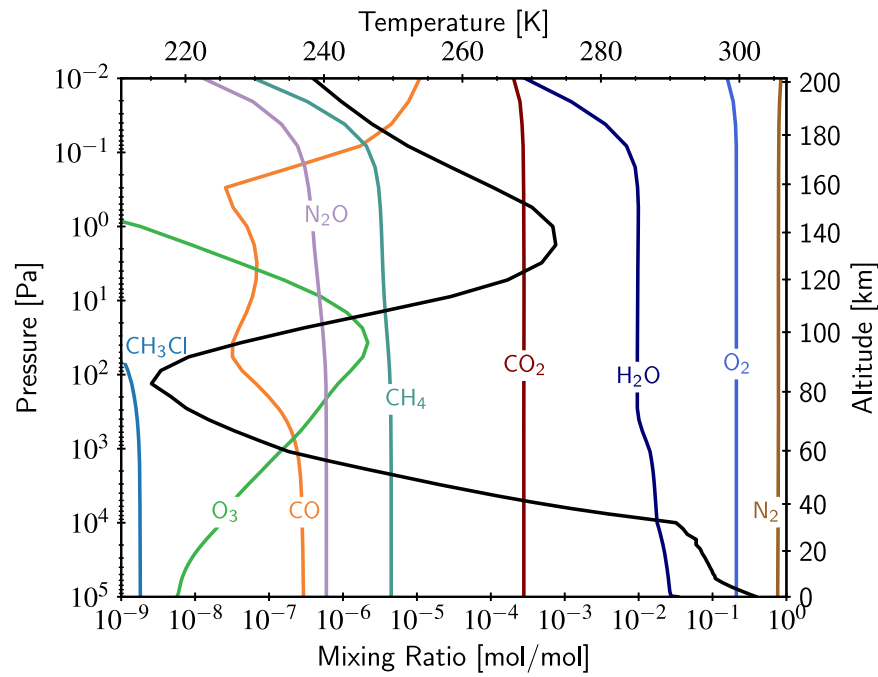
Figure 3. TRAPPIST-1 d temperature (black line) and modeled photochemical equilibrium species profiles for the cloudy modern preindustrial Earth-like atmosphere. Due to the higher atmospheric temperature and lower gravity of TRAPPIST-1 d, the atmosphere is significantly extended in the vertical direction, with a stratosphere spanning 80–140 km. Water is also nearly evenly mixed throughout the vertical column.
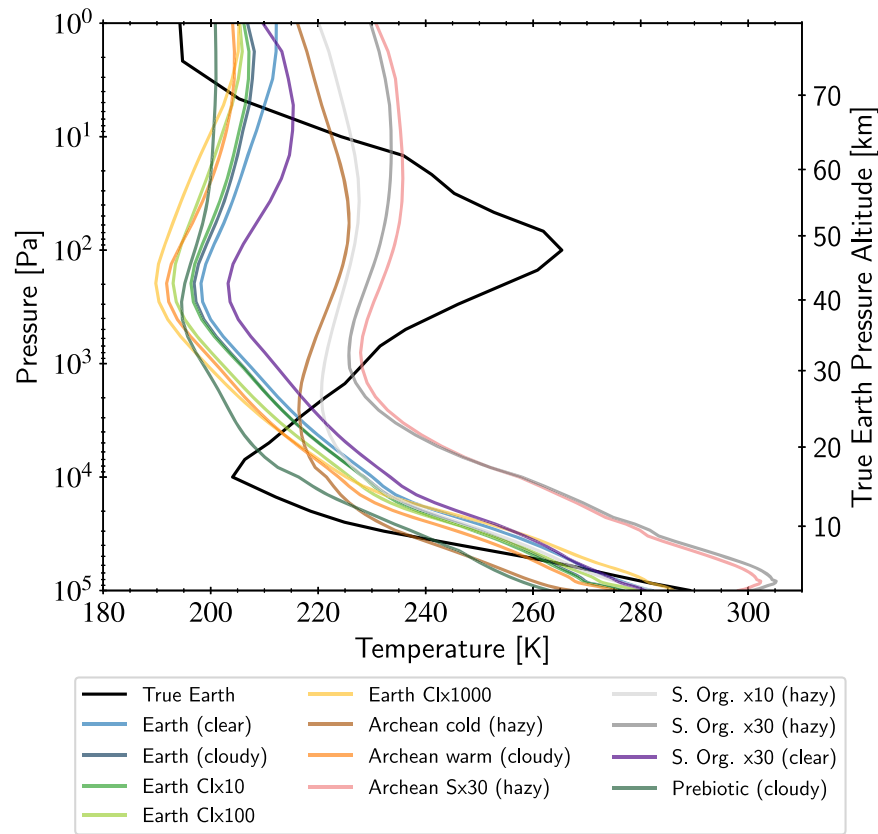

Figure 4. TRAPPIST-1 e modeled climates, with the true Earth's (modern Earth orbiting the Sun) climate for comparison (black line). Many cases exhibit a secondary cold trap at 100–300 Pa. However, the cases with enhanced sulfur fluxes and low CO_2 exhibit haze absorption heating, which results in a long adiabat, high cold trap, and mild stratosphere. In addition, the greenhouse heating of hydrocarbon and reduced sulfur gases in the atmosphere counter the anti-greenhouse of the haze to the extent that Earth-like levels of CO_2 maintain a temperate surface. Although increasing Cl levels also decrease CH_4 abundance, those planets generate lower stratospheric H_2O, with a net cooling of the stratospheres and heating of the surface. The altitude scale for Earth is provided for rough comparison.

humidity with height to the tropopause (see Appendix A), rather than a saturated adiabat, as assumed in Goldblatt et al. (2013). Furthermore, our clouds are prescribed to be consistent with the altitudes of global atmospheric condensation. We note that this approximation does not take into account the possible 3D distribution of the clouds, including whether or not clouds are present at the substellar point or blanket the nightside (Turbet et al. 2021), and either phenomenon is known to influence whether an atmosphere descends into a runaway greenhouse (Kopparapu et al. 2017; Wolf 2017). In preliminary sensitivity testing, we find that the cloud optical depth has the greatest effect on overall planetary albedo and whether TRAPPIST-1 d enters a runaway greenhouse or remains stable.

The vertical temperature structure for the TRAPPIST-1 d preindustrial Earth is also unusual when compared to those of the TRAPPIST-1 e planets (see below) in having a marked stratosphere, which is due to the radiative effects of H_2O, rather than O_3. For Earth, the stratosphere is generated by UV–visible absorption by ozone, but for TRAPPIST-1 d we calculated the climate and thermal structure with and without O_3 and found a less than 0.1% change in solar or thermal fluxes at any layer in the atmosphere, showing that O_3 had no material impact on the thermal structure. In comparison, a review of the line-by-line layer-by-layer spectral absorption map showed that at stratospheric altitudes absorption was dominated by water vapor for wavelengths in the near-infrared peak of the stellar emission, identifying it as the driver of the stratospheric inversion. Stratospheric heating is enhanced for TRAPPIST-1 d, compared to our other modeled TRAPPIST-1 planets, because, in addition to the larger insolation, the water vapor profile shows a very shallow drop-off in abundance with altitude from 3.4% near the surface, maintaining a relatively high 1% mixing ratio throughout the stratosphere and thermosphere. Although similar in temperature to Earth's stratospheric peak, TRAPPIST-1 d's arrives at about 2 Pa, 140 km, rather than Earth's 100 Pa, 47 km.

While ozone is not a contributor to the climate of the TRAPPIST-1 planets, it could still be important as a potential spectral discriminant. For TRAPPIST-1 d, abundant water vapor enhances the destruction of O_3, which produces a stratospheric bulge of ozone that is an order of magnitude less than those produced on the TRAPPIST-1 e planets. The temperature structure is also significantly extended in the vertical, due to the overall higher temperatures of the atmosphere and the lower gravity of TRAPPIST-1 d.

3.1.2. Climates of TRAPPIST-1 e

Although TRAPPIST-1 d's 280 ppm of CO_2 allowed it to avoid a runaway greenhouse state, that CO_2 abundance was too low to support habitability for the more distant TRAPPIST-1 e environments, which required either 5% CO_2 or biogenically produced greenhouse gases to maintain robustly habitable surface temperatures. For the preindustrial Earth cases, all surface temperatures remained above 273 K—but only with the addition of 5% CO_2. However, for the inhabited Archean model cases, 5% CO_2 was not required, as biogenically produced greenhouse gases such as DMS, methyl mercaptan (CH_3SH), and other hydrocarbons (primarily ethane but also C_2H_2, C_2H_4, C_3H_8, and DMDS) raised the simulated planetary surface temperature as high as 300 K, and at least as high as 267 K. These temperatures are all well above the 256 K limit needed to avoid a global snowball and maintain a non-ice-

covered ocean fraction (Charnay et al. 2013), especially around an M dwarf (Shields et al. 2013, 2014). The potential false-positive prebiotic Earth, with volcanic fluxes enhanced 200 times over Earth's, generated CH_4 at 14 ppm and CO_2 at 1.9% and had a lower, but still habitable, surface temperature of 262 K.

The complementary and additive effect of these different—and often biologically mediated—greenhouse warming mechanisms is demonstrated in the comparison between the "cold" Archean case with 150 ppm CO_2 and haze and the "warm" Archean case with 5% CO_2 and no haze, where both environments also had nominal Earth-like sulfagenic fluxes. These two environments produced an 8 K difference in surface temperature (267–275 K), which is driven primarily by their differences in CO_2 and biogenic hydrocarbon abundance. In the cold Archean case, the higher CH_4 abundance cools the planet via an anti-greenhouse effect (see Ramirez & Kaltenegger 2018), and the majority of greenhouse warming is from H_2O. However, the extremely low CO_2 abundance (150 ppm) enhances production of biologically generated trace hydrocarbons such as C_2H_2 and C_2H_6 (Arney et al. 2017, 2018), by removing a source of O that would remove CH_3 from the haze formation process. The increased hydrocarbons will produce additive greenhouse warming that is comparable to that generated by the 150 ppm CO_2. In the warm Archean case, CO_2 and H_2O vapor instead dominate greenhouse warming, and the high CO_2 abundance additionally suppresses the buildup of hydrocarbons (Arney et al. 2017), minimizing their contribution to surface warming.

The vertical temperature profiles (Figure 4) for the atmospheres modeled for TRAPPIST-1 e are strongly affected by the atmospheric composition, especially in the stratospheric regions preferentially probed by transmission observations. In particular, the Archean planets with a haze layer produce warmer and more isothermal stratospheres compared to the haze-free atmosphere owing to absorption of radiation by the photochemically generated, but potentially biologically mediated, haze (see Figures 1 and 5). After a small temperature inversion near the surface for the 30xS and 30xSorg cases, the lower atmospheres of the hazy planets show a long adiabat and a high cold trap due to the greenhouse heating of the lower atmosphere by hydrocarbon and reduced sulfur gases, which counter the anti-greenhouse effect of the high-altitude haze. This temperature structure also allows water vapor to extend higher in these atmospheres. The nonhazy environments have a more complicated structure, with both modern-Earth-like and Archean planets exhibiting dry convection that is confined to the planetary boundary layer (PBL) near the surface, with moist convection from the top of the PBL to about 10^4 Pa. Whereas Earth has a cold trap and a stratosphere, instead these planets exhibit a smaller, radiative lapse rate to about 100 Pa. The (nonhazy, but cloudy) prebiotic early Earth environment had a similar profile, but at much lower temperatures overall owing to a lack of greenhouse warming.

The TRAPPIST-1 e cases with more modern-Earth-like atmospheres (Figure 4) do not show the strong stratospheric temperature inversion due to O_3 that is typically seen in Earth's atmosphere near 10^4–10^3 Pa. This is due primarily to the small flux of visible light photons from TRAPPIST-1 in the ozone Chappuis band (0.5–0.7 μm) compared to that received at Earth from the Sun (see Meadows et al. 2018, their Figure 2). Instead, a cold trap and temperature inversion is formed at higher
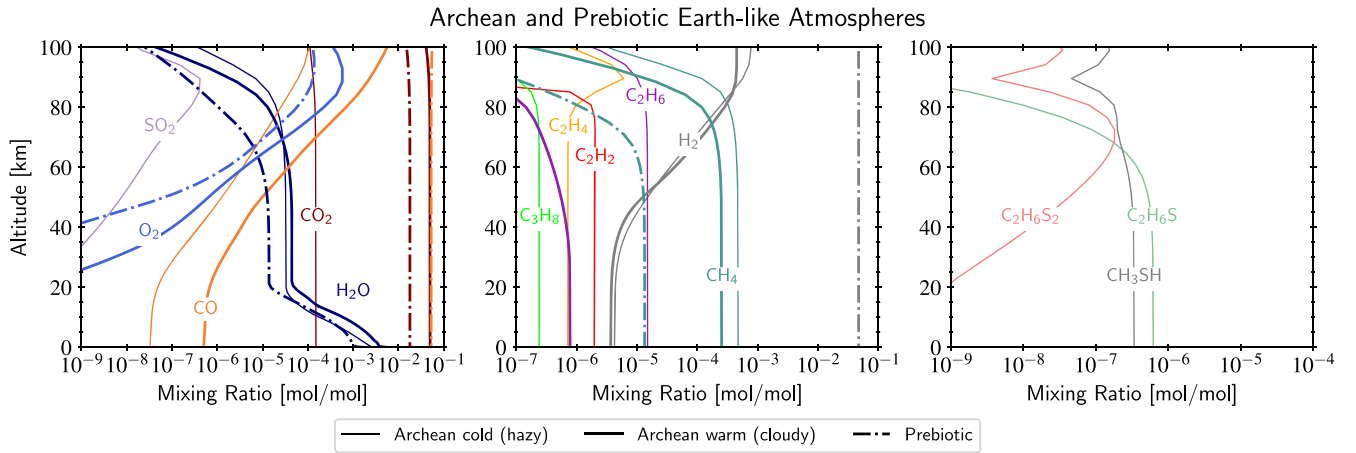
Archean and Prebiotic Earth-like Atmospheres

Figure 5. TRAPPIST-1 e modeled photochemical equilibrium species profiles for inhabited Archean and a prebiotic Earth-like atmosphere with enhanced volcanism (line types), for oxygen-bearing compounds (left panel), hydrocarbons (middle panel), and sulfur-bearing compounds (right panel). The Archean warm planet and the prebiotic planet both have water clouds, and the Archean cold planet has both water clouds and a photochemically generated hydrocarbon haze. The prebiotic planet does not contain a biosphere and shows the atmospheric abundances expected for vigorous outgassing from a more reducing mantle. Note that the warm Archean CO_2 and prebiotic atmosphere CO overlap at approximately 5% abundance in the left panel.

Sulfur-Enhanced Archean Earth-like Atmospheres
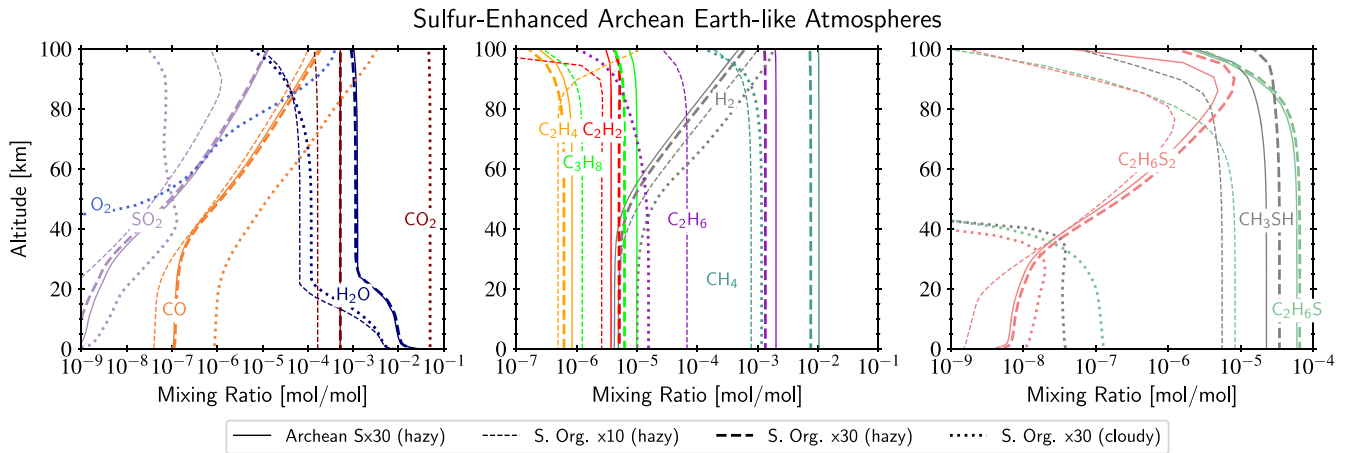
Figure 6. TRAPPIST-1 e modeled photochemical equilibrium species profiles for sulfur-enhanced Archean-Earth-like atmospheres, for oxygen-bearing compounds (left panel), hydrocarbons (middle panel), and sulfur-bearing compounds (right panel). Four different Archean-Earth-like atmospheres with enhanced sulfur fluxes are plotted in each panel (line types) for dominant methanogenic and sulfur biospheres and with clouds or hazes.

altitudes ($P < 10^2$ Pa), where the temperature increases with altitude owing to CO_2 bands absorbing TRAPPIST-1's predominantly near-infrared radiation (see also Lincowski et al. 2018). For the TRAPPIST-1 e Earth-like atmospheres with increased CH_3Cl fluxes, the direct destruction of CH_4 by chlorine (Figure 7) cools their stratospheres, reducing stratospheric water vapor abundance owing to the reduced cold trap temperature. These CH_3Cl-enhanced atmospheres also show increased heating at the surface, which is possibly due to higher atmospheric transparency due to the lower overall H_2O abundance. This higher-altitude, non-ozone-mediated temperature inversion is also seen strongly in the temperature structure for the higher-insolation TRAPPIST-1 d modern Earth planet (Figure 3), where heating by water vapor (black) extends to far higher altitudes than the O_3 bulge (green).

3.1.3. Atmospheric Compositions for Archean TRAPPIST-1 e

The vertical atmospheric compositions for oxygen-bearing, hydrocarbon, and sulfur molecules for the prebiotic volcanic and methanogenic Archean-Earth-like planets are shown in Figure 5, and those for the sulfagenic Archean are shown in Figure 6. For

the inhabited environments, we consider only photochemical generation of O_2, O_3, and CO, with only a net sink of CO and no active (e.g., geological) CO surface flux. In the prebiotic Archean case we assume a volcanic flux of CO from a chemically reduced mantle as described in Section 2.4.1. While the volcanic outgassing produces a very high abundance of CO in the prebiotic atmosphere ($\sim$5%), it is notable that CO also builds up in the upper atmosphere in all of the inhabited (with no surface CO flux) Archean cases, primarily due to CO_2 photolysis. Oxygen, produced by photolysis of CO_2, also builds up as a tenuous high-altitude bulge in the nonhazy cases, but O_3 is only seen at atmospheric abundances below 1 ppb and is not shown. In the inhabited Archean cases, the CO, O_2, and O_3, although present, are not at sufficiently high abundance to produce readily observable features in transmission at JWST wavelengths (see Section 3.4). In Figures 5 and 6 we also see upper atmosphere generation of SO_2 and H_2, potentially as by-products of photolysis and oxidation of sulfur-bearing hydrocarbons such as DMS and photolysis of stratospheric CH_4. The water vapor profiles are dependent on atmospheric temperature and follow the vertical trends seen in the corresponding temperature–pressure profiles.
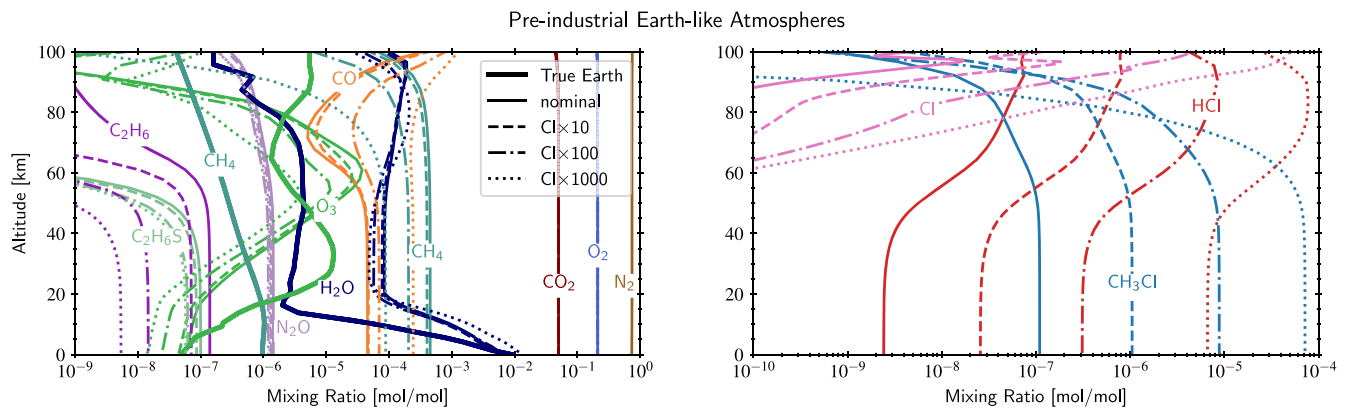
Pre-industrial Earth-like Atmospheres

Figure 7. TRAPPIST-1 e modeled photochemical equilibrium species profiles for cloudy modern-Earth-like atmospheres with nominal and enhanced CH$_3$Cl surface fluxes. The modern-Earth-like clear-sky case is not shown here but is similar to the nominal (cloudy) case. The left panel shows all climatically or spectrally relevant species except CH$_3$Cl and HCl, which are shown in the right panel, along with key radical Cl. True Earth vertical profiles for H$_2$O, O$_3$, and CH$_4$ (thick lines in the left panel) are shown for comparison.

For the biosignature gases methane (CH$_4$), ethane (C$_2$H$_6$), DMS (C$_2$H$_6$S), and methyl mercaptan (or methanethiol, CH$_3$SH), higher abundances are found in the hazy cases compared to those with clouds only (Figures 5 and 6). Since the CH$_4$ surface flux is fixed at the same value in all of the inhabited Archean cases, any differences in CH$_4$ atmospheric abundance (for all but the prebiotic case) in the middle panel of Figures 5 and 6 are due to chemistry. CH$_4$ is the most abundant trace gas in these atmospheres (up to 1%) and exhibits a higher vertical extent and abundance for the four hazy cases, presumably due to shielding from photolysis by the haze. Correspondingly, CH$_4$ is significantly depleted for the cloudy haze-free cases, dropping more than an order of magnitude in abundance between the 30 times sulfur organic flux case and the warm Archean case. The warm Archean haze-free case with 5% CO$_2$ shows a factor ~2 decrease in CH$_4$ compared to the low CO$_2$ abundance cold Archean (thick and thin solid teal lines in the middle panel of Figure 5), due to the higher atmospheric water vapor abundance in the warmer case, which generates more OH, the primary mechanism for CH$_4$ destruction in these atmospheres. In the false-positive prebiotic/enhanced volcanism scenario, even with 200 times Earth's volcanic flux from a mantle with a reduced chemical composition (see Section 2.4.1), atmospheric CH$_4$ builds up to only 14 ppm. This is many times Earth's 1.9 ppm (Lan et al. 2023) abundance, but significantly lower than the TRAPPIST-1 e environments with biospheric fluxes.

This higher abundance of hydrocarbon and organic sulfur gases in the hazy cases rather than the cloudy ones can only be partly explained by the increased surface fluxes in the enhanced sulfur cases (middle and right panels of Figure 6), and the majority of the effect is most likely due to shielding from the haze. Specifically, the surface fluxes in the enhanced sulfur cases are increased only 10–30 times, and yet the atmospheric abundances of these gases increase by at least two orders of magnitude, due to the UV shielding afforded by the haze. Ethane (C$_2$H$_6$), a potential biosignature that can be formed from recombination of methyl groups cleaved from sulfur organics like DMS (Domagal-Goldman et al. 2011), builds up to very high abundance in the haze-protected cases, reaching an atmospheric concentration of over 1000 ppm. C$_2$H$_6$S is also well protected by the haze and builds up to 10–50 ppm abundance in the hazy cases. Similarly, methyl mercaptan (CH$_3$SH) reaches values of 30 ppm. In the cases where a haze provides shielding from photolysis, DMS,

CH$_3$SH, C$_2$H$_2$, C$_2$H$_6$, and C$_3$H$_8$ become well mixed with altitude. In contrast to these gases, DMDS increases with abundance at higher altitudes because it is generated via reactions following photolysis of DMS and CH$_3$SH.

3.1.4. Atmospheric Compositions for Modern Preindustrial TRAPPIST-1 e

The vertical atmospheric composition of the modern-Earth-like TRAPPIST-1 e inhabited planets are shown in Figure 7, which illustrates the parent star's influence on planetary photochemistry, as well as the impact of introducing biologically produced CH$_3$Cl into Earth-like atmospheres. In Figure 7, the thick solid lines denote the true Earth profiles (Earth orbiting the Sun, a G2V star), and the thin solid lines give the composition of the nominal preindustrial TRAPPIST-1 e Earth, which is photochemically self-consistent with the incident TRAPPIST-1 (M8V star) stellar spectrum. The dashed, dashed–dotted, and dotted lines indicate photochemically self-consistent modern-Earth-like atmospheres with globally averaged Earth surface fluxes of CH$_3$Cl that are enhanced by 10, 100, and 1000 times, respectively. The enhanced CH$_3$Cl fluxes considered here inject more chlorine into the photochemical system, which results in several significant changes to the chemistry of the nominal Earth. The largest differences are to the primary Cl-bearing species, HCl, and the biogenic gas CH$_3$Cl, which increase by orders of magnitude at the surface, as the CH$_3$Cl surface fluxes increase. However, their vertical distribution is markedly distinct, with CH$_3$Cl dropping off significantly in the stratosphere owing to photolysis and HCl, its stable photolytic by-product, increasing to form a bulge in the upper stratosphere.

The increased CH$_3$Cl also has strong effects on several important trace gases, including CH$_4$, O$_3$, and CO, and weaker effects on other biosignature gases such as N$_2$O and C$_2$H$_6$S. The 1000 times enhanced CH$_3$Cl flux reduces the abundance of CH$_4$ by a factor of five from the nominal case and similarly increases the abundance of CO. As CH$_3$Cl is increased, CH$_4$ destruction increases, catalyzed by Cl derived from CH$_3$Cl, and at higher CH$_3$Cl levels, this becomes the dominant destruction mechanism for CH$_4$. As expected from our knowledge of Earth atmospheric science and the chlorine catalytic destruction of ozone (Seinfeld & Pandis 2006), we see that ozone is depleted by nearly two orders of magnitude as the CH$_3$Cl surface flux increases.
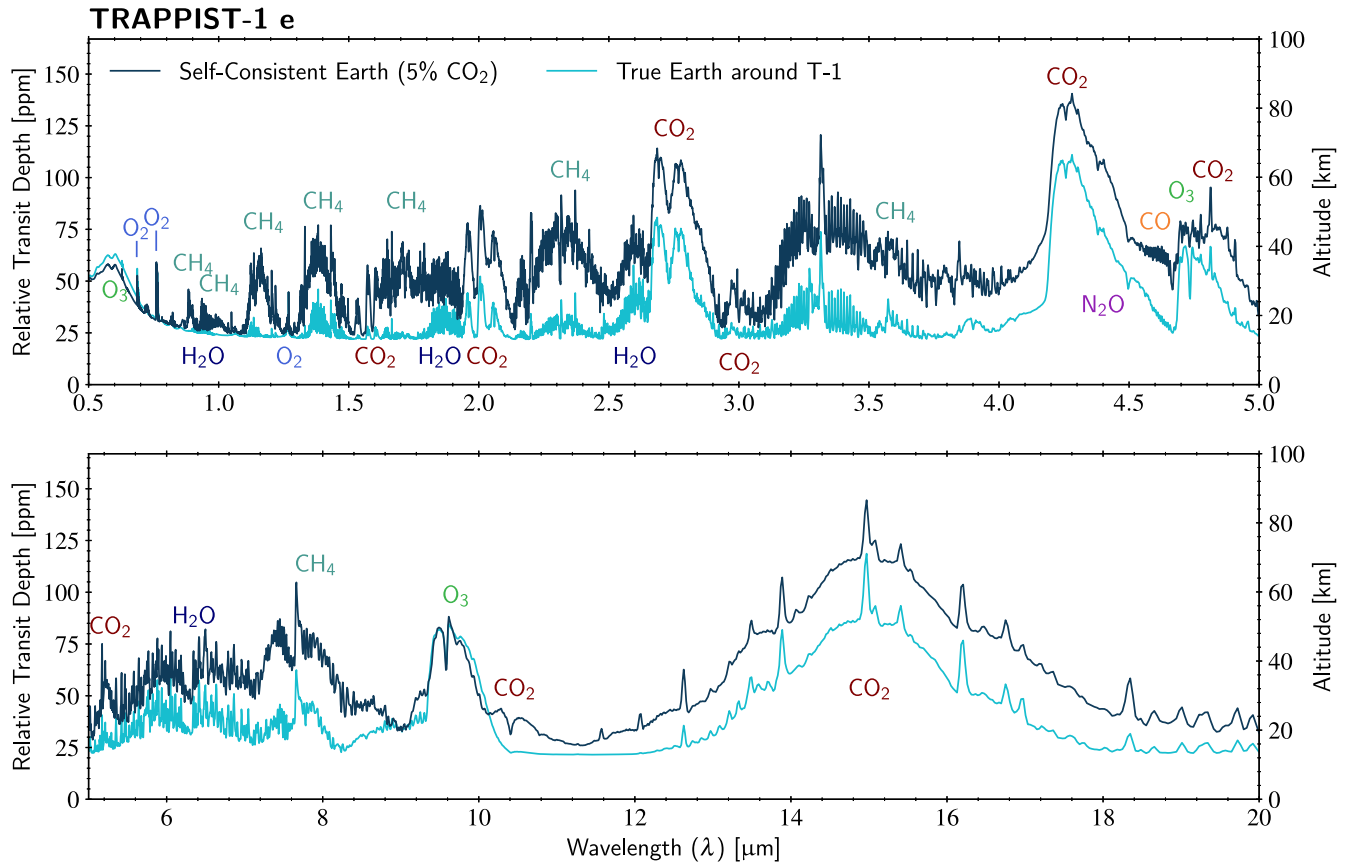
Figure 8. Comparison of the transmission spectrum (at 1 cm^{-1} resolution, $R = 10,000$ at 1 μm) for TRAPPIST-1 e with the temperature and gas abundance profiles of the true Earth (cloudy Earth orbiting a G dwarf; cyan line), which is not photochemically self-consistent with the spectrum of TRAPPIST-1, vs. the cloudy preindustrial Earth case, which is photochemically self-consistent with the spectrum of TRAPPIST-1 and has similar clouds (dark-blue line). For the same surface flux, the self-consistent preindustrial Earth produces much stronger CH$_4$ features owing to higher atmospheric abundances under favorable chemistry driven by the TRAPPIST-1 stellar spectrum. The CO$_2$ features for our self-consistent Earth are larger only as a result of requiring a higher abundance to remain temperate.

The TRAPPIST-1 e preindustrial Earth-like cases generate an ozone bulge at higher altitudes than Earth's, due to the UV spectrum of the TRAPPIST-1 star. This altitude shift is driven by changes in the effectiveness of key destruction processes for O$_3$ both above and below the bulge altitude. Above the bulge, there is a lower rate of direct photolytic O$_3$ destruction owing to the lower M-dwarf near-UV (NUV) compared to the Sun. Below the bulge, O$_3$ destruction is governed by catalysts that are mediated by water vapor and chlorine.

3.2. Model Transmission Spectra

To assess the detectability of potential biosignatures with JWST, we used the self-consistent simulated TRAPPIST-1 d and e biosphere/atmospheres described above to generate transmission spectra, which were then analyzed using PandExo to determine the detectability of specific molecular and haze features. In this section we describe the molecular and haze signals seen in the simulated transmission spectra, and in Section 3.4 we assess the detectability of these signals after JWST-relevant noise has been added.

3.2.1. Comparing Spectra for Self-consistent and Non-self-consistent TRAPPIST-1 e

Figure 8 provides a demonstration of the importance of modeling atmospheric composition using photochemistry that is self-consistent with the UV spectrum of the host star. This

figure compares the transmission spectra for a photochemically and climatically self-consistent cloudy Earth-like TRAPPIST-1 e (dark blue) with a true modern Earth atmosphere (i.e., gas abundances, clouds and climate), but on a planet of TRAPPIST-1 e's size and orbital configuration (cyan). In the self-consistent TRAPPIST-1 Earth case, Earth's biological and geological gas surface fluxes were allowed to interact with the incident TRAPPIST-1 stellar spectrum (with the exception of CO$_2$, which is fixed at 5% to maintain a temperate surface), whereas the true Earth version used the temperature profiles and mixing ratios of the current Earth (which interacts with the spectrum of the Sun, a G-dwarf star). In both cases the clouds form at a similar pressure level in the atmosphere.

While the O$_2$ and O$_3$ features remain comparable, the most prominent difference seen in the two spectra is the relative strength of the CH$_4$ bands. This difference is not due to cloud effects, as the clouds form at similar atmospheric levels and produce similar continuum levels in the spectra. Nor is the difference due to the CH$_4$ surface flux, which is identical in both cases. The differences in the strengths of the CH$_4$ features are instead due to the increased photochemical lifetime for CH$_4$ under TRAPPIST-1's M8V stellar insolation, compared with the G2V insolation for the true Earth case (Segura et al. 2005; Rugheimer et al. 2015). This longer photochemical lifetime results in a higher atmospheric abundance of CH$_4$ for the TRAPPIST-1 case, which produces more prominent CH$_4$ spectral features, potentially enhancing the detectability of this
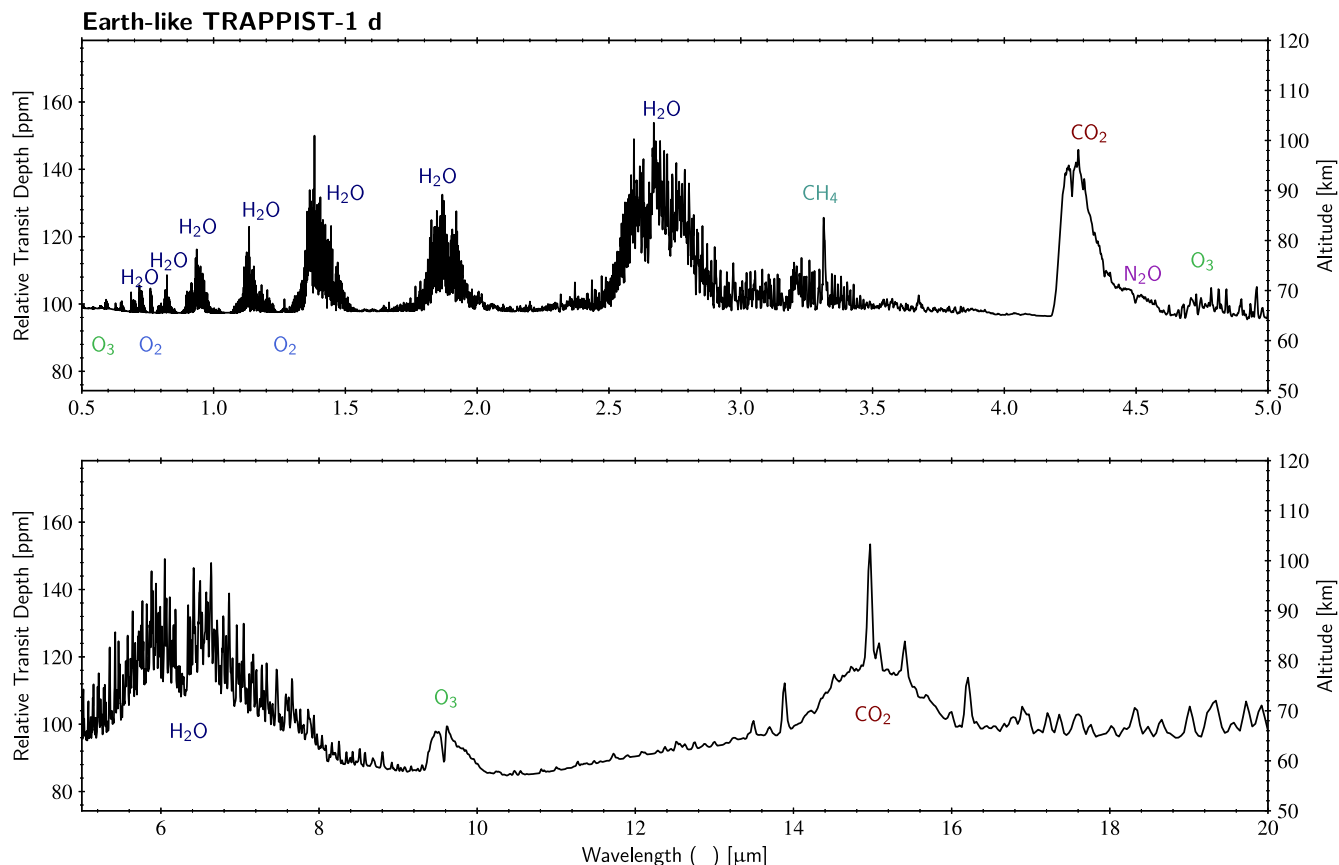
Figure 9. Transmission spectrum (at 1 cm^{-1} resolution, $R = 10{,}000$ at 1 μm) for the modern (preindustrial) Earth-like TRAPPIST-1 d. The high cloud deck truncates features throughout the spectrum, particularly the Chappuis band of ozone. The warmer and higher-altitude cold trap and subsequent higher stratospheric water vapor abundance produce additional visible-region water features and obscure the available CO$_2$ bands, except the strongest at 4.3 and 15 μm. The methane features are relatively weak owing to photochemical destruction via water photolysis and truncation of the absorption features by the formation of very high altitude water clouds. There is no Rayleigh scattering slope owing to the high-altitude cloud tops.

biosignature gas. Disparities in the strength of the CO$_2$ features are also seen, but this is due primarily to the difference in CO$_2$ abundance in the two atmospheres (400 ppm for the true Earth vs. 5% for the Earth-like TRAPPIST-1 e).

3.2.2. Common Spectral Features and the Effects of Clouds and Haze

Figures 9, 10, and 11 show the simulated transmission spectra for the TRAPPIST-1 d modern preindustrial Earth atmosphere, the TRAPPIST-1 e Archean atmospheres with methanogenic and sulfur biospheres (without the prebiotic case), and modern Earth atmospheres with oxygenic photosynthesis and methanogenesis, respectively. For TRAPPIST-1 d we show only the preindustrial Earth spectrum, as it was the only one of our TRAPPIST-1 d simulations to escape runaway. For the model spectra for TRAPPIST-1 d, note that there is no Rayleigh scattering slope seen in the shortwave, due to the high-altitude clouds that truncate the transmission spectra at lower pressure. For TRAPPIST-1 e, we show the nominal preindustrial modern Earth, as well as cases with enhanced CH$_3$Cl surface fluxes, nominally from vegetation.

These figures show the spectral impact of a number of key molecules that could either be associated with life or provide environmental context. In all spectra, CO$_2$ displays the most prominent bands at 2.7, 4.2, and 15 μm. Strong CH$_4$ features are seen in all the TRAPPIST-1 e simulations shown here, as the modeled CH$_4$ surface abundances ranged from 65 to close to 500 ppm (for comparison, Earth's current surface CH$_4$

abundance is close to 2 ppm). Strong CH$_4$ bands at 1.1 and 1.4 μm overlap with weaker bands from H$_2$O, potentially complicating water vapor retrieval, although H$_2$O bands near 2.4 and 6.3 μm produce stronger and cleaner features.

Figures 10 and 11 also show the differing impact of clouds and hazes on the sample of TRAPPIST-1 e spectra. For TRAPPIST-1 e modern preindustrial Earth-like planets, the transmission spectrum of the clear-sky Earth case probes to the deepest levels of the atmosphere, down to 7 km altitude (seen in the clear blue curve near 1.5 μm using the right-hand y-axis). As seen in Figure 11, clouds, rather than the effects of Rayleigh scattering and refraction, lift this spectral continuum to higher altitudes by truncating the transmission path near 15 km, as seen in the cloudy modern-Earth-like cases and also in Figure 10 for the cloudy but haze-free "Archean warm" case. This cloud cutoff is well above the refraction cutoff limit of 1 km altitude for TRAPPIST-1 e. Hazes, however, strongly truncate the transmission paths, and this effect is especially impactful at wavelengths shortward of 2.0 μm, where the transmission spectra probe no deeper than 50 km altitude, resulting in the marked slope seen between 0.5 and 2.0 μm for the hazy sulfur organic spectrum. However, the hazes have lower opacity at wavelengths longward of 4 μm. This combination of wavelength-dependent opacity in haze absorption perhaps nonintuitively combines to enhance the overall detectability of organic molecules (e.g., C$_2$H$_6$), as the haze protects them from photolysis at shorter wavelengths but still
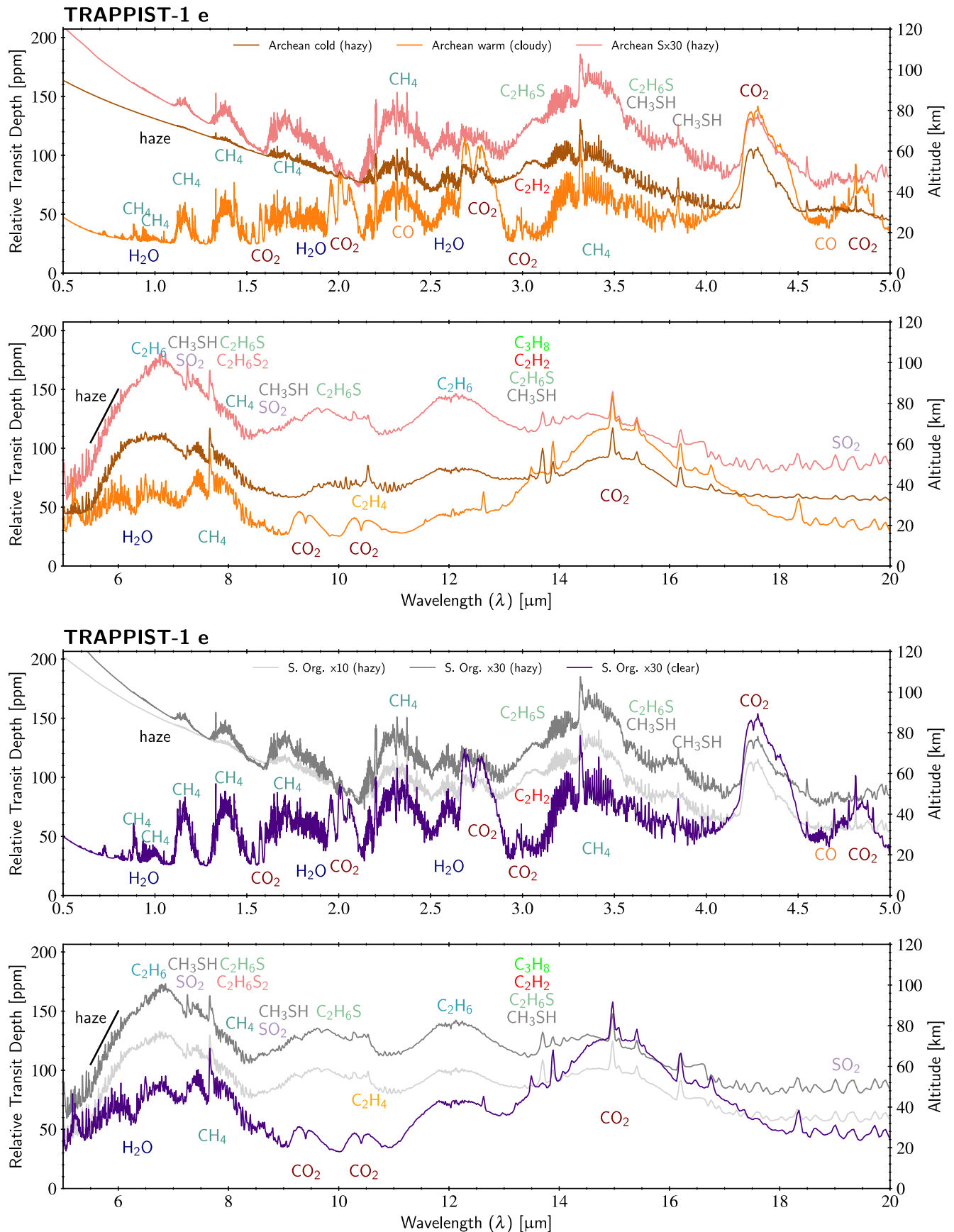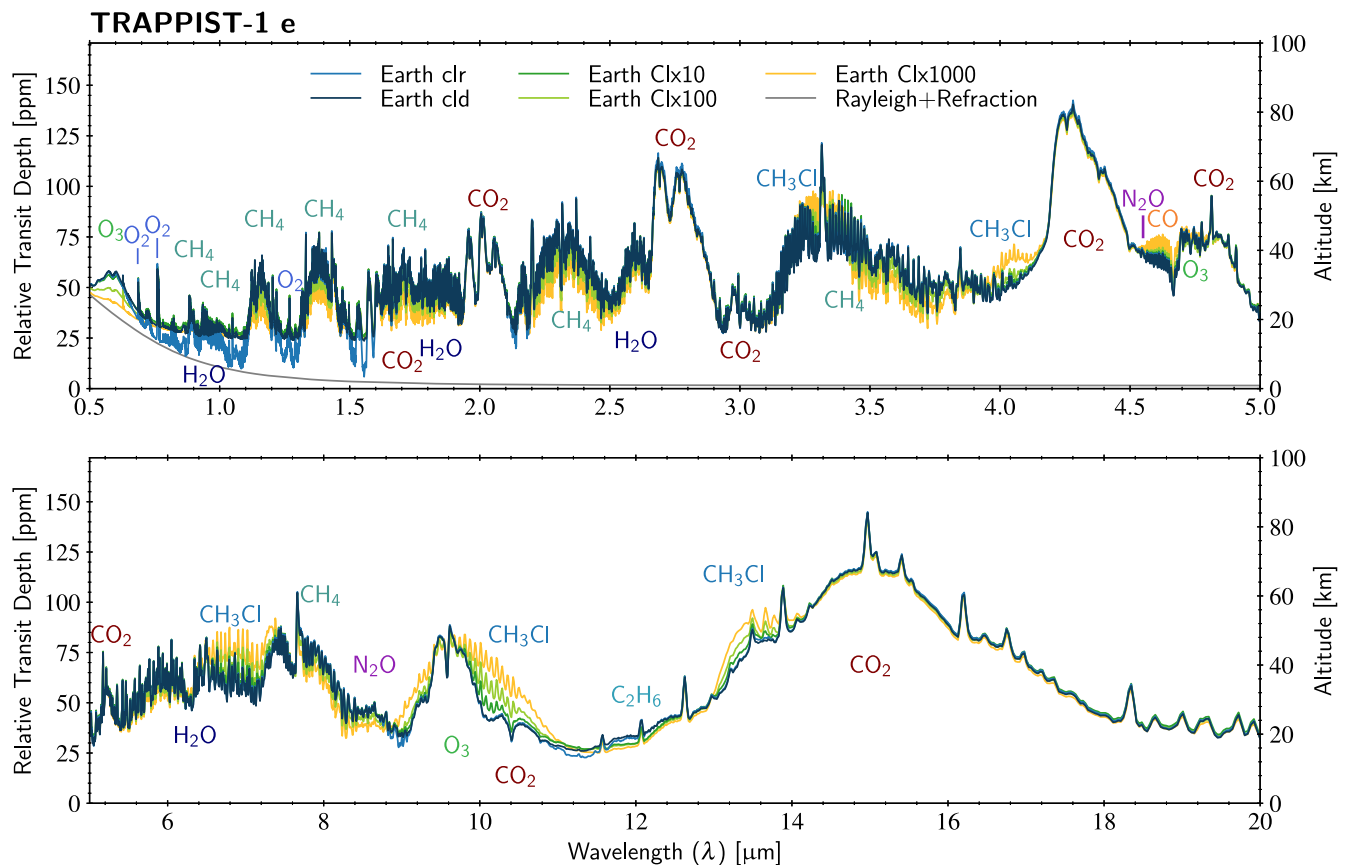
Figure 10. Transit transmission spectra (at 1 cm^{-1} resolution, $R = 10,000$ at 1 μm) of TRAPPIST-1 e Archean-like and enhanced sulfur organics environments. CH$_4$ and CO$_2$ produce some of the more detectable features, as well as hydrocarbon haze, which contributes substantially to the higher transit continuum at less than 3.2 μm and at 5.5–6.2 μm. There are also numerous hydrocarbon absorbers between 2–4 μm and 5–14 μm—not all contributing gases are labeled. In hazy atmospheres, the haze and organic molecules combine to form a strong pseudocontinuum from 8–15 μm.

Figure 11. Transit transmission spectra (at 1 cm^{-1} resolution, $R = 10,000$ at 1 μm) of modern (preindustrial) Earth-like TRAPPIST-1 e environments, and similar environments with increased fluxes of CH$_3$Cl. Strong features from CO$_2$ and CH$_4$ are seen, as well as weaker features from O$_2$, O$_3$, and N$_2$O. Increased CH$_3$Cl influences atmospheric chemistry by reducing the abundance of other biosignatures such as CH$_4$ and O$_3$, and it produces strong CH$_3$Cl spectral features only at fluxes orders of magnitude stronger than modern Earth. An additional (gray) line for Rayleigh scattering and refraction only is also shown. For TRAPPIST-1 e refraction has a negligible contribution (the transit height is less than 1 km), and Rayleigh scattering influences transit spectra predominantly in the visible.

allows strong transmission features from molecular absorption at longer wavelengths.

3.2.3. The TRAPPIST-1 d Preindustrial Earth Spectrum

Examining the potential signals produced by biosignatures in these planetary atmospheres, the simulation of TRAPPIST-1 d with a preindustrial Earth atmosphere (Figure 9) shows CH$_4$ signals that are swamped by strong water vapor absorption, except for a clean, although weak (10–20 ppm), CH$_4$ band at 3.3 μm. The O$_3$ signals are also relatively muted. This leaves the environmental context molecules H$_2$O and CO$_2$ as the most likely to be detected. This is despite the larger atmospheric scale height for this hot, low-gravity planet, which could potentially enhance the strength of molecular transmission features.

The suppression of CH$_4$ and O$_3$ is due to a combination of chemistry and cloud formation, both driven by the high water vapor abundance in this hotter atmosphere. The warmer, larger scale height atmosphere of TRAPPIST-1 d (Figure 3) allows water vapor to extend at high (percent) values to much higher altitudes. This abundant water vapor leads to production of the OH radical via water photolysis. Reactions with this radical (see Wunderlich et al. 2019) reduce the photochemical accumulation of CH$_4$ to $\sim$20 ppm and result in a smaller column depth of O$_3$ compared to those of the TRAPPIST-1 e planets. Additionally, the formation of a high cloud deck in this warmer, wetter atmosphere leads to the truncation of the

TRAPPIST-1 d transmission spectrum at 70 km altitude, narrowing the molecular features and reducing their amplitude. However, because the atmospheric scale height is much larger than that of the TRAPPIST-1 e planets, the molecular features are still relatively large, despite the high-altitude truncation, with water features of 50 ppm relative transit depths, although the CH$_4$, O$_3$, and even CO$_2$ features are still significantly weaker when compared to their TRAPPIST-1 e counterparts. Overall, the environmental context indicators H$_2$O and CO$_2$ are the strongest features, with the higher stratospheric water vapor abundance producing multiple H$_2$O features, and some that even obscure weaker CO$_2$ bands.

3.2.4. TRAPPIST-1 e Spectra

For TRAPPIST-1 e, each atmosphere/biosphere combination produces its own distinctive suite of molecules, which, if detectable (see Section 3.4), could be used to help identify the presence of a biosphere. In the spectra of the Archean atmospheres (Figure 10), with methanogenic biospheres and either enhanced sulfur fluxes or a suite of biologically produced sulfur organic fluxes from a sulfur biosphere, the strongest individual biosignature features are from CH$_4$ and CO$_2$, especially for the cloudy, nonhazy cases. However, several hydrocarbons, including ethane (C$_2$H$_6$), DMS, and CH$_3$SH, produce strong and broad features in the mid-infrared. Strong features from C$_2$H$_6$ are seen near 7 and 12 μm, DMS (C$_2$H$_6$S) has a broad feature near 10 μm, and CH$_3$SH absorbs from 2.5
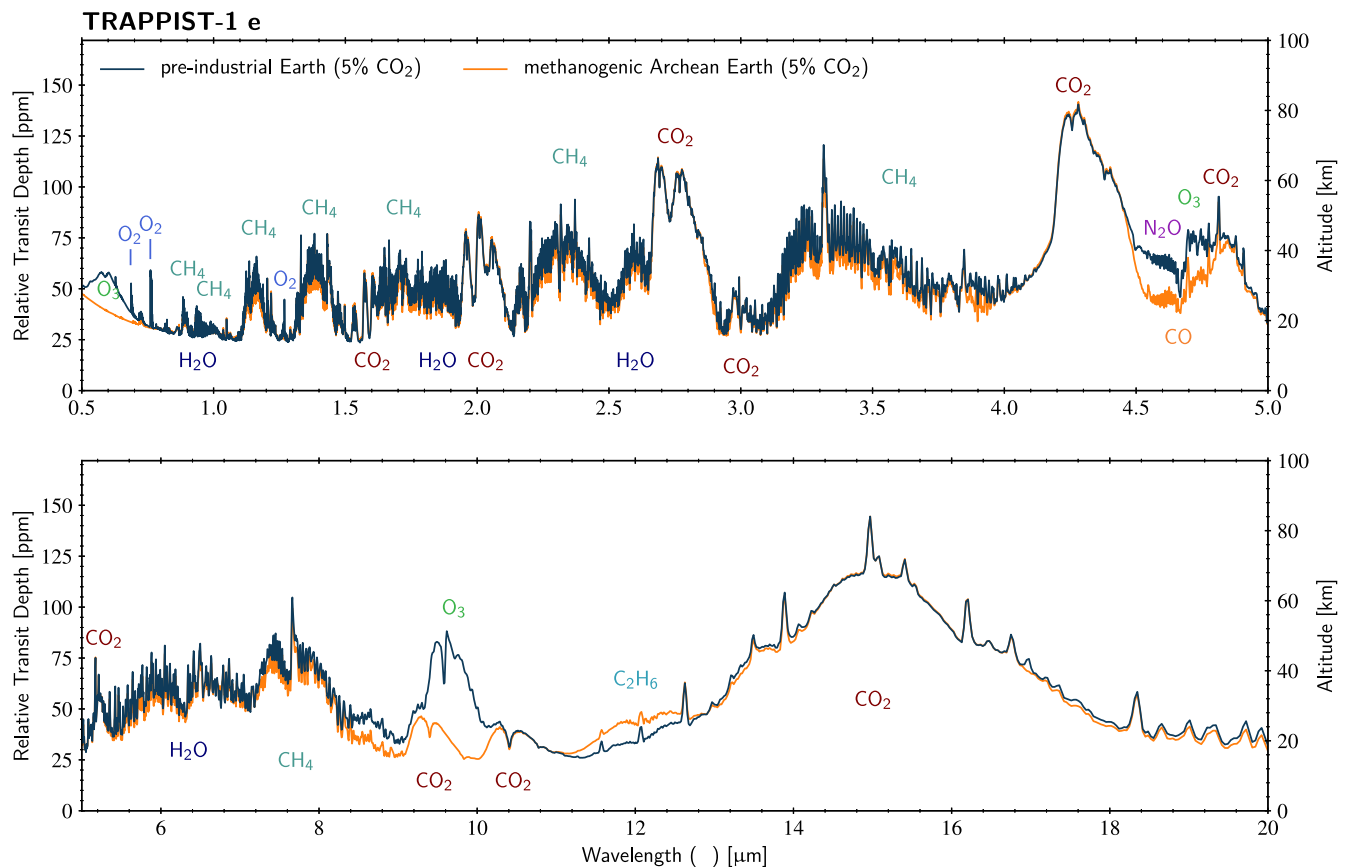
Figure 12. Comparison of the transmission spectrum (at 1 cm^{-1} resolution, $R = 10,000$ at 1 μm) for simulations of TRAPPIST-1 e with a preindustrial oxygenic Earth-like atmosphere (dark blue, 452 ppm CH$_4$) and a methanogenic, Archean-Earth-like atmosphere (orange line, 253 ppm CH$_4$), both with 5% CO$_2$. The environments produce similar CH$_4$ features, but modern Earth has O$_2$/O$_3$ features and the Archean produces sufficient C$_2$H$_6$ for a weak band at 12 μm. This result suggests that the CH$_4$ and CO$_2$ bands from methanogenesis can be a persistent feature throughout a planet's history.

to 4.0 μm. In hazy atmospheres—which have higher fluxes of organic molecules—at wavelengths shortward of 5 μm, the potential biosignatures with the strongest features again include CO$_2$ and CH$_4$ absorption longward of 2 μm, as well as the strong slope from the organic haze from 0.5 to 2.0 μm. This haze slope significantly reduces the height of the CH$_4$ features below 2.0 μm. A strong spectral absorption feature from organic haze can also be seen from 5.5 to 8 μm. The combined effects of absorption from haze and organic molecules also form a prominent pseudocontinuum from 8 to 15 μm.

For the TRAPPIST-1 e modern, preindustrial Earth biosphere (Figure 11), which supports both methanogenesis and oxygenic photosynthesis, the strongest potential biosignature features are still the simultaneous detection of CO$_2$ and methanogenic CH$_4$. Although the oxygenic-photosynthetic biosphere is highly productive and O$_2$ is present in these atmospheres at a high abundance (21%), O$_2$ produces distinctive, but very narrow and relatively weak, spectral features at short wavelengths near 0.68, 0.76, and 1.27 μm. O$_2$'s photochemical proxy, O$_3$, has broader and stronger features at 0.5–0.7, 4.7, and 9.6 μm, but these are still significantly weaker than those of CO$_2$ and CH$_4$. For the preindustrial Earth oxygenic-photosynthetic case with enhanced CH$_3$Cl fluxes up to 1000 times Earth's present-day value, the strongest CH$_3$Cl feature spans 9–11 μm and broadly overlaps the 9.6 μm O$_3$ band. Weaker CH$_3$Cl features can also be seen near 3.5, 4.1, 7.0, and 13.5 μm. It is also worth noting that the higher chlorine concentration in the CH$_3$Cl-enhanced

atmospheres chemically suppresses both the abundance of CH$_4$ and the overall column abundance of O$_3$, by up to an order of magnitude (see Figure 7). This suppression weakens the strength of the O$_3$ Chappuis band (0.5–0.7 μm), although absorption from the stronger O$_3$ 9.6 μm band remains largely unaffected.

In Figure 12, we compare the potential biosignatures for Earth-like planets over time, including the self-consistent modern Earth spectrum (without CH$_3$Cl enhancement) and the warm Archean without haze (Figure 12). Both spectra show strong CO$_2$ absorption, as both have 5% CO$_2$ added to maintain habitable surface temperatures. The strongest differences between the two spectra can be found in the presence of O$_2$/O$_3$ features in the modern Earth spectra, which are not seen in the Archean spectra. The modern Earth also shows a stronger CO absorption, and the Archean spectrum shows enhanced absorption from ethane. However, perhaps the most striking result is the similarity in strengths of the CH$_4$ bands in both cases, with the Archean—which here we have assumed has a 3× higher surface flux of CH$_4$ when compared to the modern preindustrial Earth—showing weaker CH$_4$ absorption features. This result suggests that the CH$_4$ generated by a methanogenic biosphere could have a similar photochemical lifetime and abundance in both reducing and oxidizing atmospheres and could continue to have a large impact on the near-infrared transmission spectrum, even after a planet has developed a dominant oxygenic-photosynthetic biosphere.
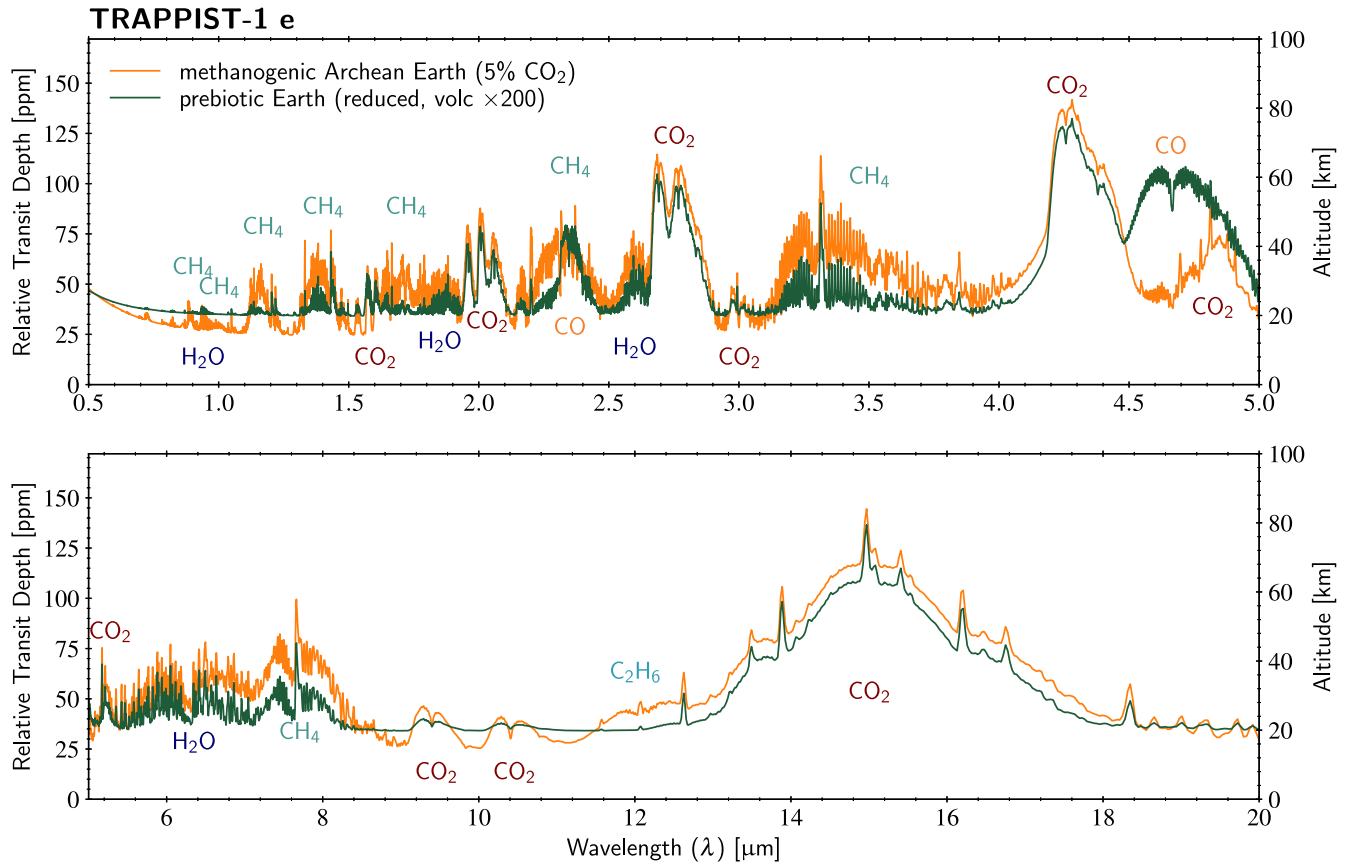
Figure 13. Comparison of the transmission spectrum (at 1 cm^{-1} resolution, $R = 10,000$ at 1 μm) for TRAPPIST-1 e for methanogenic, Archean Earth (orange line), with 5% CO_2, and a prebiotic Earth (dark green) with enhanced volcanic outgassing and 1.9% CO_2. Both environments exhibit strong CO_2 features, with the biogenic environment producing stronger CH_4 features. The prebiotic Earth is more easily distinguished by its large CO band at 4.6 μm.

Finally, in Figure 13, we show a comparison of the transmission spectra for TRAPPIST-1 e with a methanogenic, Archean Earth, versus the false-positive scenario of a prebiotic Earth with enhanced volcanism from a more reducing mantle (see Krissansen-Totton et al. 2018b). Both spectra exhibit CH_4 and strong CO_2 signals, but in one the methane is produced by methanogens, and in the other it is due to volcanic outgassing. In the prebiotic case, the abiotic CH_4 reaches a surface abundance of only 14 ppm, producing an absorption signal that is about half that expected from the 200 ppm of biologically generated CH_4 for the methanogenic early Earth. However, the largest difference between the two cases is the strong CO absorption from the 4.6 μm band, and to a lesser extent from the 2.3 μm band, that is present in the false-positive outgassing case (prebiotic)—and not present in the biological case.

3.3. Atmosphere Detectability with JWST

Having simulated a suite of environments and the molecular signals that may be present in their spectra, we now consider the potential detectability of these signals with JWST. Our detectability results are shown in Table 4, where each row corresponds to a different planetary environment. The last column lists the number of transits required for detecting the presence of an atmosphere and for any molecules that could be detected in fewer than 100 transits. For each planetary attribute, the number of transits required to achieve a weak sensitivity $\langle S/N \rangle = 3$ to spectroscopic features in the atmosphere is listed in parentheses, with a superscript corresponding to the JWST

instrument configuration applicable to that observation. If more than one instrument is capable of making the observation in fewer than 100 transits, then up to three instruments are listed, starting with the smallest number of transits to the largest.

The first step to characterizing terrestrial exoplanet atmospheres is to determine whether an atmosphere is in fact present. For the suite of inhabited planet environments/ biospheres that we have simulated, we apply JWST noise models to assess the detectability of their atmospheres by searching a transmission spectrum for deviation from a straight line as a function of wavelength, using the technique described in Lustig-Yaeger et al. (2019). This test is equivalent to ruling out a featureless spectrum at 3σ using a model with 1 degree of freedom. It does not identify specific molecular features, only the spectrum's deviation from a straight line. The results of this test are shown as the first element in the last column of Table 4, which lists the number of observed transits with JWST required to detect an atmosphere for that environment. Note that because TRAPPIST-1 d and e are temperate, rather than hot, JWST secondary eclipse spectroscopy cannot provide the signal-to-noise ratio (S/N) needed for robust constraints on the atmosphere via molecular absorption in thermal emission spectra (Barstow & Irwin 2016; Lustig-Yaeger et al. 2019). Consequently, we only consider atmosphere detection via transmission spectroscopy.

Our results indicate that most of the atmospheres considered in this work could be detected in just a few transits, despite the presence of hazes, which make detecting specific molecules more challenging. All of the photochemically self-consistent

Table 4
Detectability of the Atmosphere and Various Molecules in the Transit Transmission Spectrum of TRAPPIST-1 d and e Assuming Different Plausible Biosphere Templates, and the Number of Transits with Each Instrument Needed to Weakly Detect Them

Planet	Template	Molecules (Number of Transits to $\langle S/N \rangle \geq 3.0$)
T-1 e	True Earth (clr; no photochemistry)	Atmosphere(3[i], 4[h], 5[d]), O_3(57[d], 61[i], 77[e]), H_2O(6[i], 9[h], 10[d]), O_2(77[b]), CO_2(6[i], 7[d], 10[h]), CH_4(23[i], 35[h], 39[c])
	True Earth (cld; no photochemistry)	Atmosphere(4[i], 6[d], 7[h]), O_3(64[d], 69[i]), H_2O(58[i], 74[c], 89[h]), CO_2(7[i], 7[d], 11[a]), CH_4(76[i], 85[d])
T-1 d	Preindustrial Earth (cld)	Atmosphere(10[i], 16[h], 20[c]), H_2O(11[i], 15[c], 17[h]), CO_2(29[d], 35[i], 42[a])
T-1 e	Preindustrial Earth (clr)	Atmosphere(2[i], 3[h], 4[g]), H_2O(20[i], 25[e], 30[c]), CO_2(2[i], 3[h], 3[d]), CH_4(2[i], 2[h], 3[c])
	Preindustrial Earth (cld)	Atmosphere(2[i], 3[h], 4[d]), H_2O(37[e], 37[i], 43[c]), CO_2(2[i], 3[d], 4[h]), CH_4(2[i], 3[h], 4[c])
	Preindustrial Earth $\Phi(CH_3Cl) \times 10$	Atmosphere(2[i], 3[h], 4[d]), H_2O(38[i], 41[e], 45[c]), CO_2(3[i], 3[d], 4[h]), CH_4(3[i], 4[h], 4[c])
	Preindustrial Earth $\Phi(CH_3Cl) \times 100$	Atmosphere(2[i], 3[h], 4[d]),CH_3Cl(97[d]), H_2O(38[i], 46[c], 50[e]), CO_2(3[i], 4[d], 4[h]), CH_4(4[i], 6[h], 6[c])
	Preindustrial Earth $\Phi(CH_3Cl) \times 1000$	Atmosphere(2[i], 3[h], 4[d]), CH_3Cl(21[d], 23[i], 38[h]), H_2O(29[i], 38[c], 45[h]), CO(69[d], 70[i]), CO_2(3[i], 4[h], 5[d]), CH_4(7[i], 10[c], 11[h])
	Archean Earth (cold)	Atmosphere(2[i], 3[h], 4[g]), CO_2(17[d], 19[i], 25[a]), CH_4(13[i], 20[h], 21[c]), Haze(18[e]), HazeSlope(2[i], 4[h], 6[g])
	Archean Earth (warm)	Atmosphere(2[i], 3[h], 4[d]), H_2O(43[e], 46[i], 54[c]), CO_2(2[i], 3[d], 4[h]), CH_4(3[i], 4[h], 5[c])
	Archean Earth $\Phi(DMS,CH_3SH) \times 30$	Atmosphere(2[i], 3[d], 3[h]), H_2O(37[i], 50[c], 61[h]), CH_3SH(99[i]), C_2H_6S(96[i]), CO_2(25[d], 28[i], 38[a]), CH_4(5[i], 6[c], 7[h]), Haze(22[e]), HazeSlope(5[d], 6[i], 10[f])
	Archean Earth $\Phi(DMS,CH_3SH,H_2S,CS_2) \times 10$	Atmosphere(2[i], 2[h], 3[g]), CO_2(20[d], 23[i], 30[a]), CH_4(18[i], 23[c], 28[h]), Haze(21[e]), HazeSlope(2[i], 3[h], 4[g])
	Archean Earth $\Phi(DMS,CH_3SH,H_2S,CS_2) \times 30$	Atmosphere(2[i], 3[h], 3[d]), H_2O(43[i], 56[c], 69[h]), CH_3SH(50[i], 54[d], 85[h]), C_2H_6S(94[i]), CO_2(30[d], 33[i], 45[a]), CH_4(7[i], 8[c], 10[h]), Haze(28[e]), HazeSlope(4[i], 6[d], 7[h])
	Archean Earth (warm) $\Phi(DMS,CH_3SH,H_2S,CS_2) \times 10$	Atmosphere(2[i], 4[h], 4[d]), H_2O(62[i], 67[e], 69[c]),CO_2(3[i], 4[d], 5[h]), CH_4(3[i], 4[h], 5[c])
	Archean Earth (warm) $\Phi(DMS,CH_3SH,H_2S,CS_2) \times 30$	Atmosphere(2[i], 3[h], 4[d]), H_2O(35[i], 37[e], 41[c]), CO_2(2[i], 3[d], 3[h]), CH_4(1[i], 2[h], 2[c])
	Prebiotic Earth	Atmosphere(3[i], 4[d], 4[h]), CO(7[i], 8[d], 13[a]), CO_2(3[i], 4[d], 6[h]), CH_4(40[i], 44[d], 62[h])

Notes.
[a] NIRCam F444W.
[b] NIRSpec G140H.
[c] NIRSpec G235H.
[d] NIRSpec G395H.
[e] MIRI LRS.
[f] NIRISS SOSS substrip96.
[g] NIRSpec Prism sub512.
[h] NIRSpec Prism sub512s.
[i] NIRSpec Prism sub512 ngroup6.

inhabited atmospheres considered for planet e appear to be weakly detectable with NIRSpec Prism in two to three transits, with more confident 5σ detections possible in six to nine transits. The hazy Archean atmospheres remain detectable even though their molecular absorption features in the NIR are diminished because the hydrocarbon haze scattering slope causes the transit depths to drop by 50–100 ppm between 1 and 2 μm (see Figure 10). Consequently, the prospect of identifying the presence of ~1 bar, possibly inhabited atmospheres on TRAPPIST-1 d and e is likely within the capability of JWST.

3.4. Biosignature Detectability with JWST

To assess the detectability of specific gaseous molecules in the atmospheres of different TRAPPIST-1 d and e inhabited environments, we follow Lustig-Yaeger et al. (2019) and use simulations of JWST transmission spectra of the environments and compare these models to JWST transmission spectra of the same environment but with the target molecule removed. For molecules with multiple spectral features in an observed wavelength range, this technique can use all available spectral features for a given molecule—including collisionally induced absorption, if present—thereby enhancing detection sensitivity over single-band estimates. By using all molecular bands of a given species within an instrument wavelength range, this approach leverages similar spectroscopic information to that of atmospheric retrieval models. Our biosignature detectability results for spectra generated for all of our simulated inhabited environments are collected in Table 4, which lists the

molecules that may be detected in fewer than 100 transits with JWST in each spectrum. For each potentially detectable molecule, the number of transits to achieve $\langle S/N \rangle = 3$ on the contribution to the spectrum from that molecule is listed in parentheses, with a superscript corresponding to the JWST instrument and mode applicable to that observation. As for the atmosphere detection, if more than one instrument is capable of making the observation, then up to three instruments may be listed from the smallest to largest number of transits needed.

3.4.1. Haze Detectability with JWST

We also considered how to assess detectability of the organic hazes in our spectra, which can be biologically mediated and so can also serve as biosignatures (Arney et al. 2018). Table 4 provides detectability estimates for both the haze scattering slope and haze absorption features, labeled "HazeSlope" and "Haze," respectively. The detectability of the haze scattering slope refers to the number of transits needed to distinguish a best-fit power-law haze model from a best-fit flat featureless spectrum and is maximized for instruments with broad NIR wavelength coverage, such as NIRSpec Prism and NIRSS SOSS. The haze imparts such a significant scattering slope from 0.6 to 3 μm that its detection via scattering is relatively straightforward, requiring a comparable amount of observing time to detecting the presence of the atmosphere. However, to positively identify the source of the scattering slope as due to an organic haze, detection and identification of the haze absorption features would be needed. The method used to
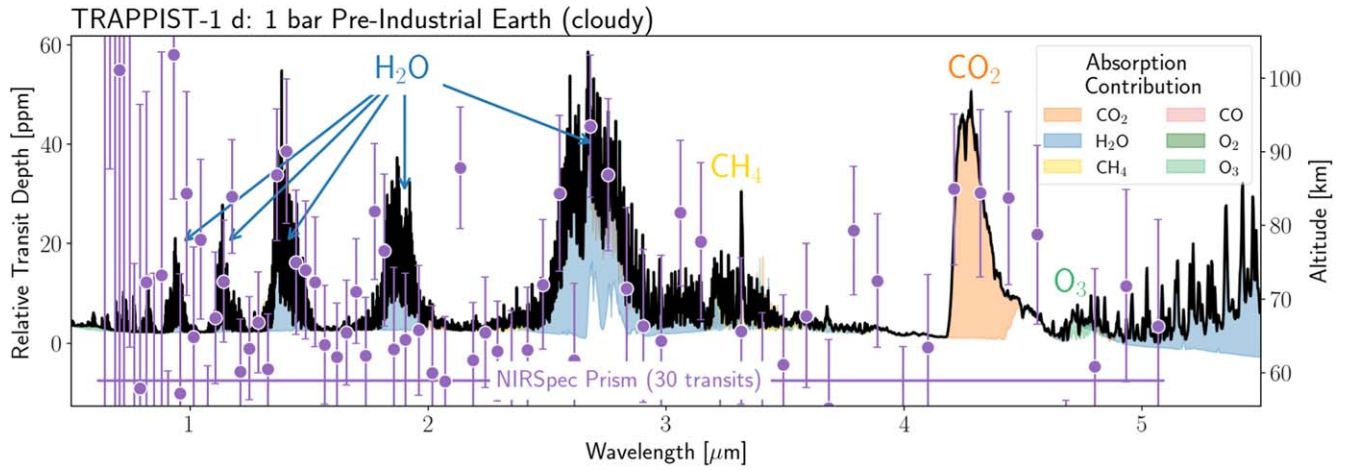
Figure 14. Theoretical transmission spectrum (at 1 cm^{-1} resolution) of TRAPPIST-1 d with a cloudy modern-Earth-like atmosphere. The shaded color regions show the contribution of the dominant absorbing molecules to the spectrum. Simulated data points and error bars are shown for 30 transits (binned to a resolving power of $\mathcal{R} = 20$) with NIRSpec Prism (NGROUP = 6), which is sufficient for $\langle S/N \rangle \approx 5$ on H_2O and $\langle S/N \rangle \approx 3$ on CO_2. For reference, the NIRSpec spectrograph with the double-pass low-resolution prism has a spectral resolving power R ($\lambda/\Delta\lambda$) of 30–300, and that with the high-resolution G140H grating has an R of 1300–2300 (Jakobsen et al. 2022).
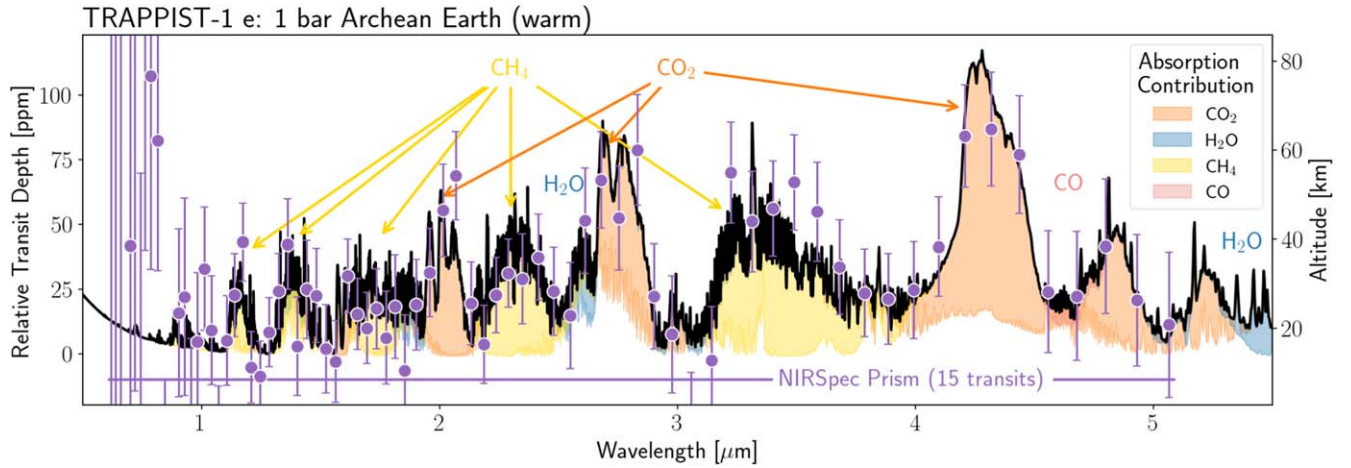

Figure 15. Simulated data and transmission spectrum model (at 1 cm^{-1} resolution) of TRAPPIST-1 e assuming that it possesses a 1 bar Archean-Earth-like atmosphere with a methanogenic biosphere (warm Archean Earth case). The spectrum is shown with water clouds in the atmosphere, with error bars calculated for 15 transits observed with JWST/NIRSpec Prism (binned to a resolving power of $\mathcal{R} = 20$). The shaded color regions show the contribution of the dominant absorbing molecules to the spectrum, which notably shows large and detectable CO_2 and CH_4 features and small and undetectable H_2O and CO features.

determine the detectability of haze absorption features is identical to that used for other molecular bands, and it calculates the number of transits needed to resolve the haze's absorption contribution to the transmission spectrum. MIRI LRS is the only instrument that covers the prominent 5.5–8 μm haze absorption band and is therefore well suited for detecting it, although at least ∼20 coadded transits would be required for weak sensitivity to it.

To illustrate some of the key results in the table, we also generated a sample of simulated JWST spectra for several inhabited environments, with noise. We present and describe these below, along with general comments about the detectability of features for our simulated planets with similar environments to the example spectra.

3.4.2. TRAPPIST-1 d

Figure 14 shows transmission spectra and simulated observations for TRAPPIST-1 d with a cloudy modern-Earth-like atmosphere. The high-altitude cloud deck that forms in this warmer, wetter atmosphere acts to preclude the detectability of the possible biosignature gases (CH_4, O_3, O_2) in less than 100 transits. However, spectral features from water vapor above the clouds are still more pronounced in this spectrum when compared with the TRAPPIST-1 e results. As a result, 10 transits with NIRSpec Prism (NGROUP = 6) are needed to weakly detect the presence of the atmosphere, where the strongest potentially detectable features would come from water vapor, rather than CO_2 or CH_4 as is the case for the other atmospheres considered here. CO_2 is also potentially detectable, although the features are weakened by the low abundance needed to avoid runaway and the truncation by the high cloud. The 30 coadded transits simulated for Figure 14 would lead to $\langle S/N \rangle \approx 5$ sensitivity to H_2O and $\langle S/N \rangle \approx 3$ sensitivity to CO_2.

3.4.3. TRAPPIST-1 e Archean Earth with Methanogens

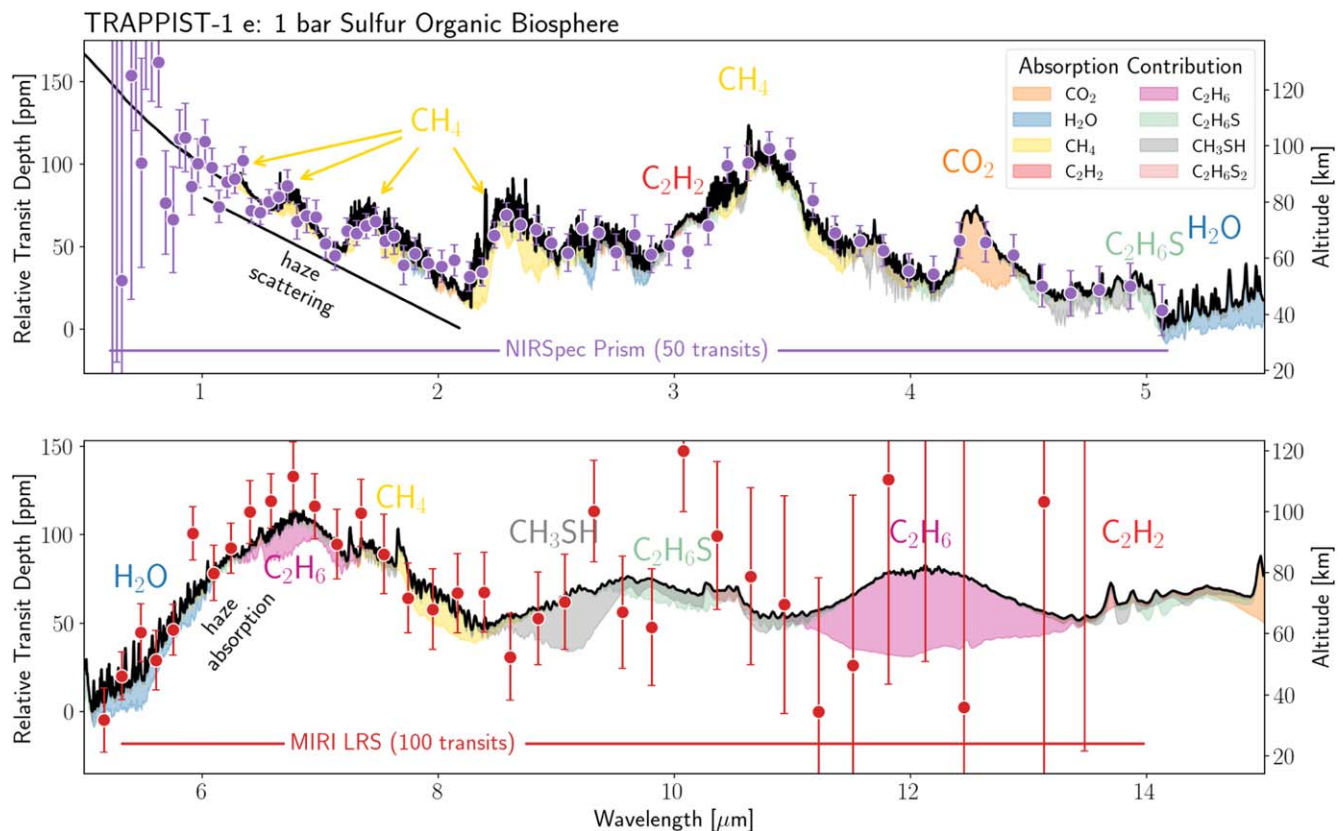Figure 15 shows the model spectrum and 15 transits of simulated JWST/NIRSpec Prism data points for the cloudy,

Figure 16. Transmission spectrum model (at $1 \, cm^{-1}$ resolution) of TRAPPIST-1 e assuming that it possesses a 1 bar sulfur organic biosphere with a thick hydrocarbon haze. The simulated data are shown with error bars corresponding to 50 transits with NIRSpec Prism (top panel) and 100 transits with MIRI LRS (bottom panel), both binned to a resolving power of $\mathcal{R} = 20$. Individual absorption features are shaded in color to indicate the molecule responsible for the absorption. Despite the presence of numerous biosignature gases in the mid-IR with strong features (e.g., DMS, C_2H_6, and CH_3SH), CO_2, CH_4, and organic haze are the most detectable potential biosignatures for these environments.

but nonhazy, warm Archean-Earth-like (>2.5 Ga) TRAPPIST-1 e atmosphere, which has 5% CO_2 and a strong surface flux of CH_4 from methanogens. Prominent features from CO_2 and CH_4 are readily detectable for S/N = 3 in two to three transits, or S/N = 5–6 in 6–12 transits, with the partially saturated NIRSpec Prism (see Table 4) and could be interpreted as a biogenic disequilibrium (Krissansen-Totton et al. 2018b). Water vapor, however, is challenging, with ∼50 transits required with either NIRSpec or MIRI. For comparison, the more challenging case of a colder, cloudy, and hazy Archean still suggests that the CO_2 and biogenic CH_4 pair may be feasible. This environment has a CO_2 abundance of only 150 ppm, which is lower than that expected for Earth's Archean, but this abundance chemically enables the presence of a high haze—which additionally truncates the absorption features from CH_4. Nonetheless, even in this doubly challenging case, 17 and 13 transits are needed for a 3σ detection of CO_2 and CH_4, respectively.

To strengthen the conclusion that the CO_2/CH_4 disequilibrium pair is due to life, abundances and false-positive discriminators could be sought. If CH_4 abundances can be retrieved from the spectrum, then calculations of the corresponding surface fluxes needed to maintain those abundances against photochemical destruction would help assess whether a biogenic origin for the CH_4 was more likely. The significant nondetection of CO at $4.6 \, \mu m$, even for 100 transits, also implies that the false-positive scenario of the prebiotic Earth with vigorous volcanic outgassing from a reduced mantle (Krissansen-Totton et al. 2016) is unlikely. Conversely,

confirming the false-positive scenario may be relatively straightforward and require fewer transits. For the prebiotic Earth case, the 1.9% CO_2 is of comparable detectability, requiring three versus two transits for a 3σ detection. However, the CH_4 is significantly weaker in the false-positive case, despite the 200× volcanic flux, requiring 40 transits compared with three transits for the methanogenic Archean. Additionally, the CO features at 2.3 and especially $4.6 \, \mu m$ (see Figure 13) are far more detectable in the false-positive case, requiring only seven transits instead of over 100. However, the much weaker H_2O features may require a significant observational investment to detect.

3.4.4. Archean Earth with a Sulfur Biosphere

Figure 16 shows spectra and simulated JWST data for an Archean-Earth-like atmosphere with both methanogenesis and a strong sulfur-generating biosphere for 50 transits with NIRSpec Prism (top) and 100 transits with MIRI LRS (bottom). This spectrum is generated using the cloudy and hazy Archean Sorg ×30 environment, where the sulfur organic fluxes from the biosphere are 30× Earth's modern-day value and the atmosphere contains 524 ppm of CO_2 and an organic haze. This scenario enhances the abundances of sulfur organic molecules because the haze shields them from photochemical destruction. Domagal-Goldman et al. (2011) postulated that a sulfur biosphere might produce biosignatures of C_2H_6 (ethane) and DMS. However, although both the latter two molecules produce relatively strong features in the mid-infrared in our
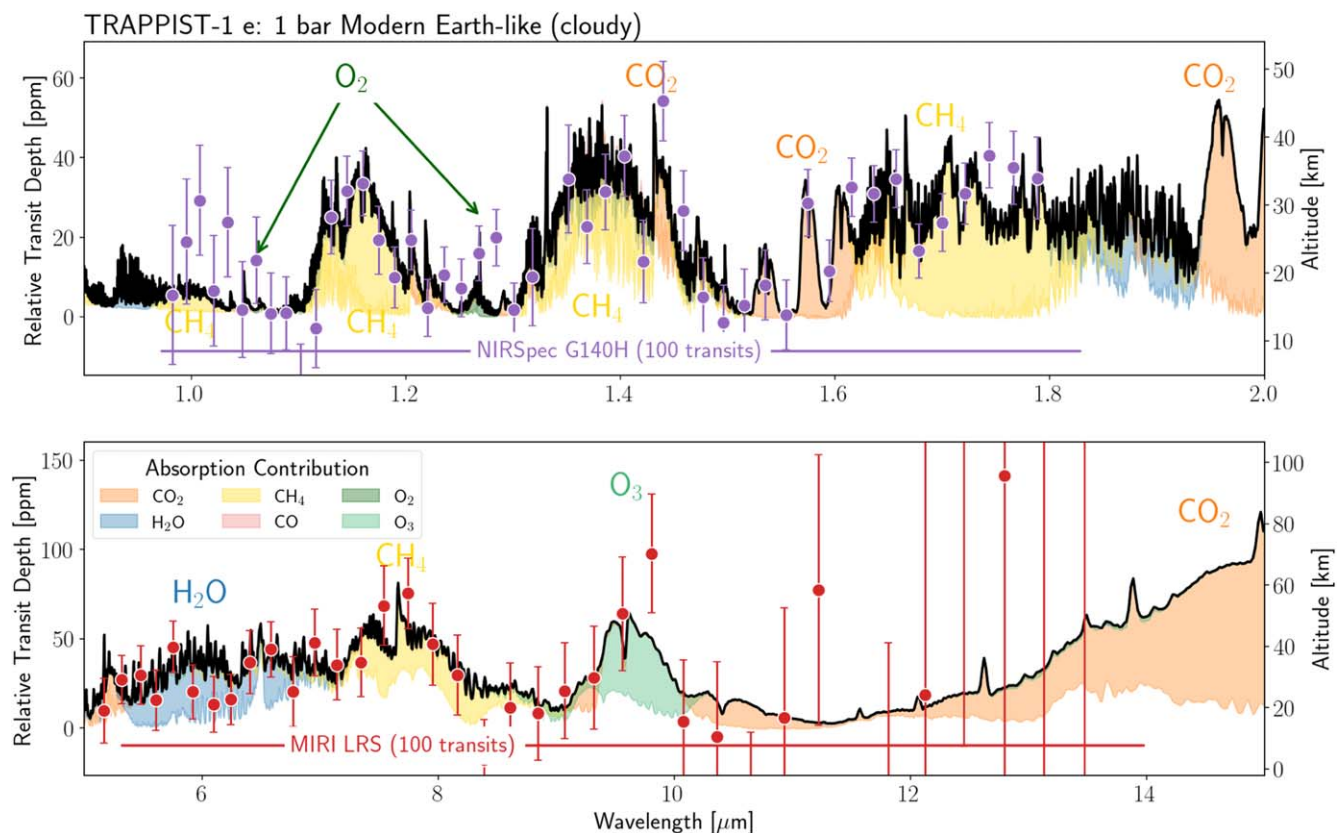
Figure 17. Theoretical transmission spectra (at 1 cm^{-1} resolution) of TRAPPIST-1 e with a cloudy modern-Earth-like atmosphere. In the top panel, error bars are shown for 100 transits with NIRSpec G140 (binned to a resolving power of $\mathcal{R} = 40$), which is insufficient for O_2 detection for TRAPPIST-1 e. In the bottom panel, error bars are shown for 100 transits with MIRI LRS (binned to a resolving power of $\mathcal{R} = 20$), which is also insufficient for the detection of O_3 at 9.6 μm. An S/N of 3 for O_3 would require ~260 transits.

simulated transmission spectra, MIRI lacks the sensitivity to detect them in less than 100 transits. Instead, features from DMS also exist and are more detectable in the near-infrared with NIRSpec PRISM, although a challenging 94 transits would still be needed. However, another product of the sulfagenic biosphere, methyl mercaptan (CH_3SH), appears to be the most promising sulfagenic molecular biosignature in the JWST wavelength range, producing features in our spectrum that could potentially be detected in 50 transits with NIRSpec. As environmental context, H_2O is also potentially detectable with 35–62 transits.

Hydrocarbon haze features have also been proposed as a potential biosignature in atmospheres where biogenic CH_4 or methyl radicals from the photolysis of more complex biogenic molecules such as DMS (C_2H_6S) provide the right conditions for haze formation when it would otherwise not form without the biosphere (Arney et al. 2018). In the Archean sulfagenic, hazy example shown in Figure 16 our simulations suggest that both MIRI and NIRSpec could detect the biogenic CH_4 absorption in as few as seven transits and the hydrocarbon haze slope in only four transits. Positive confirmation that the haze is likely organic would require 28 transits with MIRI. However, abundances and surface fluxes for CH_4 derived from observations and models could also help interpret the haze features. It is also worth noting that the combination of hazes and organics produces a pseudocontinuum of enhanced absorption from 6 to 15 μm that may be a potential target using MIRI filter bands, although we do not simulate those here.

Expanding on the low-CO_2, hazy example given above by taking the Archean sulfur biosphere examples as a whole, the most detectable biosignature in these environments is still the CH_4/CO_2 disequilibrium pair from the methanogens. This biosignature is potentially detectable in all five sulfagenic scenarios and is the only molecular biosignature detectable for the $10\times$ Sorg case. This pair is often more challenging to detect than in the haze-free Archean case, however, requiring 1–18 transits for a 3σ detection of CH_4 and 2–30 transits for a 3σ detection of CO_2. When present, the next most accessible biosignature is the haze scattering slope shortward of 2 μm, which requires two to five transits to detect, but 21–28 transits for detection of the more diagnostic haze absorption between 6 and 8 μm. For the $30\times$ sulfur species and $30\times$ sulfur organics species hazy cases, DMS potentially becomes detectable, although extremely challenging at 94–96 transits, as does CH_3SH at 50–99 transits.

3.4.5. Earth-like with Photosynthetic Biosphere

Figure 17 shows spectra and simulated JWST data for a cloudy modern preindustrial Earth-like TRAPPIST-1 e that has a biosphere that is dominated by oxygenic photosynthesis, but which also includes a methanogenic flux. Spectra and simulated JWST/NIRSpec data are shown in the top panel, and JWST/MIRI data are shown in the bottom panel.

These simulations show that biogenic O_2 and its photochemical proxy, O_3, are likely to be extremely challenging to detect with JWST, especially in the presence of clouds. The O_2
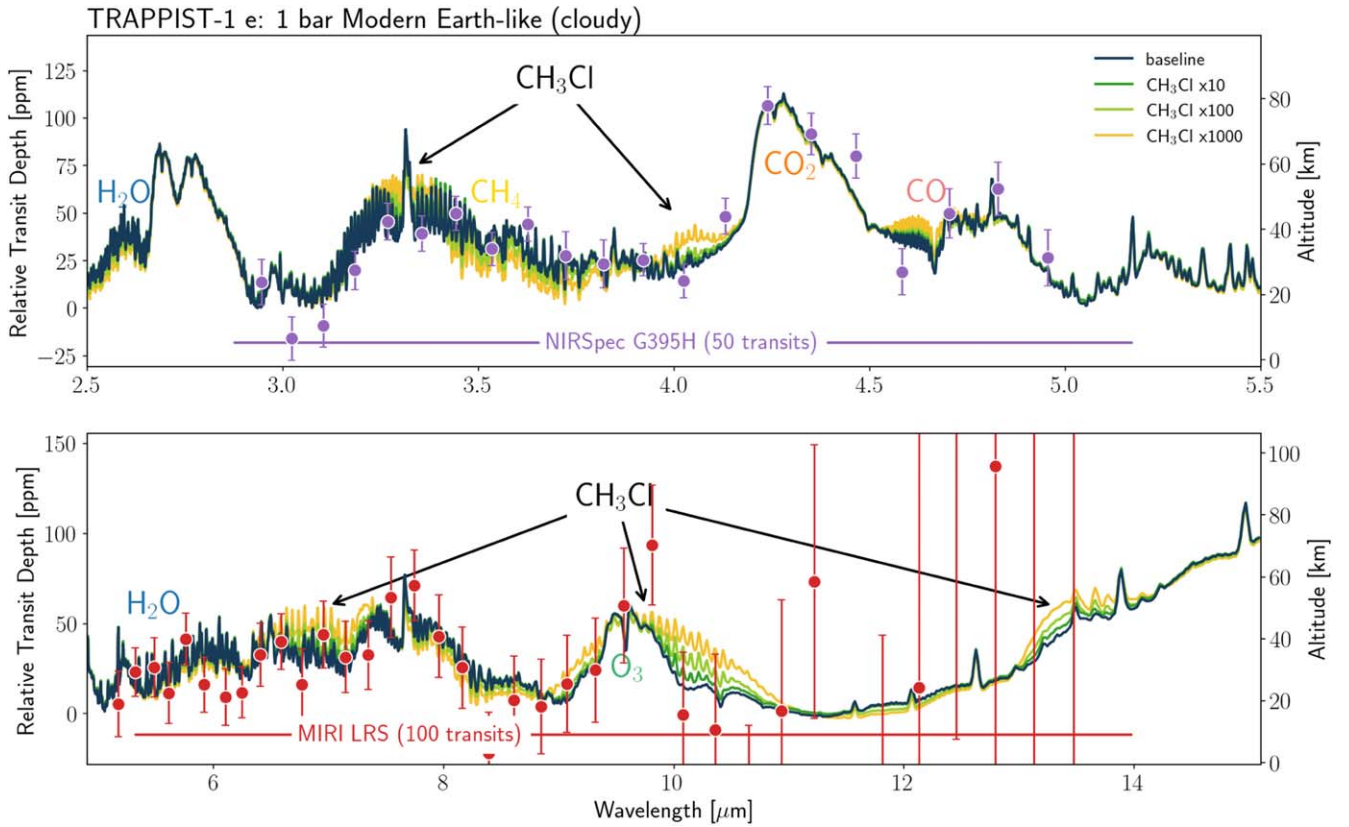
Figure 18. Theoretical transmission spectra (at 1 cm^{-1} resolution) of TRAPPIST-1 e with a modern-Earth-like atmosphere with increasing levels of CH$_3$Cl enhancement. Error bars are shown for 50 transits with NIRSpec G395, which is sufficient for $\langle S/N \rangle \approx 4.6$ on CH$_3$Cl at 1000 × enhancement, and 100 transits with MIRI LRS, which is insufficient for the detection of CH$_3$Cl despite the presence of a large absorption feature between 9 and 11 μm. Both simulated observations are binned to a resolving power of $\mathcal{R} = 20$.

features at 1.06 and 1.27 μm are both weak and relatively narrow, and in a cloudy atmosphere 100 transits with NIRSpec result in an S/N of only 1 for these features (900 transits for S/N = 3). If the higher spectral resolution, narrower wavelength range G140H is used for the 1.27 μm O$_2$ band alone, a 3σ detection may be possible for the clear modern-Earth-like case by acquiring just over 100 transits. The broad O$_2$–O$_2$ collisionally induced feature at 6 μm proposed as an alternative means to detect O$_2$ (Fauchez et al. 2020) is also not detectable for this habitable planet case, as it is swamped by strong absorption from water vapor. Consequently, more than 100 transits would be required for a 3σ detection of O$_2$ molecular absorption or collision-induced absorption (CIA). The 9.6 μm O$_3$ feature is broader and more prominent than the narrow O$_2$ molecular absorption lines, but given the expected noise of MIRI LRS observations, it is only detectable at $\langle S/N \rangle \approx 2$ in roughly 100 transits.

However, even though the indicators of abundant O$_2$ and the possible presence of an oxygenic-photosynthetic biosphere are extremely challenging, the terrestrial CO$_2$ and methanogenic CH$_4$ remain relatively easy to detect, with as little as two to three transits needed for an S/N = 3 detection of these two molecules, and 10 transits needed for a more robust detection at S/N of 5–6. Water is potentially detectable in 41 transits with NIRSpec and a comparable 39 transits with MIRI LRS.

Looking at the preindustrial modern Earth simulations as a whole (see Table 4), we can assess the effects of clouds and photochemistry on detectability. We see that the clouds have no impact on the detectability of the relatively evenly mixed

atmospheric gases CO$_2$ and CH$_4$, which require two transits for a 3σ detection in both clear and cloudy cases, but they nearly double the time required to detect water vapor, from 20 transits for the clear-sky case to 37 transits for the cloudy case. If we also compare the detectability of CH$_4$ and O$_3$ for the climatically and photochemically self-consistent preindustrial TRAPPIST-1 modern Earth with those for a true Earth atmosphere but a TRAPPIST-1-sized planet and orbit, we can see the host star's critical impact on photochemistry and detectability. For example, the number of transits required to detect the CH$_4$ abundance for the true Earth would increase significantly to 76 for the cloudy non-self-consistent case, compared to the two transits required for detection of CH$_4$ for the self-consistent TRAPPIST-1 preindustrial Earth. Conversely, O$_3$ would go from being undetectable in well over 100 transits in the self-consistent case, primarily due to inefficient O$_3$ formation under the TRAPPIST-1 M8V stellar spectrum, to being detectable in 64 transits for the true Earth case.

Figure 18 shows transmission spectra and simulated observations for an Earth-like TRAPPIST-1 e with an oxygenic-photosynthetic biosphere and CH$_3$Cl surface fluxes (nominally from vegetation) enhanced by factors of 10–1000 over Earth's. Spectra and JWST simulated data for 50 transits focusing on NIRSpec's 2.5–5 μm range are shown in the top panel, and 100 transits in MIRI's 5–15 μm range are shown in the bottom panel. We find that a 1000 × enhancement in the surface flux of CH$_3$Cl is detectable at the 3σ level with the NIRSpec in 21–23 transits using NIRSpec G395H or NIRSpec Prism (see Table 4). However, the perhaps more realistic

10–100× enhancement cases are either not detectable in under 100 transits for the 10× enhancement or challenging at 97 transits for the 100× enhancement case. We also note that despite the strong and broad CH_3Cl feature between 9 and 11 μm, it is less detectable than the weaker features in the NIRSpec wavelength range owing to both JWST/NIRSpec's better sensitivity at shorter wavelengths and the strong overlap of O_3 and CH_3Cl near 9.6 μm.

4. Discussion

With this work we have used self-consistent 1D coupled climate–photochemical and radiative transfer models to simulate TRAPPIST-1 d and e transmission spectra and explored the detectability of a suite of biosignatures appropriate for modern and early Earth-like atmospheres and biospheres. We confirm previous calculations that indicate that detecting the impact of oxygenic photosynthesis, via the presence of O_2 and O_3, will be extremely challenging. CH_3Cl, a possible alternative biosignature for oxygenic photosynthesis, is also likely challenging to detect except at implausibly large surface fluxes. However, we find that the CH_4/CO_2 disequilibrium pair, previously identified as characteristic of Archean methanogenic biospheres, may be detectable with JWST NIRSpec transmission observations even in the presence of clouds and photochemical hazes. In addition, we find that this gas pair is in fact the most detectable biosignature in all environment/metabolism combinations, including for the methanogenic/photosynthetic biosphere on modern-day Earth. We also find that our modeled high molecular weight inhabited atmospheres are all potentially detectable at 3σ within two to nine transits, even when taking into account the presence of clouds and hazes. And our models indicate that organic hazes counterintuitively enhance the detectability of organic molecules in transmission by shielding them from photolysis in the UV and being relatively transparent at the longer wavelengths where these molecules absorb. Finally, we note that biosignature gases can have a profound effect not only on planetary atmospheric composition but on planetary climate and habitability as well.

4.1. The By-products of Oxygenic Photosynthesis Are Likely Not Detectable with JWST

While oxygenic photosynthesis is the dominant metabolism on modern Earth and has produced the largest modifications to our atmosphere, we have used photochemically self-consistent, clear and cloudy simulations to confirm the results of previous work in finding that the key signatures of this metabolism, including abundant O_2 and O_3, are highly unlikely to be detectable in JWST data. While our simulations show that clouds can suppress O_2 and O_3 signals below 1.6 μm, even our clear-sky simulations show that biogenic levels of O_2, and the attendant photochemically generated O_3, are not detectable using the full NIRSpec or MIRI wavelength range in less than 100 transits. This is due in part to the narrowness and weakness of the O_2 bands, but also to JWST's relative lack of sensitivity at shorter wavelengths. Sensitivity to the 0.76 μm O_2 absorption band in particular is also compromised by the lack of backlighting in transit due to the late M-dwarf stellar spectrum, which decreases rapidly in brightness below 1 μm. Because the molecular O_2 bands are relatively narrow, the higher-resolution G140H mode is better suited for their

detection, but even so, in the fully clear-sky case, it requires 100 transits for an S/N $\sim$ 3 detection. For the cloudy TRAPPIST-1 e simulations, the resultant truncation of the atmospheric path length results in 100 transits with G140H for an S/N $\sim$ 1 detection, or an implausible 900 transits for an S/N $\sim$ 3 detection. While the 6 μm O_2–O_2 band has been suggested as an alternative means of detecting O_2 (Fauchez et al. 2020), its signal was relatively weak compared with the much stronger 6.3 μm H_2O band on these habitable planets, and 100 transits with MIRI were not sensitive enough to detect it. In the case of O_3, which is generated via the photolysis of O_2 and can serve as a chemical proxy for it, the strongest spectral features are at 9.6 μm in the mid-infrared, and 100 transits with MIRI can only reach an S/N of 2. This is due in part to MIRI's lack of sensitivity to the signals generated by high mean molecular weight atmospheres, but also to the fact that the integrated column abundance of O_3 is significantly lower than for Earth, due to the photochemical migration of the ozone bulge to higher altitudes for these simulated M-dwarf planets, as described in Section 3.1.

For TRAPPIST-1 d, for which we were able to obtain a borderline stable habitable environment for a modern-Earth-like atmospheric composition (see also Section 4.5), we also found that the O_2/O_3 features required more than 100 transits for detection. This relative lack of detectability of biosignatures is despite the potential advantages to detectability conferred by TRAPPIST-1 d's high atmospheric temperature and scale height. Instead, TRAPPIST-1 d's warm temperature profile leads to a water-rich atmosphere that suppresses detection of O_2, CH_4, and O_3 via a combination of chemistry and cloud formation. The abundant water vapor leads to production of the OH radical (see Wunderlich et al. 2019), which reduces the photochemical accumulation of CH_4 to 4.5 ppm and results in a column depth of O_3 that is an order of magnitude less than those of the TRAPPIST-1 e planets. The formation of a cloud deck with a cloud top near 75 km in this warmer, wetter atmosphere then truncates the path length at altitudes above this level, narrowing the molecular features of all the biosignatures, including O_2, and reducing the amplitude of their features.

Our results are consistent with previous work that shows that O_2 and O_3 will be extremely challenging to detect with JWST for planets in the TRAPPIST-1 system. These include the results of Wunderlich et al. (2019), who found that 170 transits would likely be needed for a 3σ O_3 detection for a habitable Earth-like planet close to TRAPPIST-1 e's insolation; Gialluca et al. (2021), who require over 360 transits for an S/N = 3 for O_3 detection for a habitable TRAPPIST-1 e; Wunderlich et al. (2020), who predict that 45 transits are needed to detect even an enhanced O_3 abundance in a clear-sky atmosphere; and Lustig-Yaeger et al. (2019), who required over 100 transits for a 3σ detection of O_3 for a TRAPPIST-1 e habitable aqua planet and well over 100 transits for O_2 detection. Moreover, for 85 transits of a clear-sky Earth using NIRSpec Prism sub512s, Pidhorodetska et al. (2020) predicted an S/N of 1.6 for O_2, and we are in very good agreement with this result, finding 85 transits for an S/N of 1.6 for our clear-sky Earth observed with NIRSpec PRISM. Results for the more realistic cloudy-sky cases indicate that detectability would be even more challenging, with our results predicting an S/N of 0.4 for O_2 with NIRSPEC prism in 100 transits and an increase to an S/N of 1 for 100 transits with the higher spectral resolution provided by NIRSpec G140H.

We also modeled O_2–O_2 CIA as a potential marker of a photosynthetic biosphere for our clear and cloudy atmospheres, including the relatively strong feature at 6 μm (Fauchez et al. 2019), but due to the confounding effects of water vapor in a habitable atmosphere, this feature did not attain an S/N of 3 in 100 transits or less with MIRI. This result is also supported by Pidhorodetska et al. (2020), where 85 transits with MIRI are predicted to attain an S/N of only 1.7 for this feature.

We also note that Gialluca et al. (2021) obtained more optimistic results for O_2 detectability, with 40 transits for S/N = 5 O_2 detection. This result was for a generic TRAPPIST-1 planet that is hotter, with a larger scale height and no clouds, and for O_2 spectral features of comparable strength to the surrounding H_2O and CH_4 features, i.e., considerably stronger than those seen in our or the Pidhorodetska et al. (2020) synthetic spectra. This anomalous spectral result is currently being reevaluated and may be due to an error in the treatment of O_2–O_2 CIA (Gialluca et al., private communication). If that is the case, then the true detectability will require significantly more transits than indicated.

The overall agreement between modeling efforts from three separate research groups, using both 1D and 3D models of photochemically self-consistent atmospheres, strongly suggests that O_2 and O_3 features for an Earth-like oxygenic-photosynthetic biosphere will be challenging, if not impossible, to detect with JWST. This conclusion emphasizes the important role of the next generation of ground-based telescopes and future space-based direct imaging missions with the wavelength range and sensitivity to search for signs of biogenic O_2 and its O_3 photochemical proxy in habitable exoplanet atmospheres (e.g., Lovis et al. 2017; Feng et al. 2018; Arney 2019; Lopez-Morales et al. 2019; Bixel & Apai 2021; Currie et al. 2023; Hardegree-Ullman et al. 2023).

Our calculations for the modern-Earth-like planets also emphasized the importance of self-consistent photochemistry and climate in assessing the probability for detection of biosignatures—due to photochemistry's effect on gas abundance and the climate's impact on vertical temperature structure, scale height, atmospheric water vapor, and cloud formation. Photochemistry strongly drives the TRAPPIST-1 e and d atmospheric trace gas abundances, especially for O_3 and CH_4. If the formation and destruction of O_3 are ignored, and instead Earth's existing O_3 profile and abundance are used, our detectability calculations suggest that TRAPPIST-1 e with Earth-like O_3 could be detected in 64 transits. This is comparable to the 30 transits calculated for a TRAPPIST-1 d Earth twin by Barstow & Irwin (2016), but still conservative when compared with the 15–18 transits found by Tremblay et al. (2020) for O_3 detection on an Earth-twin TRAPPIST-1 e. However, the high abundance of O_3 exhibited by an Earth-twin atmosphere is at odds with the significantly lower O_3 column depths seen in our TRAPPIST-1 d and e simulations, where the climate and chemistry is self-consistent with the incident stellar radiation. In the self-consistent cases, even with a 21% O_2 abundance, the lower O_3 abundances increase the number of transits required for O_3 detection to over 100 transits for both TRAPPIST-1 d and e. Conversely, by ignoring the photochemical buildup of CH_4 on planets orbiting M dwarfs, we find that Earth's modern-day 1.8 ppm CH_4 abundance would require 76 transits for a 3σ detection, which is comparable to the Tremblay et al. (2020) analysis of 62 transits for a 3.6σ detection. However, for TRAPPIST-1 e's self-consistent CH_4

abundance, despite having a lower surface flux of CH_4 than the Earth twin, photochemistry enhances the abundance by 2.5 orders of magnitude so that only two transits are needed for S/N = 3 detection.

We also note that we were not able to build up significant amounts of CO or abiotic O_2 on our Archean-like planets under the TRAPPIST-1 SED used here. We used a relatively high CO deposition rate of 0.03 cm s^{-1} (Hauglustaine et al. 1994), which is applicable primarily to continents, and which would have favored abiotic O_2 production, and yet we see only negligible amounts of O_2 in the stratosphere in this case. However, when combined with lighting production of NO, this rapid removal of CO keeps the abundance of CO low in our atmospheres. Previous work has shown that smaller deposition rates and active surface fluxes may build up higher amounts of CO, even on a habitable Archean-type planet (Schwieterman et al. 2019). Indeed, when we decrease our CO deposition rate to 10^{-8}—the calculated maximum CO deposition rate in the absence of biology (Kharecha et al. 2005; Harman et al. 2015) —we do see increases in CO abundance in the lower atmosphere, but a factor of 2 decrease in O_2, which remains present in the upper atmosphere only. This lack of abiotic O_2 production is consistent with that seen in the Harman et al. (2018) models that include lightning-driven reactions, but it appears to be inconsistent with other results (Hu et al. 2020) that model TRAPPIST-1 e and assume a similarly low deposition rate for CO and lightning-driven reactions but build up 0.02 bars or more of O_2 for CO_2 abundances of 5%, as we used here.

4.2. CH_3Cl Is Challenging as an Alternative Biosignature for Oxygenic Photosynthesis

We explored the possibility that CH_3Cl could serve as a more JWST-accessible proxy for a terrestrial planet with a photosynthetic biosphere with large amounts of vegetation, given that biogenic O_2 or O_3 detection is likely extremely challenging and that their nondetection also negates the use of the O_2/CH_4 and O_3/CH_4 biosignature disequilibrium pairs. However, we find that the flux rates needed for detection are still implausibly high. Our simulations show that detecting CH_3Cl is challenging in both the NIRSpec and MIRI wavelength ranges and that more than 100 transits are needed for both instruments for a planet with 10 times Earth's current averaged global flux (or twice the flux from a tropical-vegetation-dominated biosphere). Features of CH_3Cl become potentially detectable in our simulations of TRAPPIST-1 e with 97 transits with NIRSpec for S/N = 3 for 100 times Earth's current global flux of CH_3Cl and for 21–23 transits with NIRSpec for S/N = 3 with NIRSpec at 1000 times Earth's current global flux. In all cases, including the 100 and 1000 times flux rates, MIRI had less sensitivity than NIRSpec to CH_3Cl features and for detection required 89 transits for CH_3Cl at $1000\times$ and 400 transits at $100\times$. This result is consistent with Leung et al. (2022), who calculated MIRI detectability and found that over 100 transits were needed with MIRI for a modern-Earth-like TRAPPIST-1 e with 100 times Earth's CH_3Cl flux.

We therefore find that it is unlikely that CH_3Cl would make a good proxy for a vegetation photosynthetic biosphere for JWST observations, although it may be plausible for some microbially dominated environments (Leung et al. 2022). Earth's tropical plants produce CH_3Cl at 6 times the global flux

per unit area, so a tropical-forest-covered planet would have only 6 times Earth's current global flux, unless a significant increase in the production efficiency of CH_3Cl by vegetation is assumed. However, that may not be implausible, as some of Earth's biomes are known to be more efficient at producing CH_3Cl per unit area (Leung et al. 2022). In particular, localized areas in salt marshes produce from 50 times (Blei et al. 2010) to up to 3000 times (Rhew et al. 2000) Earth's average CH_3Cl flux rate, as organisms in those environments detoxify halides by methylating and volatilizing them (Rhew et al. 2000; Blei et al. 2010; Leung et al. 2022). Leung et al. (2022) therefore speculated that an inhabited planet with a higher concentration of dissolved halides may have a biosphere that produces a higher CH_3Cl signal, which could approach the 100 or (perhaps less likely) 1000 times flux value modeled here. However, with 97 transits needed for an $S/N = 3$ detection at the 100 times flux value, detecting such a biosphere would still be extremely challenging.

As an aside, we also found that high atmospheric CH_3Cl levels, perhaps from a more halide-rich environment, have the chemical consequence of enhancing the destruction of other biosignatures, most notably O_3 and CH_4 (see Figure 7). On Earth, CH_3Cl is known as the largest natural source of ozone-depleting Cl compounds (Butler 2000), and our simulations also showed depletion of atmospheric O_3 for our TRAPPIST-1 planets, by up to an order of magnitude, although the strength of the ozone spectral features was less heavily affected.

4.3. Biosignatures from a Sulfur Biosphere Will Also Be Challenging

By simulating the detectability of biosignature species from a sulfur biosphere in the presence of hazes, we found that hazes can shield many biosignature species from destruction at shorter wavelengths, but without significantly reducing their detectability at longer wavelengths. Our TRAPPIST-1 (M8V) haze-free warm Archean shows similar abundances and distributions for ethane when compared with the Domagal-Goldman et al. (2011) AD Leo (M3.5V) haze-free sulfur organics biosphere—with an abundance of ∼1 ppm in the lower atmosphere, decreasing owing to photolysis above 40 km altitude. In contrast, our other Archean sulfur organics cases were simulated with self-consistent haze production and higher surface fluxes of organics, leading to formation of a thick haze. The haze provided a UV shield that allowed buildup of biosignature gases to levels 2–3 orders of magnitude higher (Figure 6) than those seen in our haze-free warm Archean case (Figure 5) and the haze-free sulfur organic cases of Domagal-Goldman et al. (2011). Moreover, the majority of the haze absorption is in the UV and visible, whereas the spectral absorption from sulfur organic and hydrocarbon biosignature gases is seen mostly in the near- and mid-infrared, where the haze absorption was less pronounced. Consequently, the haze was able to shield biosignature gases from photolysis in the UV, preserving higher atmospheric abundances at the higher altitudes probed by transit, but it did not significantly lessen the detectability of the biosignature spectral features at longer wavelengths.

Our simulations show that sulfur biosignature gas detectability is still extremely challenging, despite what should have been an optimal detection scenario. High surface fluxes, photochemical shielding by hazes, and our use of room-temperature cross-section files all should have worked to

enhance the predicted atmospheric abundances and strength of transmission spectral features. However, the majority of these features are at wavelengths only accessible to the JWST/MIRI instrument, and our simulations predict that MIRI lacks the sensitivity to detect sulfur biosignature gases, even at up to 30 times the current Earth's sulfur organic fluxes. Instead, NIRSpec may have the required sensitivity to detect DMS and methyl mercaptan (CH_3SH), at the 30 times flux rate, with $S/N = 3$ detections requiring 94–96 transits and 50–99 transits, respectively. However, because line lists for these molecules are unavailable, these detectability estimates, including both the nondetections and the marginal detections, were made using available room-temperature cross-section files, which lack the pressure and temperature dependence of measured line lists. Our absorption features are therefore likely overestimated in strength, as transmission is most sensitive to the cooler upper troposphere and stratosphere, where the temperatures and pressures are significantly lower than room temperature. This ensures that our nondetections are robust, because even with the enhanced absorption afforded by the cross-section files the molecules were still not detectable. However, it also casts doubt on the DMS and CH_3SH detectability estimates, as the features from these molecules are likely overestimated. We performed initial tests that suggest that the difference in modeled band strength using absorption cross sections versus line list data is case specific, and larger discrepancies in absorption strength are likely with larger gas abundance.

Our results therefore suggest that for JWST the most robustly detectable biosignature for the sulfur biosphere is a biologically mediated haze, although progressively larger amounts of observing time are needed to detect, identify, and interpret a biogenic haze. Organic hazes typically form in Archean-type atmospheres when the ratio of CH_4 to CO_2 is above 0.1 (Trainer et al. 2006; Arney et al. 2018). Arney et al. (2018) have argued that such a haze may be considered a biosignature if organic sulfur compounds contributed methyl groups and other hydrocarbons to enhance the haze formation over that expected from the atmospheric CH_4/CO_2 ratio alone. In our simulations, an organic haze produces a pronounced slope in the 0.5–1.5 μm region, which may require only two to five transits to detect. However, the slope could conceivably be formed by another type of aerosol, and positive identification of an organic haze would require detection of the haze absorption feature between 5.5 and 8 μm, in 18–28 transits. To then more robustly discriminate between an abiotic and biological origin of an organic haze, the CH_4/CO_2 ratio and the UV spectrum of the host star are needed, to determine the likelihood that the haze could have formed with or without an additional (biological) source of organic compounds. Our simulations showed that for Archean-like environments with sulfur biospheres, the CH_4/CO_2 pair needed to assess haze formation potential and to identify the presence of a methanogenic biosphere is still more detectable than the sulfur biosignatures themselves. However, in the presence of a haze, these two gases are more difficult to detect, with as many as 30 transits needed for CO_2 and 18 transits for CH_4. For CH_4, detectability is straightforwardly reduced by the haze increasing the short-wavelength near-infrared continuum, where many of the CH_4 absorption bands occur. However, for CO_2 this loss of detectability compared to the nonhazy cases is due in part to the environmental parameters required for the hazy planet to remain habitable (and so able to support a biosphere), with

lower CO_2 needed both to allow the hydrocarbon haze to form and to offset the higher greenhouse warming obtained with the sulfur biosignature gases.

4.4. The Methanogenic Biosphere Is Likely the Most Detectable with JWST

For the TRAPPIST-1 Archean-like environments with a methanogenic biosphere, our models predict that the CO_2/CH_4 biosignature pair would likely be the most detectable biosignature considered in this study. This work supports the general conclusion that this biosignature is potentially detectable and quantifiable with JWST spectroscopic retrieval in as few as 10 transits, as described in Krissansen-Totton et al. (2018a) and Mikal-Evans (2022), and adds information on the detectability of this biosignature pair for self-consistent chemistry and the presence of more realistic clouds and hazes. In our simulation for the haze-free but cloudy Archean case, as little as two to three transits are needed to achieve an $S/N = 3$ detection (6–12 transits for an $S/N = 5$ detection) for both CH_4 and CO_2. For other Archean environments with methanogenesis, including those with a sulfur biosphere, the number of transits needed for an $S/N = 3$ detection of CH_4 ranges from 1 for the $30\times$ sulfur biosignature nonhazy case to 18 for the hazy $10\times$ sulfur biosignature case. CO_2 detectability is dependent on the assumed atmospheric concentration of this gas and the presence or absence of a haze. For the low CO_2 concentration (150–524 ppm) hazy planets, the number of transits needed for an $S/N = 3$ detection ranges from 17 to 30 transits, which drops to two to three transits for the inhabited Archean environments with 5% CO_2 that are cloudy but haze free. Even considering the more difficult hazy case, these values suggest that CO_2 and CH_4 can be extremely accessible when compared to the 76 transits needed for methane detection for the non-self-consistent true Earth photochemistry on TRAPPIST-1 e and the over 100 transits required to detect abiogenic (geological) methane fluxes simulated for a TRAPPIST-1 e aqua planet in Lustig-Yaeger et al. (2019). This detectability is due in part to TRAPPIST-1's stellar spectrum, which allows the buildup of CH_4 in the atmosphere to abundances that are more than two orders of magnitude higher than the true Earth's (see Figure 7).

Our comprehensive study comparing different biosignatures in their likely environmental context has additionally shown a perhaps surprising result—that the methanogen-revealing CO_2/CH_4 biosignature pair was the most JWST-detectable biosignature for each of the simulated biospheres throughout Earth's history, up to and including the modern eon where methanogenesis and oxygenic photosynthesis coexist. Even though Earth's photosynthetic biosphere outproduces the methanogenic one by three orders of magnitude, JWST is relatively insensitive to O_2 and O_3, dramatically reducing their detectability. In addition, the extended photochemical lifetime and buildup of CH_4 on planets orbiting M dwarfs and the increased CO_2 needed to maintain a habitable surface temperature for TRAPPIST-1 e in its relatively remote position in the HZ mean that CH_4 and CO_2 are likely considerably more detectable than the by-products of an oxygenic biosphere.

The higher detectability of CH_4 in the spectrum of an Earth-like planet when compared to O_2 or O_3 is a promising discovery, because methanogenesis is an ancient metabolism that may persist throughout a significant fraction of a planet's lifetime, further increasing its probability of detection. On our own planet, methanogenesis may have originated even earlier

than 3.5 Gya (Wolfe & Fournier 2018) and has likely persisted throughout our history to the present day, and potentially at rate of productivity that is within a factor of 3 (Kharecha et al. 2005). This longevity provides a key biosignature advantage over oxygenic photosynthesis, whose impact on Earth's planetary environment is relatively recent, with support for the rise of oxygen spanning 2.3 to as recently as 0.8 billion years ago (Lyons et al. 2014; Planavsky et al. 2014a), although M dwarfs are extremely long-lived (Baraffe et al. 2015), and many nearby examples are likely older than Earth. Even though the CO_2/CH_4 pair would reveal the inhabited nature of Earth—and for observations taken at many points in Earth's evolution—because these gases are relatively easy to detect in both the Archean (more reducing) and modern (oxidizing) atmospheres, the presence of a coexisting oxygenic or sulfagenic biosphere, or even a strongly oxidizing atmosphere, would not necessarily be easily inferred.

We also found that the CH_4 signal over large spans of geological time not only remains relatively detectable in our simulations but also remains relatively constant in abundance (see Figure 12) despite our assumed CH_4 surface flux being three times higher in the Archean than in the preindustrial Earth and the significant change in the redox state of the atmosphere, from reducing in the Archean to oxidizing in the modern day. This is in stark contrast to simulations of the history of our own Earth, which suggest that while CH_4 may indeed have been higher in the Archean, with values in the 100–1000 ppm range, this value would have dropped precipitously in the Proterozoic owing primarily to increases in both atmospheric O_2 and seawater sulfate (Reinhard et al. 2017) to no more than 10 ppm (Olson et al. 2016) and then down to today's 1.9 ppm (Lan et al. 2023). Consequently, CH_4 would have been far more challenging to detect in Earth's atmosphere for nearly half our history. For reference, Earth's current flux of CH_4, which is roughly what we used for our Archean models, produces an atmospheric abundance of only 42 ppm for our warm Archean model orbiting a G dwarf and so is relatively conservative as far as CH_4 buildup.

However, for the TRAPPIST-1 planets, the differences in CH_4 surface flux in the Archean-like and preindustrial Earth cases appear to be countered by the impact of TRAPPIST-1's stellar UV spectrum on the photochemical destruction processes for CH_4 in the two different kinds of atmosphere, which in turn govern CH_4's atmospheric lifetime. Relevant CH_4 destruction processes in this case are the direct photolysis of CH_4—predominantly by photons shortward of 130 nm—and the chemical destruction of CH_4 via reaction with OH and $O(^1D)$ radicals produced via photolysis of water vapor and $O(^1D)$ radicals produced from photolysis of ozone.

For the preindustrial Earth, although the surface flux of CH_4 is lower, the atmospheric lifetime is longer because the presence of O_2 and O_3 helps to shield photolysis of water vapor, slowing the rate of OH production, which our models show is the principal mechanism for CH_4 destruction for this atmosphere. Similarly, the production of $O(^1D)$ radicals from O_3 photolysis, a secondary mechanism for CH_4 destruction, is also reduced from that expected from the Sun owing to TRAPPIST-1's much lower NUV spectrum (Segura et al. 2005), and this also increases the buildup of CH_4 in the atmosphere.

In contrast, the Archean environment has a higher surface flux of CH_4 from its methanogenic biosphere and little to no O_3

to produce $O(^1D)$ even at the lower rate expected around M dwarfs. The expectation might be that the Archean would therefore have a higher abundance of CH_4 in its atmosphere, as is likely for Earth's Archean. However, the atmospheric lifetime of CH_4 in this much more reducing atmosphere is, paradoxically, lower than for the preindustrial Earth. This appears to be due to the strong far-UV flux of the host star and the lack of photochemical shielding from O_2 and O_3, which allows both efficient direct photolysis of CH_4 and a factor of two increase in the production of OH radicals from the photolysis of water vapor when compared to the preindustrial case. The shielding provided by O_2 and O_3 therefore works to increase the CH_4 abundance in the preindustrial Earth case (surface abundance of 450 ppm), despite having one-third the surface flux of CH_4, and enhances its detectability slightly over that of the Archean case (250 ppm), with the higher surface flux of CH_4 and more reducing atmosphere. As a final note, colder planets with a lower atmospheric water abundance could build up more CH_4, and the cold Archean case with 150 ppm was able to build up CH_4 to 474 ppm, a value very similar to that of the preindustrial Earth.

It is important to provide the caveat that these results are strongly dependent on our model assumptions and processes, whereas divergent evolution of an atmosphere and biosphere and a myriad of chemical, physical, and biological processes can interact to affect the buildup or suppression of atmospheric CH_4 on an exoplanet. In particular, CH_4 methanogenesis would have to evolve, and the productivity of any resultant CH_4 biosphere would be strongly dependent on the availability of substrates for methanogenesis, including H_2, CO_2, and organic compounds (Pavlov et al. 2003), the latter of which could be provided by additional microbial pathways that may be quite divergent from those on Earth. However, even high methanogenic productivity may not enable CH_4 atmospheric buildup, as sinks in the atmosphere, surface, and ocean, including anaerobic oxidation of methane, oxidizing compounds, and ocean sulfate, could all work to reduce atmospheric CH_4 buildup (Olson et al. 2016; Reinhard et al. 2017).

However, if present, the CO_2/CH_4 disequilibrium pair has both superior detectability of the two gases, which enhances the ability to quantify abundances, and the advantage of a relatively detectable false-positive indicator. If the CH_4 abundances can be retrieved from the spectrum, then calculations of whether the corresponding surface fluxes needed to maintain those abundances against photochemical destruction are higher or lower than those expected from geological sources would help assess whether a biogenic origin for the CH_4 was more likely (Krissansen-Totton et al. 2018a). The significant nondetection of CO at 4.6 μm, even for 100 transits, also implies that the false-positive scenario of the prebiotic Earth with vigorous volcanic outgassing from a reduced mantle (Krissansen-Totton et al. 2018a) is unlikely. However, we also show that confirming the false-positive scenario may be relatively straightforward and require fewer transits than the detection of the biosignature pair. For the prebiotic Earth case, we show that the 1.9% CO_2 generated by an outgassing from a heavily reduced mantle is of comparable detectability to the Archean methanogenic case, requiring three versus two transits for a 3σ detection. However, the CH_4 is significantly weaker in the false-positive case, despite the $200\times$ volcanic flux, requiring 40 transits compared with three transits for the methanogenic Archean. The false-positive indicator, CO, in

this case requires only seven transits in the volcanic false-positive scenario, instead of over 100 for the methanogenic biosphere.

In overview, our results suggest that the strong CO_2 and CH_4 features in the TRAPPIST-1 e with an Archean-Earth-like biosphere spectrum may be readily detectable even in the presence of clouds and potentially feasible, although more challenging, in the presence of a planet-wide hydrocarbon haze. Discriminating the presence of a false-positive, geological source for the CH_4 may also be quite straightforward owing to the strong CO signal this scenario produces.

4.5. The Habitability and Climate of Inhabited TRAPPIST-1 d

Our modeling work also revealed several interesting aspects of the potential habitability of inhabited TRAPPIST-1 planets and the impacts of biogenically generated compounds on planetary climate. We find that the likelihood of habitability for TRAPPIST-1 d is somewhat precarious, with greenhouse-rich Archean-like atmospheres conclusively going into runaway, but more modern-Earth-like O_2-dominated atmospheres barely escaping this process. This is in contrast to earlier results with 3D GCMs (Wolf 2017; Turbet et al. 2020), where TRAPPIST-1 d would go into runaway with only N_2 and H_2O. These discrepancies may be due to many differences in both input environment assumptions and model capabilities and limitations. For example, our environments differ from those of Wolf (2017) in their assumed stellar insolation, ocean fraction, and atmospheric composition, which in turn impacts planetary albedo, saturation, and humidity. Wolf (2017) uses 1.143 times Earth's insolation for TRAPPIST-1 d, while we use the more recent, lower value of 1.115 (Agol et al. 2021). Other factors in previous models that could lead to an increased probability of runaway include the low albedo and maximum humidity of 100% for the assumed 100% ocean planet, coupled with no ocean heat transport—an important heat redistribution mechanism on Earth (Trenberth & Caron 2001; Wunsch 2005)—whose absence would keep heat concentrated on the dayside hemisphere of the planet (Wolf 2017). In contrast, our models with an Earth-like land/ocean distribution use a Manabe & Wetherald (1967) formalism where drier downwelling columns counteract saturated upwelling columns, with only an 88% humidity overall at the surface. Our models also include biogenically generated CH_4 at relatively high abundance, which is known to produce a surface-cooling anti-greenhouse effect on planets orbiting M dwarfs (Ramirez & Kaltenegger 2018).

In sensitivity testing, the radiative effect of clouds has the greatest impact on our model atmospheres. Compared to 3D models with band k-coefficients (Wolf 2017), our 1D model uses multistream, multiscattering spectrum-resolving radiative transfer, which more accurately calculates the radiative effects of atmospheric gas and aerosol components. However, it cannot calculate the self-consistent atmospheric heat transport and the spatial distribution of clouds, which we instead approximate with radiatively active, realistic particle distributions and optical depths similar to those of Earth-like clouds, but with adjusted cloud heights appropriate for TRAPPIST-1 d (see Section 2.4.3). This approximation is somewhat justified by the total condensation flux for TRAPPIST-1 d being similar to that for our Earth validation, suggesting a similar level of cloud generation. However, under cloud cover, changing our TRAPPIST-1 d environment to an ocean-covered aqua planet

had little effect on surface temperature, due to the concomitant increase in surface latent heat flux as a result of the change in surface humidity to 100%. Lowering our cumulative TRAPPIST-1 d cloud optical depth from the nominal Earth-like value of $\tau = 2.25$ to 1.25 still resulted in a stable environment, albeit with a slightly higher temperature of 308 K (vs. 302 K). Additional work on studying the climate of TRAPPIST-1 d, in conjunction with upcoming observations, is warranted. Given that TRAPPIST-1 d is within the optimistic HZ of its parent star, whether it underwent, is in, or avoided runaway could serve as an important test for the limits of the HZ.

4.6. Climatic Effects of Biosignature Gases on TRAPPIST-1 e

Our work has also showed that biologically mediated atmospheric composition, from the production of trace gases to the formation of hazes, can have a profound effect on the planet's temperature–pressure profile and surface temperature, and consequently its habitability. While temperature structures on Earth are governed by water vapor and stratospheric O_3 absorption, the different atmospheric compositions considered here could produce atmospheric heating at a range of altitudes, via atmospheric absorbers such as CO_2 and biosignatures such as CH_4 and hydrocarbon hazes. These biogenic components can impact climate and surface temperature through radiative greenhouse forcing. Methane can generate an anti-greenhouse and cool the surface of planets orbiting M dwarfs (Ramirez & Kaltenegger 2018), and we have shown that there can be significant contributions to greenhouse warming from sulfur organics.

The methyl-based complex sulfur biosignature gases assessed here, including CH_3Cl, CH_3SH, DMS, and DMDS, can also strongly impact planetary climate via their extensive absorption bands in both the mid- and near-infrared, where there is a peak in incident radiation from the TRAPPIST-1 host star. These molecules impact climate as a result of both the mid-infrared absorption of outgoing radiation and the absorption of incoming stellar radiation in the near-infrared (Lincowski 2020). Due to photochemistry, the higher amounts of methyl-containing gases also result in more available simple hydrocarbons in the atmosphere, such as C_2H_2, C_2H_4, and C_2H_6, which are themselves greenhouse gases. The increased hydrocarbons can also allow the formation of a hydrocarbon haze, which we show produces a more isothermal stratosphere via a combination of scattering and absorption, and can result in weak cooling of the surface for planets orbiting M dwarfs (Arney et al. 2017). We also found that enriched levels of hydrocarbon biosignature gases, protected from photolysis by a haze, have a complementary absorption band in the mid-infrared and can create a pseudocontinuum longward of 8 μm that is even more effective at blanketing and absorbing outgoing radiation to warm the surface.

The destruction of potential biosignatures by photochemical reactions driven by TRAPPIST-1's UV spectrum can also modify the composition and vertical structure of the planetary atmosphere. Two key atmospheric processes that are more pronounced on our simulated TRAPPIST-1 planets compared to Earth are the formation of hydroxyl (OH) radicals via direct photolysis of water vapor—which can in turn reduce the abundance of O_3—and the specified enhanced CH_3Cl flux, which produces free chlorine, another powerful catalyst that destroys O_3. This photochemical loss of O_3, combined with the relative lack of stellar NUV or visible light where O_3 absorbs,

works to eliminate the significance of O_3 in determining the planetary temperature structure. Increases in OH production and the concomitant loss of CH_4 can also enhance hydrocarbon production, which enhances greenhouse warming up until a thick haze forms. Additional OH destroys CH_4, which releases CH_3, which in the absence of abundant oxygen recombines to form C_2H_6 or other hydrocarbons. For atmospheres containing abundant chlorine, Cl can also react with methane, reducing its abundance and cooling the cold trap, which in turn reduces stratospheric water vapor. Reducing CH_4 also reduces its anti-greenhouse effect, warming the surface. It is clear from this work that biologically mediated gases are key components of the complex atmospheric climate–chemistry balance, and future work will explore their impact on planetary habitability.

5. Conclusions

We have simulated and reviewed the potential detectability of a range of biosignature molecules and associated environments in JWST transmission spectra of TRAPPIST-1 d and e. The simulation of the modern preindustrial Earth for TRAPPIST-1 d did not show the larger signals expected owing to the planet's smaller size and the atmosphere's larger scale height, and the biosignatures O_2, O_3, and CH_4 were not detectable in less than 100 transits owing to the formation of a high-altitude cloud in this hot, wet atmosphere. We confirm previous work in estimating the detectability of biosignatures for modern-Earth-like TRAPPIST-1 e environments that shows that detecting either O_2 or O_3 is extremely challenging. We also explored the potential for CH_3Cl to act as a proxy for oxygenic photosynthesis from vegetation and found that we would still need at least 100 times Earth's current flux of this gas, or 20 times the flux expected from tropical vegetation, to produce a signal that is detectable to JWST in under 100 transits. Consequently, despite the high abundance of O_2 in Earth's atmosphere and strong absorption by O_3 in the mid-infrared, an Earth-like photosynthetic biosphere is largely invisible to JWST, and we await the first light of ground-based extremely large telescopes (ELTs) to search for O_2 on terrestrial exoplanets. We also explored the detectability of more complex organics generated by a sulfur-dominated biosphere, as well as their photochemical by-products, but show that MIRI is unlikely to detect the signals from these biosignatures.

We find that the CH_4/CO_2 is the most detectable biosignature for all of the TRAPPIST-1 e habitable environment/metabolism scenarios that we considered, including for a modern preindustrial Earth with both oxygenic photosynthesis and a methanogenic biosphere. This result indicates that the signal of a methanogenic biosphere, even in the presence of other, more dominant metabolisms, may be the most detectable to JWST, and it may also persist throughout the evolution of a planet's biosphere and atmosphere. This enhanced detectability for methanogenesis is due in part to the higher CO_2 abundance needed to warm the planets, the increased photochemical lifetime for CH_4 for planets orbiting M-dwarf stars, and the strength of the CO_2 and CH_4 spectral features in the NIRSpec wavelength range. However, it will be important to invest additional observing time to help interpret whether or not the CH_4/CO_2 disequilibrium pair is in fact more likely to be due to biological processes. Nevertheless, we conclude that JWST may have the capability to execute the first search for signs of life on terrestrial exoplanets, and with a biosignature that, given Earth's example, may persist throughout a planet's history.

Appendix

This appendix contains the details for the new convection formalism implemented in the VPL Climate model (Appendix A) and the first validation of the model in radiative-convective mode with photochemistry (Appendix B).

Appendix A
The Convection Model

As described in Lincowski et al. (2018), for the VPL Climate model, the convective heating rates and transport are defined within a mixing-length formulation to maintain heat and mass fluxes linked to physical properties of the atmosphere. The convective heating rate is related to the divergence of the convective energy flux:

$$q_c = \Gamma \frac{\partial F_c}{\partial P}, \qquad (A1)$$

where P is pressure and the adiabatic lapse rate is $\Gamma_{ad} = g/c_p$, where c_p is the specific heat capacity and g is the acceleration due to gravity. The convective energy flux F_c is given by

$$F_c = -\rho c_p K_h \left(\frac{\partial T}{\partial z} + \Gamma_{ad} \right), \qquad (A2)$$

where K_h is the eddy diffusion coefficient for heat. The atmosphere is unstable to convection when $\partial T/\partial z < -\Gamma_{ad}$. In this case, the eddy diffusion coefficient for heat K_h is given by (e.g., Gierasch & Goody 1968)

$$K_h = kl^2 \left[-\frac{g}{T} \left(\frac{\partial T}{\partial z} + \Gamma_{ad} \right) \right]^{1/2}, \qquad (A3)$$

where k is a proportionality constant equal to 1.32 (Priestley 1959) and l is the mixing length. For the mixing length, we use an asymptotic profile given by Blackadar (1962):

$$l = \frac{k_{vk} z}{1 + k_{vk} z/l_0}. \qquad (A4)$$

Here, k_{vk} is von Kármán's constant and l_0 is the mixing length in the free atmosphere, which we express as

$$l_0 = f_z H, \qquad (A5)$$

where H is the pressure scale height, given by

$$H = \frac{RT}{\mu g}, \qquad (A6)$$

where R is the ideal gas constant, μ is the mean molar mass, and f_z is the proportionality constant.

For mass fluxes, in particular to improve transport in neutral atmospheric layers, we update the convective parameterization to a Richardson-number-based scheme, similar to that used in other 1D and 3D models with solar system terrestrial heritage (Savijarvi 1999; Collins et al. 2004). The kinematic mass flux is

$$F_m = -\rho K_m \frac{\partial r}{\partial z}. \qquad (A7)$$

Here K_m is the eddy diffusion coefficient for mass transport and r is the mixing ratio of the condensable species. The eddy diffusion coefficient in the Richardson number formulation is specified as

$$K_m = l^2 \left| \frac{du}{dz} \right| f(\text{Ri}) + K_{m,0} \left(\frac{\rho}{\rho_0} \right)^{1/2}$$
$$\times (1 - e^{-P/P_0}) + K_{m,1}, \qquad (A8)$$

where ρ is density; du/dz is the wind shear, a calibration variable here, which we take to be a constant value of $0.02\,\text{s}^{-1}$ (consistent with wind shear measurements of Earth in stratocumulus clouds; Ryan et al. 1972; Noonkester 1978; Brost et al. 1982); and $f(\text{Ri})$ is the stability function, given as (see Savijarvi 1999; Collins et al. 2004)

$$f(\text{Ri}) = \begin{cases} (1 - 18\text{Ri})^{1/4}, & \text{Ri} < 0 \\ \frac{1 - (1 + \exp(-10(\text{Ri}-1)))^{-1}}{1 + 18\text{Ri}(1 + 10\text{Ri})^{5/3}}, & \text{Ri} > 0 \end{cases}, \qquad (A9)$$

and here the Richardson number is calculated as

$$\text{Ri} = \frac{g}{T} \frac{dT/dz + \Gamma}{(du/dz)^2}. \qquad (A10)$$

This stability formulation provides a smaller stability function than the comparable references, but since we prescribe and do not calculate du/dz, the combination of these terms results in a good validation for Earth (see Appendix B). The density- and pressure-dependent terms of Equation (A8) represent the breaking of gravity waves (Lindzen & Forbes 1983).

Condensation is formulated differently than in Lincowski et al. (2018); condensation is calculated in a flux formulation more similar to kinetic fluxes, where the heating rate due to latent heat release is the divergence of the latent heat flux through the layer, the same as Equation (A1), but the differential latent heat flux is given by

$$\partial F_{c,lh} \approx \Delta F_{c,lh} = L\rho \Delta z \frac{\Delta r_{c,lh}}{\Delta t}, \qquad (A11)$$

where L is the latent heat of evaporation and $\Delta r_{c,lh}$ is the difference in layer mixing ratio and the mixing ratio criteria for

condensation, which includes condensable gas mixed into the layer owing to vertical transport during the time step.

At globally averaged temperatures, it is unlikely that globally averaged water mixing ratios will approach saturation, particularly in the troposphere, where temperatures are most spatially heterogeneous. Nonetheless, there is still condensation, evaporation, and latent heat exchange due to saturation of individual air parcels. The simplest solution remains to use a different mixing ratio criterion for condensation. Here we use a simplified and generalized form of Equation (2) from Manabe & Wetherald (1967) for Earth, plus a term to increase the criteria to saturation in the stratosphere:

$$rh = rh_s \max\left(\frac{p}{p_s}, 0.1\right) + \max\left(\frac{(1000\mathrm{Pa})/p - 0.1}{0.9}, 0\right).$$
(A12)

The radiative effects of clouds in our model are parameterized using altitude-dependent profiles of differential optical depth, which is described in more detail in Section 2.4.3. The types of clouds used were originally specified from Earth spectral retrievals (Robinson et al. 2011) and broken into high-altitude ice (cirrus) clouds and low-altitude water (stratocumulus) clouds. We continue that convention here and use optically thin ice clouds spanning the upper layers of our model where condensation occurs and specify optically thick water clouds spanning the lower layers of our model where condensation occurs. The profiles used are scaled in pressure space from the original Earth pressure profiles. This specification for clouds results in multilayer, radiatively active, Earth-like clouds spanning the vertical regions of the atmosphere where our model is showing condensation that would result in cloud formation.

Appendix B
Earth Coupled Climate–Photochemistry Validation

The VPL Climate model has been previously validated for Earth in radiative equilibrium (Robinson & Crisp 2018) with fixed gas profiles and clear-sky conditions. In this section, we demonstrate validation of this model in radiative-convective mode, with condensation and associated latent heat fluxes that control the climate profile of Earth, coupled to photochemistry (Kasting et al. 1993; Kopparapu 2013). We include vertically resolved clouds, where the aerosol distribution and optical depths of vertically distributed cirrus (water-ice) and stratocumulus (water) clouds have been tuned to represent the globally averaged fluxes observed in the atmosphere of Earth (Trenberth et al. 2009).

As shown in Figure 19, we largely reproduce the globally averaged temperature structure of Earth, including surface temperature and overall structure. Our simulation exhibits a tropopause and a stratopause that are less sharply defined than the Earth average.

In Table 5, we compare the radiative, sensible heat, and latent heat fluxes with sophisticated Earth 3D climate models (Trenberth et al. 2009). Radiative fluxes are in good agreement with the Earth climate data. The surface sensible heat fluxes are sensitive to surface assumptions and are small compared to the surface latent heat flux. The sensible heat flux is also small compared to Earth global values, but the combined sensible and latent heat flux matches Earth conditions.

We have also separately validated our photochemical model, *Atmos*, for Earth. The lower boundary conditions are listed in Table 6, and the resultant chemical profiles are shown in Figure 20. The total ozone column depth is slightly low (5.8×10^{18} molecules cm^{-2} vs. 8.0×10^{18} molecules cm^{-2}), but generally the profiles are in excellent agreement with Earth average measurements for key constituents H_2O, O_3, HCl, CH_3Cl, N_2O, CH_4, and C_2H_6S. Our model uses primarily surface fluxes rather than fixed mixing ratios to obtain these results, with the exception of N_2, O_2, and CO_2. Another exception is NO, for which the flux is adjusted for global chemical agreement and stands in for total NO_x and other pollutants not included in our model.
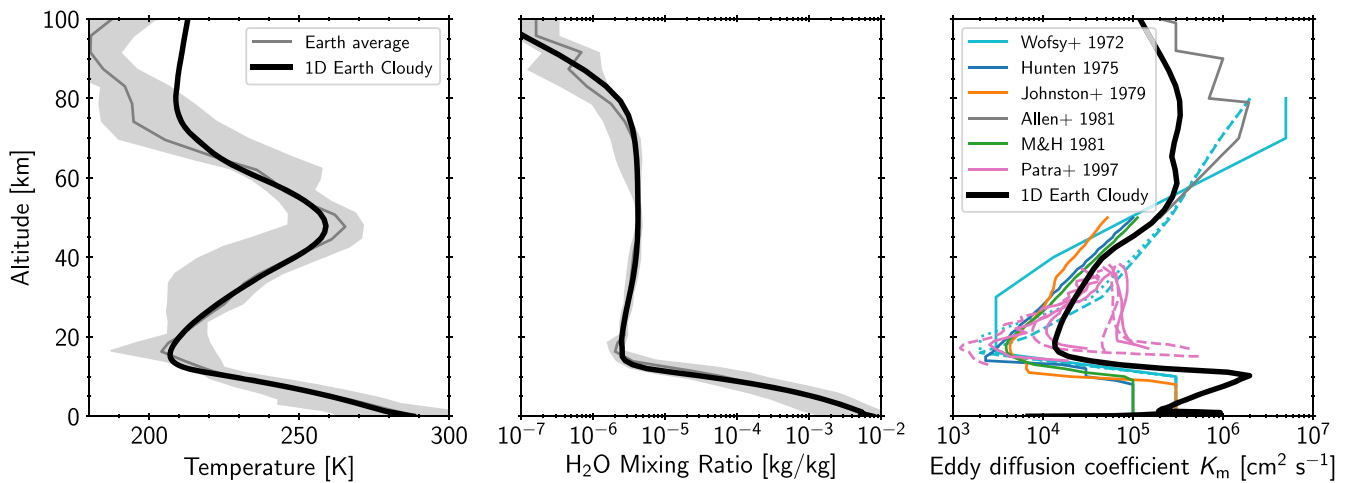

Figure 19. Left and middle: comparison of VPL Climate 1D temperature and H_2O mixing ratio profiles with Earth retrieval data from 4/23/2008 in the VPL 3D Spectral Earth model (Robinson et al. 2011). Right: comparison of VPL Climate 1D eddy diffusion coefficient for mass with retrieved Earth values (Wofsy et al. 1972; Hunten 1975; Johnston et al. 1979; Allen et al. 1981; Massie & Hunten 1981; Patra & Lal 1997). The VPL Climate temperature and water vapor profiles are a good match to average Earth conditions, and the modeled eddy diffusion coefficient is within observed values.
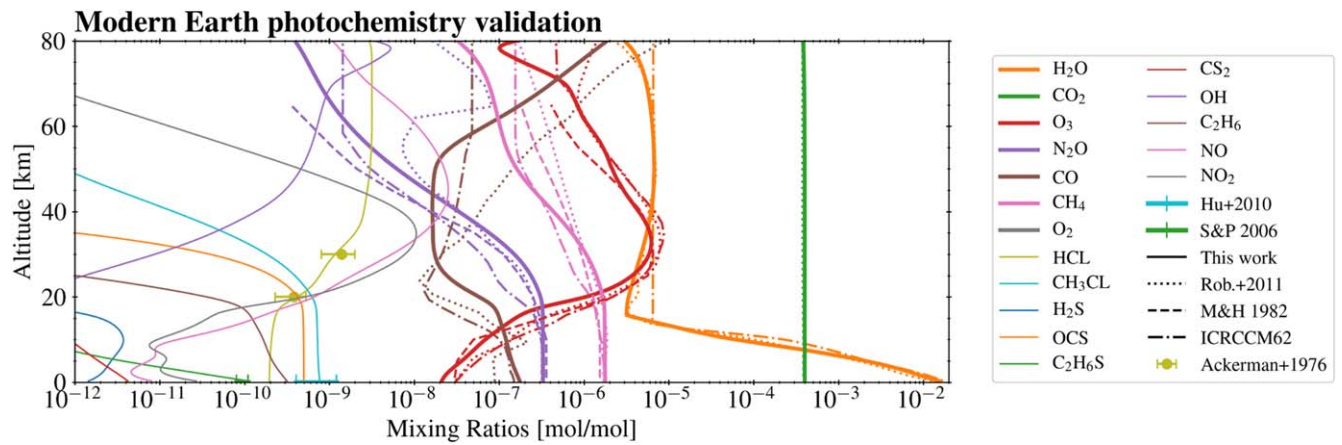
Figure 20. Mixing ratio profiles with Earth data sources, demonstrating a new, comprehensive validation for our photochemical model. Our model has excellent agreement with global Earth data, using measured fluxes for key gases for the surface boundary condition. Here the photochemical model uses the average temperature from the data-derived 3D Spectral Earth model (Robinson et al. 2011). Calculated mixing ratio profiles of key species are shown with solid lines. For comparison, plotted are an average derived from the 3D Spectral Earth model (Robinson et al. 2011; dotted lines), measurements from Massie & Hunten (1981; dashed lines), the ICRCCM Earth midlatitude summer sounding case 62 (dashed–dotted lines), and data points for HCl (Ackerman et al. 1976), CH₃Cl (Hu et al. 2010), and C₂H₆S (Seinfeld & Pandis 2006, Table 2.3).

Table 5
Comparison of the Global Energy Budget for Earth (Trenberth et al. 2009) with VPL Climate Model Results

	Trenberth et al. (2009)		VPL Climate Earth
Surface temperature (K)	289.1	(288.7–289.25)	288.21
Direct solar	341.3	(339.1–341.8)	344.4
Net reflected solar	101.9	(94.6–117.0)	102.0
Solar reflected by atmosphere and clouds	78.8	(69–82.4)	79.1
Solar absorbed by atmosphere and clouds	78.2	(64.4-78.2)	78.4
Solar reflected at surface	23.1	(22.8–45.2)	23.0
Net solar flux at surface	161.2	(160.4–169.8)	163.9
Net thermal flux at surface	63	(48.5–72.8)	67.6
Outgoing thermal flux	238.5	(235.6–253.6)	243.7
Surface sensible heat flux	17	(15.3–24)	0.7
Surface latent heat flux	80	(78–85.1)	95.4

Note. Except surface temperature, all quantities are flux (W m⁻²). Values from Trenberth et al. (2009) include the range from several studies compared (in parentheses). The fluxes for our VPL Climate Earth model are in excellent agreement with Trenberth et al. (2009).

Table 6
Earth Validation Lower Boundary Conditions

Species	Boundary Condition
O	$v_{dep} = 1.$
O₂	$r_0 = 0.21$
H₂O	$rh_0 = 0.88$
H	$v_{dep} = 1.$
OH	$v_{dep} = 1.$
HO₂	$v_{dep} = 1.$
H₂O₂	$v_{dep} = 0.2$
H₂	$v_{dep} = 2.0 \times 10^{-3}$, $F = 4.0 \times 10^8$ dist. 16 km (Warneck 1999; Steinbacher et al. 2007)
CO	$F = 2.7 \times 10^{11}$ (Seinfeld & Pandis 2006, Section 2.4.5)
HCO	$v_{dep} = 1.$
H₂CO	$v_{dep} = 0.2$
CH₄	$F = 1.5 \times 10^{11}$ (Stocker et al. 2013)
C₂H₆	$F = 2.0 \times 10^9$ (Xiao et al. 2008)
NO	$F = 4.0 \times 10^9$
NO₂	$v_{dep} = 3.0 \times 10^{-3}$ (Domagal-Goldman et al. 2011)

Table 6
(Continued)

Species	Boundary Condition
HNO	$v_{\text{dep}} = 1.$
H_2S	$v_{\text{dep}} = 0.02$, $F = 2.0 \times 10^8$ dist. 16 km (Seinfeld & Pandis 2006, Table 2.2)
SO_2	$v_{\text{dep}} = 1.$, $F = 1.35 \times 10^9$ dist. 16 km (Sehmel 1980), volcanic: (Carn et al. 2017)
H_2SO_4	$F = 7.0 \times 10^8$ (Hu et al. 2012), (Seinfeld & Pandis 2006, Table 2.2)
HSO	$v_{\text{dep}} = 1.$
OCS	$F = 7.0 \times 10^6$ (Seinfeld & Pandis 2006, Table 2.2), (Kettle et al. 2001)
O_3	$v_{\text{dep}} = 0.07$ (Hauglustaine et al. 1994)
HNO_3	$v_{\text{dep}} = 0.2$
N_2O	$F = 1.53 \times 10^9$ (Stocker et al. 2013)
HO_2NO_2	$v_{\text{dep}} = 0.2$
CO_2	$r_0 = 4.0 \times 10^{-4}$
CS_2	$F = 2.0 \times 10^7$ (Seinfeld & Pandis 2006, Table 2.2)
$C_2H_6S(DMS)$	$F = 3.3 \times 10^9$ (Lana et al. 2011)
CH_3Cl	$F = 3.0 \times 10^8$
Ar	$r_0 = 0.01$
N_2	$r_0 = 0.78$

Note. All unlisted species have a lower boundary condition $v_{\text{dep}} = 0$. Deposition velocities (v_{dep}) are given in cm s^{-1}, fluxes (F) are given in molecules cm^{-2} s^{-1}, r_0 is a fixed surface mixing ratio, and rh_0 is the surface relative humidity. SO_2 excludes anthropogenic sources. NO flux was chosen to obtain proper chemical cycles. Deposition velocities not otherwise attributed are taken from Domagal-Goldman et al. (2011).

ORCID iDs

Victoria S. Meadows https://orcid.org/0000-0002-1386-1710
Andrew P. Lincowski https://orcid.org/0000-0003-0429-9487
Jacob Lustig-Yaeger https://orcid.org/0000-0002-0746-1980

References

Ackerman, M., Frimout, D., Girard, A., Gottignies, M., & Muller, C. 1976, GeoRL, 3, 81
Agol, E., Dorn, C., Grimm, S. L., et al. 2021, PSJ, 2, 1
Allen, M., Yung, Y. L., & Waters, J. W. 1981, JGR, 86, 3617
Arney, G., Domagal-Goldman, S. D., Meadows, V. S., et al. 2016, AsBio, 16, 873
Arney, G., Domagal-Goldman, S. D., & Meadows, V. S. 2018, AsBio, 18, 311
Arney, G., Meadows, V., Crisp, D., et al. 2014, JGRE, 119, 1860
Arney, G. N. 2019, ApJL, 873, L7
Arney, G. N., Meadows, V. S., Domagal-Goldman, S. D., et al. 2017, ApJ, 836, 49
Baraffe, I., Homeier, D., Allard, F., & Chabrier, G. 2015, A&A, 577, A42
Baranov, Y. I., Lafferty, W. J., & Fraser, G. T. 2004, JMoSp, 228, 432
Barstow, J. K., & Irwin, P. G. J. 2016, MNRAS, 461, L92
Barth, P., Carone, L., Barnes, R., et al. 2021, AsBio, 21, 1325
Batalha, N., Espinoza, N., Fix, M., et al. 2022, natashabatalha/PandExo: Release 2.0 (v2.0)., Zenodo. doi:10.5281/zenodo.7473939
Batalha, N. E., Lewis, N. K., Line, M. R., Valenti, J., & Stevenson, K. 2018, ApJ, 856, L34
Batalha, N. E., Mandell, A., Pontoppidan, K., et al. 2017, PASP, 129, 064501
Baum, B. A., Yang, P., Heymsfield, A. J., et al. 2014, JQSRT, 146, 123
Bétrémieux, Y., & Kaltenegger, L. 2014, ApJ, 791, 7
Bixel, A., & Apai, D. 2021, AJ, 161, 228
Blackadar, A. K. 1962, JGR, 67, 3095
Blei, E., Heal, M. R., & Heal, K. V. 2010, BGeo, 7, 3657
Bolmont, E., Selsis, F., Owen, J. E., et al. 2017, MNRAS, 464, 3728
Brost, R. A., Wyngaard, J. C., & Lenschow, D. H. 1982, JAtS, 39, 818
Butler, J. H. 2000, Natur, 403, 260
Canfield, D. E., Rosing, M. T., & Bjerrum, C. 2006, RSPTA, 361, 1819

Carn, S. A., Fioletov, V. E., McLinden, C. A., Li, C., & Krotkov, N. A. 2017, NatSR, 7, 44095
Catling, D. C., & Kasting, J. F. 2017, Atmospheric Evolution on Inhabited and Lifeless Worlds (Cambridge: Cambridge Univ. Press)
Catling, D. C., & Zahnle, K. J. 2020, SciA, 6, eaax1420
Cawood, P. A., Hawkesworth, C., & Dhuime, B. 2013, GSA Bulletin, 125, 14
Charnay, B., Forget, F., Wordsworth, R., et al. 2013, JGRD, 118, 10,414
Chaverot, G., Turbet, M., Bolmont, E., & Leconte, J. 2022, A&A, 658, A40
Collins, W. D., Rasch, P. J., Boville, B. A., et al. 2004, Description of the NCAR Community Atmosphere Model (CAM 3.0) No. NCAR/TN-464 +STR, Univ. Corporation for Atmospheric Research
Crisp, D. 1997, GeoRL, 24, 571
Currie, M. H., Meadows, V. S., & Rasmussen, K. C. 2023, PSJ, 4, 83
de Wit, J., Wakeford, H. R., Lewis, N. K., et al. 2018, NatAs, 2, 214
Delrez, L., Gillon, M., Triaud, A. H. M. J., et al. 2018, MNRAS, 475, 3577
Des Marais, D. J. 2000, Sci, 289, 1703
Des Marais, D. J., Harwit, M. O., Jucks, K. W., et al. 2002, AsBio, 2, 153
DeWitt, H. L., Trainer, M. G., Pavlov, A. A., et al. 2009, AsBio, 9, 447
Domagal-Goldman, S. D., Meadows, V. S., Claire, M. W., & Kasting, J. F. 2011, AsBio, 11, 419
Ducrot, E., Gillon, M., Delrez, L., et al. 2020, A&A, 640, A112
Fauchez, T. J., Turbet, M., Villanueva, G. L., et al. 2019, ApJ, 887, 194
Fauchez, T. J., Villanueva, G. L., Schwieterman, E. W., et al. 2020, NatAs, 4, 372
Feng, Y. K., Robinson, T. D., Fortney, J. J., et al. 2018, AJ, 155, 200
Flückiger, J., Monnin, E., Stauffer, B., et al. 2002, GBioC, 16, 1010
Forget, F., Wordsworth, R., Millour, E., et al. 2013, Icar, 222, 81
Fulton, B. J., Petigura, E. A., Howard, A. W., et al. 2017, AJ, 154, 109
Gialluca, M., Robinson, T., Rugheimer, S., & Wunderlich, F. 2021, PASP, 133, 054401
Gierasch, P., & Goody, R. 1968, P&SS, 16, 615
Gillon, M., Triaud, A. H., Demory, B.-O., et al. 2017, Natur, 542, 456
Goldblatt, C., Robinson, T. D., Zahnle, K. J., & Crisp, D. 2013, NatGe, 6, 661
Gordon, I. E., Rothman, L. S., Hill, C., et al. 2017, JQSRT, 203, 3
Greene, T. P., Line, M. R., Montero, C., et al. 2016, ApJ, 817, 17
Grimm, S. L., Demory, B.-O., Gillon, M., et al. 2018, A&A, 613, A68
Gruszka, M., & Borysow, A. 1997, Icar, 129, 172
Guzmán-Marmolejo, A., Segura, A., & Escobar-Briones, E. 2013, AsBio, 13, 550
Haan, D., & Raynaud, D. 1998, TellB, 50, 253

Hardegree-Ullman, K. K., Apai, D., Bergsten, G. J., Pascucci, I., & López-Morales, M. 2023, AJ, 165, 267

Harman, C., Felton, R., Hu, R., et al. 2018, ApJ, 866, 56

Harman, C. E., Schwieterman, E. W., Schottelkotte, J. C., & Kasting, J. F. 2015, ApJ, 812, 137

Harris, C. R., Millman, K. J., van der Walt, S. J., et al. 2020, Natur, 585, 357

Hartmann, J.-M., Boulet, C., & Toon, G. C. 2017, JGRD, 122, 2419

Hauglustaine, D. A., Granier, C., Brasseur, G. P., & MéGie, G. 1994, JGR, 99, 1173

Hawkesworth, C. J., Cawood, P. A., Dhuime, B., & Kemp, T. I. 2017, AREPS, 45, 169

Hitchcock, D. R., & Lovelock, J. E. 1967, Icar, 7, 149

Hoehler, T., Bains, W., Davila, A., Parenteau, N., & Pohorille, A. 2020, in Planetary Astrobiology, ed. V. S. Meadows et al. (Tucson, AZ: Univ. Arizona Press), 37

Hori, Y., & Ogihara, M. 2020, ApJ, 889, 77

Hörst, S. M., He, C., Ugelow, M. S., et al. 2018, ApJ, 858, 119

Hu, L., Yvon-Lewis, S. A., Liu, Y., Salisbury, J. E., & O'Hern, J. E. 2010, GBioC, 24, GB1007

Hu, R., Cahoy, K., & Zuber, M. T. 2012, JGRE, 117, E07002

Hu, R., Peterson, L., & Wolf, E. T. 2020, ApJ, 888, 122

Hunten, D. M. 1975, PNAS, 72, 4711

Hunter, J. D. 2007, CSE, 9, 90

Jakobsen, P., Ferruit, P., de Oliveira, C. A., et al. 2022, A&A, 661, A80

Johnson, T. J., Sams, R. L., & Sharpe, S. W. 2004, Proc. SPIE, 5269, 159

Johnston, H. S., Serang, O., & Podolske, J. 1979, JGR, 84, 5077

Karman, T., Gordon, I. E., van der Avoird, A., et al. 2019, Icar, 328, 160

Karman, T., Koenis, M. A. J., Banerjee, A., et al. 2018, NatCh, 10, 549

Kasting, J., Liu, S., & Donahue, T. 1979, JGR, 84, 3079

Kasting, J. F., Pollack, J. B., & Ackerman, T. P. 1984, Icar, 57, 335

Kasting, J. F., Whitmire, D. P., & Reynolds, R. T. 1993, Icar, 101, 108

Keller-Rudek, H., Moortgat, G. K., Sander, R., & Sörensen, R. 2013, ESSD, 5, 365

Kettle, A., Rhee, T., Von Hobe, M., et al. 2001, JGR, 106, 12193

Kharecha, P., Kasting, J., & Siefert, J. 2005, Gbio, 3, 53

Kopparapu, R. K. 2013, ApJL, 767, L8

Kopparapu, R. K., Wolf, E. T., Arney, G., et al. 2017, ApJ, 845, 5

Kopparapu, R. K., Wolf, E. T., Haqq-Misra, J., et al. 2016, ApJ, 819, 84

Korenaga, J. 2018, RSPTA, 376, 20170408

Krissansen-Totton, J., Bergsman, D. S., & Catling, D. C. 2016, AsBio, 16, 39

Krissansen-Totton, J., & Fortney, J. J. 2022, ApJ, 933, 115

Krissansen-Totton, J., Garland, R., Irwin, P., & Catling, D. C. 2018a, AJ, 156, 114

Krissansen-Totton, J., Olson, S., & Catling, D. C. 2018b, SciA, 4, eaao5747

Lafferty, W. J., Solodov, A. M., Weber, A., Olson, W. B., & Hartmann, J.-M. 1996, ApOpt, 35, 5911

Lan, X., Thoning, K., & Dlugokencky, E. 2023, Trends in globally-averaged CH_4, N_2O, and SF_6 determined from NOAA Global Monitoring Laboratory measurement, Version 2023-01

Lana, A., Bell, T., Simó, R., et al. 2011, GBioC, 25, GB1004

Lee, Y. J., Sagawa, H., Haus, R., et al. 2016, JGRE, 121, 1737

Leung, M., Schwieterman, E. W., Parenteau, M. N., & Fauchez, T. J. 2022, ApJ, 938, 6

Lin, Z., MacDonald, R. J., Kaltenegger, L., & Wilson, D. J. 2021, MNRAS, 505, 3562

Lincowski, A. P. 2020, PhD thesis, Univ. Washington, Seattle

Lincowski, A. P., Meadows, V. S., Crisp, D., et al. 2018, ApJ, 867, 76

Lincowski, A. P., Meadows, V. S., Crisp, D., et al. 2021, ApJL, 908, L44

Lindzen, R., & Forbes, J. 1983, JGR, 88, 6549

Lopez-Morales, M., Ben-Ami, S., Gonzalez-Abad, G., et al. 2019, AJ, 158, 24

Lovelock, J. E. 1975, RSPSB, 189, 167

Lovis, C., Snellen, I., Mouillet, D., et al. 2017, A&A, 599, A16

Lustig-Yaeger, J., Meadows, V. S., & Lincowski, A. P. 2019, AJ, 158, 27

Lyons, T. W., Reinhard, C. T., & Planavsky, N. J. 2014, Natur, 506, 307

Manabe, S., & Wetherald, R. T. 1967, JAtS, 24, 241

Mann, A. W., Dupuy, T., Kraus, A. L., et al. 2019, ApJ, 871, 63

Marty, B., & Tolstikhin, I. N. 1998, ChGeo, 145, 233

Massie, S. T., & Hunten, D. M. 1981, JGR, 86, 9859

Maté, B., Lugez, C., Fraser, G. T., & Lafferty, W. J. 1999, JGRD, 104, 30585

Meadows, V. S. 2017, AsBio, 17, 1022

Meadows, V. S., Arney, G. N., Schwieterman, E. W., et al. 2018, AsBio, 18, 133

Meadows, V. S., & Crisp, D. 1996, JGR, 101, 4595

Mikal-Evans, T. 2022, MNRAS, 510, 980

Misra, A., Meadows, V., & Crisp, D. 2014, ApJ, 792, 61

Moore, J. F. 1972, PhD thesis, Columbia Univ.

Moran, S. E., Hörst, S. M., Batalha, N. E., Lewis, N. K., & Wakeford, H. R. 2018, AJ, 156, 252

Morley, C. V., Kreidberg, L., Rustamkulov, Z., Robinson, T., & Fortney, J. J. 2017, ApJ, 850, 121

Muñoz, A. G., Osorio, M. Z., Barrena, R., et al. 2012, ApJ, 755, 103

Nicewonger, M. R., Verhulst, K. R., Aydin, M., & Saltzman, E. S. 2016, GeoRL, 43, 214

Nikitin, A., Dmitrieva, T., & Gordon, I. 2016, JQSRT, 177, 49

Noonkester, V. R. 1978, BAMS, 59, 522

Olson, S., Jansen, M. F., Abbot, D. S., Halevy, I., & Goldblatt, C. 2022, GeoRL, 49, e2021GL095748

Olson, S. L., Reinhard, C. T., & Lyons, T. W. 2016, PNAS, 113, 11447

Ozaki, K., Tajika, E., Hong, P. K., Nakagawa, Y., & Reinhard, C. T. 2018, NatGe, 11, 55

Patra, P. K., & Lal, S. 1997, JASTP, 59, 1149

Pavlov, A. A., Brown, L. L., & Kasting, J. F. 2001a, JGR, 106, 23267

Pavlov, A. A., Hurtgen, M. T., Kasting, J. F., & Arthur, M. A. 2003, Geo, 31, 87

Pavlov, A. A., Kasting, J. F., Eigenbrode, J. L., & Freeman, K. H. 2001b, Geo, 29, 1003

Peacock, S., Barman, T., Shkolnik, E. L., Hauschildt, P. H., & Baron, E. 2019, ApJ, 871, 235

Pidhorodetska, D., Fauchez, T. J., Villanueva, G. L., Domagal-Goldman, S. D., & Kopparapu, R. K. 2020, ApJL, 898, L33

Pilcher, C. B. 2003, AsBio, 3, 471

Planavsky, N. J., Asael, D., Hofmann, A., et al. 2014a, NatGe, 7, 283

Planavsky, N. J., Reinhard, C. T., Wang, X., et al. 2014b, Sci, 346, 635

Pontoppidan, K. M., Pickering, T. E., Laidler, V. G., et al. 2016, Proc. SPIE, 9910, 991016

Priestley, C. H. B. 1959, QJRMS, 86, 290

Ramirez, R. M., & Kaltenegger, L. 2018, ApJ, 858, 72

Ranjan, S., Schwieterman, E. W., Harman, C., et al. 2020, ApJ, 896, 148

Reinhard, C. T., Olson, S. L., Schwieterman, E. W., & Lyons, T. W. 2017, AsBio, 17, 287

Rhew, R. C., Miller, B. R., & Weiss, R. F. 2000, Natur, 403, 292

Robinson, T. D. 2011, ApJ, 741, 51

Robinson, T. D. 2017, ApJ, 836, 236

Robinson, T. D., & Crisp, D. 2018, JQSRT, 211, 78

Robinson, T. D., & Marley, M. S. 2014, ApJ, 785, 158

Robinson, T. D., Meadows, V. S., Crisp, D., et al. 2011, AsBio, 11, 393

Rogers, L. A. 2015, ApJ, 801, 41

Rugheimer, S., Kaltenegger, L., Segura, A., Linsky, J., & Mohanty, S. 2015, ApJ, 809, 57

Ryan, R. T., Blau, H. H. J., von Thüna, P. C., Cohen, M. L., & Roberts, G. D. 1972, JApMe, 11, 149

Sagan, C., & Chyba, C. 1997, Sci, 276, 1217

Saito, T., & Yokouchi, Y. 2008, GeoRL, 35, L07103

Savijarvi, H. 1999, QJRMS, 125, 483

Schwieterman, E. W., Kiang, N. Y., Parenteau, M. N., et al. 2018, AsBio, 18, 663

Schwieterman, E. W., Reinhard, C. T., Olson, S. L., et al. 2019, ApJ, 874, 9

Seager, S., Bains, W., & Petkowski, J. 2016, AsBio, 16, 465

Segelstein, D. J. 1981, PhD thesis, Univ. Missouri-Kansas City

Segura, A., Kasting, J. F., Meadows, V., et al. 2005, AsBio, 5, 706

Sehmel, G. A. 1980, AtmEn (1967), 14, 983

Seinfeld, J., & Pandis, S. 2006, Atmospheric Chemistry and Physics (New York: Wiley)

Shields, A. L., Bitz, C. M., Meadows, V. S., Joshi, M. M., & Robinson, T. D. 2014, ApJL, 785, L9

Shields, A. L., Meadows, V. S., Bitz, C. M., et al. 2013, AsBio, 13, 715

Spiering, F. R., Kiseleva, M. B., Filippov, N. N., van Kesteren, L., & van der Zande, W. J. 2011, PCCP, 13, 9616

Spiering, F. R., & van der Zande, W. J. 2012, PCCP, 14, 9923

Steinbacher, M., Fischer, A., Vollmer, M. K., et al. 2007, AtmEn, 41, 2111

Stocker, T. F., Qin, D., Plattner, G.-K., et al. 2013, IPCC, 2013: Climate Change 2013 – The Physical Science Basis (Cambridge: Cambridge Univ. Press),

STScI Development Team, 2013 pysynphot: Synthetic photometry software package, Astrophysics Source Code Library, ascl:1303.023

Tange, O. 2011, login: The USENIX Magazine, 36, 42, http://www.gnu.org/s/parallel

Thalman, R., & Volkamer, R. 2013, PCCP, 15, 15371

Thompson, M. A., Krissansen-Totton, J., Wogan, N., Telus, M., & Fortney, J. J. 2022, PNAS, 119, e2117933119

Tinetti, G., Meadows, V. S., Crisp, D., et al. 2005, AsBio, 5, 461

Trainer, M. G. 2013, Current Organic Chemistry, 17, 1710

Trainer, M. G., Pavlov, A. A., DeWitt, H. L., et al. 2006, PNAS, 103, 18035

Tran, H., Boulet, C., & Hartmann, J. M. 2006, JGRD, 111, D15210

Tremblay, L., Line, M. R., Stevenson, K., et al. 2020, AJ, 159, 117

Trenberth, K. E., & Caron, J. M. 2001, JCli, 14, 3433

Trenberth, K. E., Fasullo, J. T., & Kiehl, J. 2009, BAMS, 90, 311

Turbet, M., Bolmont, E., Bourrier, V., et al. 2020, SSRv, 216, 1

Turbet, M., Bolmont, E., Chaverot, G., et al. 2021, Natur, 598, 276

Ugelow, M. S., De Haan, D. O., Hörst, S. M., & Tolbert, M. A. 2018, ApJL, 859, L2

Virtual Planetary Laboratory, 2021 atmos: Coupled climate-photochemistry model, Astrophysics Source Code Library, ascl:2106.039

Wallace, J. M., & Hobbs, P. V. 2006, Atmospheric Science: An Introductory Survey, Vol. 92 (Amsterdam: Elsevier)

Warneck, P. 1999, Chemistry of the Natural Atmosphere (Amsterdam: Elsevier)

Weiss, M. C., Sousa, F. L., Mrnjavac, N., et al. 2016, Nature Microbiology, 1, 16116

Wofsy, S. C., McConnell, J. C., & McElroy, M. B. 1972, JGR, 77, 4477

Wolf, E. T. 2017, ApJ, 839, L1

Wolfe, J. M., & Fournier, G. P. 2018, Nature Ecology & Evolution, 2, 897

Wordsworth, R., Forget, F., Selsis, F., et al. 2010, A&A, 522, A22

Wunderlich, F., Godolt, M., Grenfell, J. L., et al. 2019, A&A, 624, A49

Wunderlich, F., Scheucher, M., Godolt, M., et al. 2020, ApJ, 901, 126

Wunsch, C. 2005, JCli, 18, 4374

Xiao, Y., Logan, J. A., Jacob, D. J., et al. 2008, JGRD, 113, D21306

Yokouchi, Y., Ikeda, M., Inuzuka, Y., & Yukawa, T. 2002, Natur, 416, 163

Zahnle, K., Claire, M., & Catling, D. 2006, Gbio, 4, 271

Zahnle, K. J. 2006, Elements, 2, 217

Zahnle, K. J., Gacesa, M., & Catling, D. C. 2019, GeCoA, 244, 56

Zerkle, A. L., Claire, M. W., Domagal-Goldman, S., Farquhar, J., & Poulton, S. W. 2012, NatGe, 5, 359

Zhan, Z., Huang, J., Seager, S., Petkowski, J. J., & Ranjan, S. 2022, ApJ, 930, 133